# EXPERIMENTS TO DEVELOP HIGH Q AND TUNABLE SUPERCONDUCTING COPLANAR RESONATORS APPLICABLE FOR QUANTUM BIT TECHNOLOGY

BY

JOANNE ELIZABETH HEALEY

A thesis submitted to
The University of Birmingham
For the degree of
DOCTOR OF PHILOSOPHY
School of Physics and Astronomy
Supervisors: Dr. M. S. Colclough and Dr. C. M. Muirhead

November 18, 2010

*To my Father Mark, Mother Roslyn, and Brothers Matthew and Daniel.*

I would first like to thank my supervisors Mark Colclough and Chris Muirhead for proposing a fascinating and intellectually stimulating PhD. Their humour, light heartedness and an extensive knowledge of physics has helped me to complete this PhD. I would like to thank Gary Walsh for his hard work, providing me with the tools to do my research, enthusiasm and most of all, his patience in creating such beautifully crafted cryostats and microwave boxes. I would also like to thank Michael Parks, for always supplying me with liquid Nitrogen and Helium on a "yesterday" timescale.

Throughout my PhD I have greatly benefitted from working within a collaboration with the National Physics Laboratory. My collaborators Alexander Tzalenchuk, Tobias Lindstrom and Carol Webster, have inspired, encouraged and supported me throughout.

I would also like to thank all of my friends and mentors who I have had the pleasure of working with throughout my PhD. Richard Lycett, Suzanne Gildert, Silvia Ramos, Charlotte Bowell, Elizabeth Blackburn, Ted Forgan, Colin Gough, Joe Vinen, Ed Tarte, Georgina Klemencic, Richard Heslop and Alex Holmes have always been there to support me and provide me with a coffee fix whenever I have needed it.

I owe a great deal of thanks to my boyfriend Shane O'Hehir. His attitude towards work and personal life is a breath of fresh air in this sometimes hectic world.

Lastly, I could not have completed my research or degree without the love and support of my family.

# ABSTRACT

Measurements are made on superconducting Niobium on Sapphire and oxidized Silicon microwave coplanar resonators for quantum bit experiments. Device geometry and materials are investigated and quality factors in excess of a million have been observed.

The resonant frequency as a function of temperature of a coplanar resonator is characterised in terms of the change in the number density of superconducting electrons. At lower temperatures, the resonant frequency no longer follows this function, and evidence is shown that this is associated with the resonant coupling of the resonant frequency with two level systems in the substrate.

At $T < 2.2$ K the resonant frequency scales logarithmically with the temperature, indicating that two level systems distributed in the volume of the Silicon Dioxide affect the electric permittivity. Applying higher input microwave power levels is shown to saturate these two level systems, essentially decoupling them from the CPR resonance. This is observed as an increase in resonant frequency and $Q$ factor.

The resonant frequency is also shown to have a high sensitivity to a magnetic field applied perpendicular to the plane of the coplanar resonator, with a quadratic dependence for the fundamental, second and third harmonics. Frequency shift of hundreds of linewidths are obtained. Coplanar resonator are fabricated and measured with current control lines built on chip, and these have shown to produce frequency shifts of tens of Kilohertz.

# CONTENTS

# LIST OF FIGURES

# LIST OF TABLES

# 1. INTRODUCTION

## *1.1 Overview.*

The purpose of the experimental work described in this thesis is to investigate changes in resonant frequency and quality factor of Superconducting Coplanar Resonators (CPRs) driven by a microwave source, with variations in device material and geometry. Both resonant frequency and quality factor are measured as a function of temperature.

Investigations are also made into novel methods of perturbing the CPR resonant frequency. This is achieved by an externally applied magnetic field, and an internally applied magnetic field through an inbuilt current control line on chip. These methods are shown to provide a large and reproducible change in the CPR resonant frequency.

The research undertaken here can be used to support research into cavity quantum electrodynamics (CQED) [1], quantum computing [2], kinetic inductance detectors [3], filters [4], and resonators [5].

## *1.2 CPR Basic Concepts.*

A coplanar resonator consists of a central conductor strip separated by a gap on either side from ground conductor planes. The conductor strip and planes are made from high electrical conductivity materials that support an electromagnetic field, and these reside on a high dielectric constant, low loss substrate. A picture of a CPR is given below.

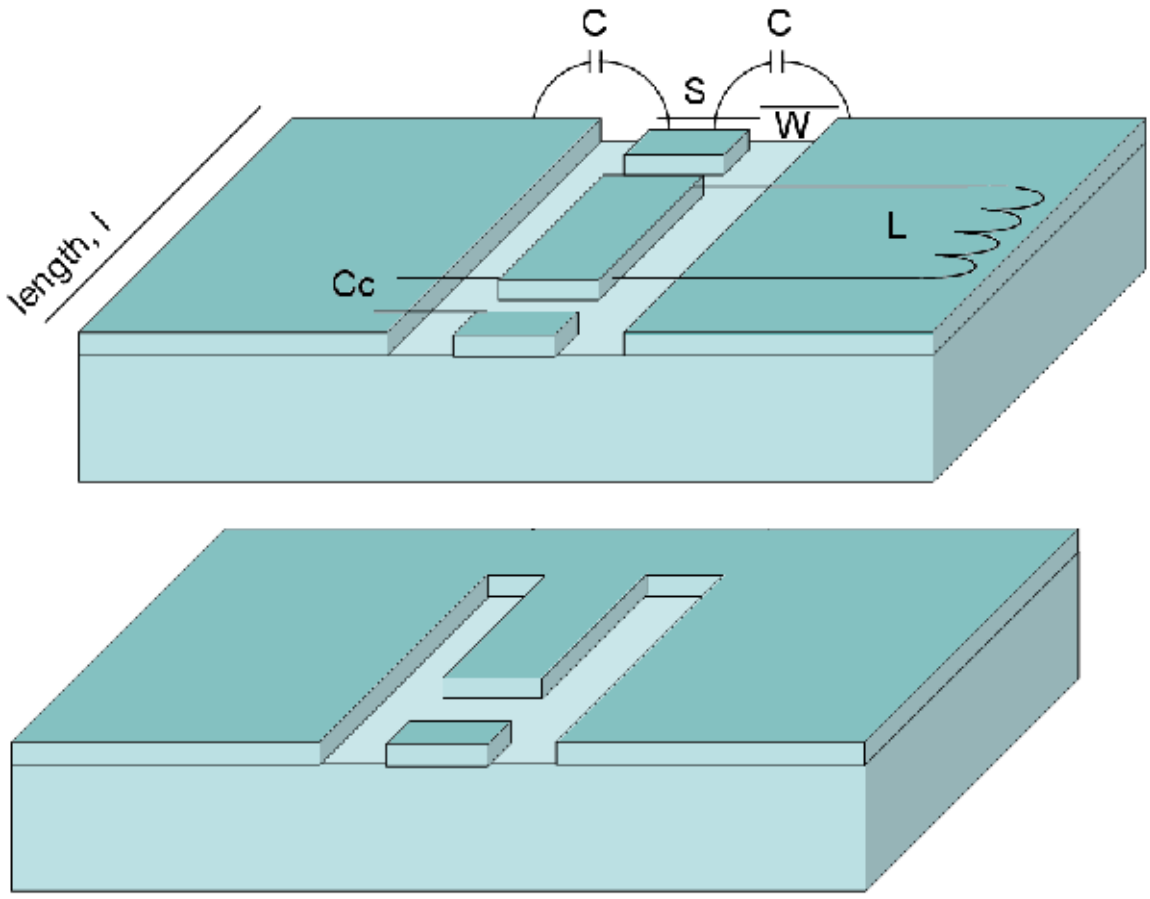


*Fig. 1.1:* **Top**, A diagram of a half wavelength CPR. The dimension of the conductor strip is given by $s$, and the separation between the inner and the outer conductor planes are given by $w$. $L$ and $C$ are the inductance and capacitance of the inner conducting strip. **Bottom**, A diagram of a quarter wavelength CPR.

The central conductor strip can resonate at a frequency that is determined by its inductance ($L$) and its capacitance ($C$). The inductance is dependent on the length ($l$) of the conducting strip and the ratio of its width to the total separation of the two ground planes $s/(s + 2w)$. The capacitance is due to the electric field between the conducting strip and the outer ground planes.

The modes of a CPR are equivalent to a resonant waveguide. A half wavelength resonant waveguide is constructed with its two ends open to air, and supports a half wavelength standing wave. For a half wavelength CPR this is achieved by the placement of coupling capacitors at each end of the conducting strip, see figure 1.1 [6, 7]. For a quarter

wavelength CPR one end of the conducting strip encompasses a coupling capacitor and the other end is shorted to the ground conductor plane [8, 9, 10, 11]. The transverse electromagnetic wave for the fundamental mode of a half wavelength CPR is given in figure 1.2.

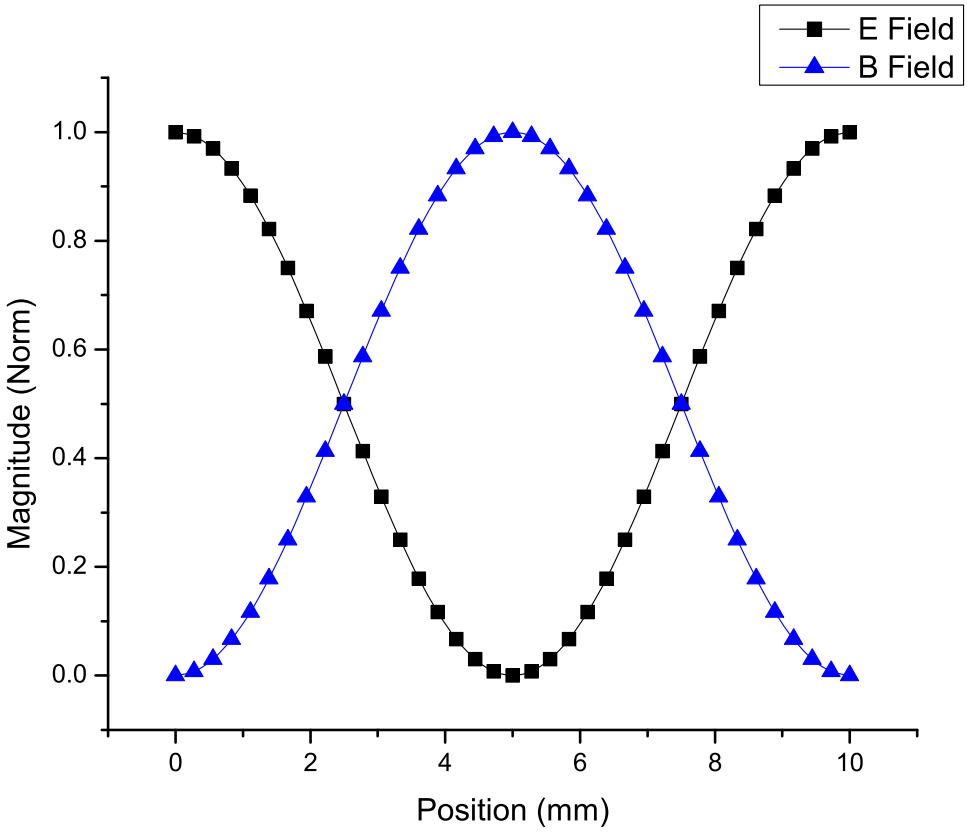


*Fig. 1.2:* Electromagnetic field pattern for a half wavelength resonance at fixed time $t = 0$ seconds, showing the variation in fields across the length of the CPR (Position 0 and 10 cm corresponds to the two ends of the CPR). The red curve represents the electric field E and the black curve represents the magnetic field B. The evolution of these waveforms follows a typical standing wave mode.

For a half wavelength resonator, all modal frequencies are given by $f_n = n/4\pi l\sqrt{LC} = nc/4\pi l\sqrt{1/2(\epsilon_r + 1)}$, where $n$ is the mode number, $L$ and $C$ are the inductance and capacitance, $c$ is the speed of light, $\epsilon_r$ is the dielectric constant of the substrate and $l$ is the length of the conducting strip.

CPRs of interest here are designed to resonate at microwave frequencies. When the

resonator is driven by an external microwave source through one end of the CPR (via the coupling capacitor) at a frequency above or below the resonant frequency, the signal transmitted through the device is small. When the microwave drive frequency is resonant with the CPR, then the amplitude of the transmitted signal is maximized. Below is a figure of the transmitted signal across a half wavelength CPR.

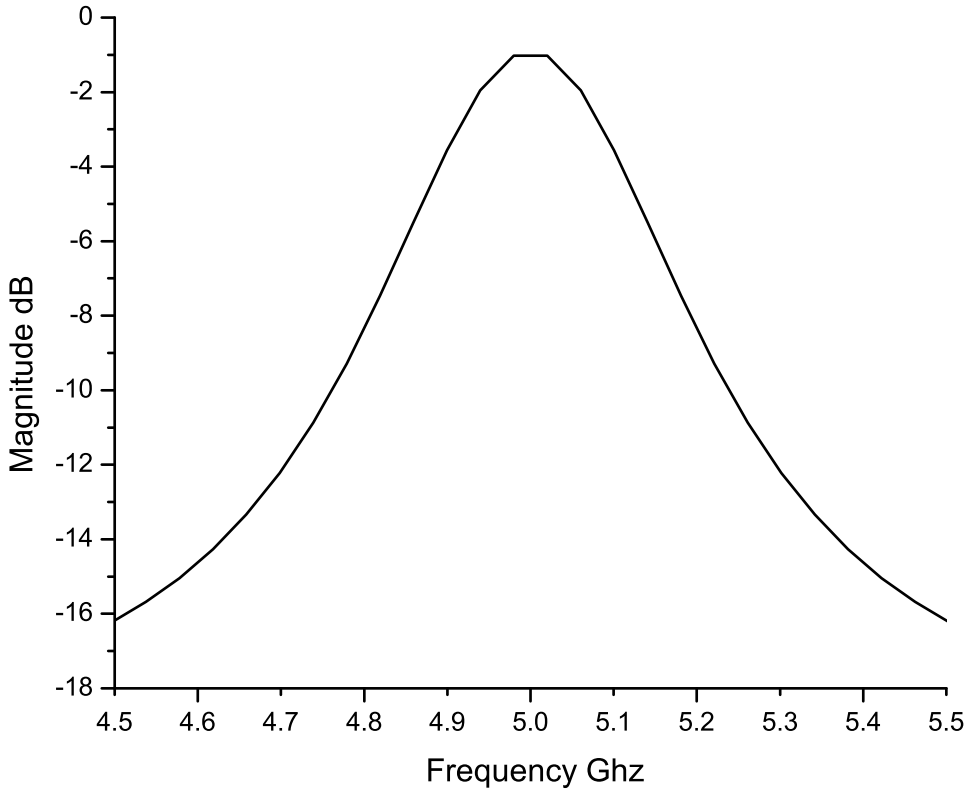


*Fig. 1.3:* Lorentizan shaped response of the transmission signal through a half wavelength CPR.

The parameters of interest in CPR operation are its resonant frequency and quality ($Q$) factor. The $Q$ factor is defined as the energy stored at resonance divided by the energy lost per cycle and is equivalent to the resonant frequency divided by its bandwidth (full width at half maximum). The inverse of $Q$ is a measure of energy loss and is dependent on the intrinsic, $Q_{int}$, and the extrinsic, $Q_{ext}$, quality factors.

The inverse of $Q_{int}$ describes the loss associated with the electrically conductive material and the dielectric substrate. The inverse of $Q_{ext}$ describes the loss associated with the coupling of the CPR to the external microwave source and radiation loss. The loaded $Q$ factor, $Q_L$ of the CPR is given by:

$$\left(\frac{1}{Q_L}\right) = \left(\frac{1}{Q_{int}}\right) + \left(\frac{1}{Q_{ext}}\right) \tag{1.1}$$

The losses defining the intrinsic and extrinsic $Q$ are described in more detail in the following chapters.

## 1.3 The History of Coplanar Waveguide Resonators.

CPRs have been the subject of intense interest to the scientific community since their invention by Cheng. P. Wen in 1969, over 4 decades ago [11]. The original terminology for these devices was the "planar strip line", until it was pointed out that by changing the name to "CoPlanar Waveguide" (CPW), it would resemble his initials in honour of his invention.

CPWs are a type of planar transmission line used in microwave integrated circuits. They have a planar geometry with the conductors on the same side of the substrate, with the advantage of fast and inexpensive manufacturing using current on-wafer technology. There are many applications of the coplanar waveguide, including delay lines, filters, oscillators and resonators. The focus of this thesis are coplanar resonators and therefore the notation of CPR is more appropriately applied to these devices.

CPRs are made from metal and superconducting materials. Metal CPRs are used within the telecommunications industry due to their low dispersion, offering the potential to construct wide band circuits and components, and they do not require cryogenic cooling. Superconducting CPRs are devices of interest in scientific research as outlined in the overview.

The superconducting materials that are most commonly used are Aluminium (Al), Niobium (Nb) and Yttrium Barium Copper Oxide (YBCO). The advantages of using superconductors over normal metals are that they exhibit extremely low transmission loss and can be made smaller in size. CPRs made from superconducting Niobium have a short penetration depth $\lambda_L$, and thus can be made with dimensions close to the theoretical limit with thickness $2\lambda_L$ (although not ideal as conductor losses increase, hence $Q$ is not

maintained high).

Superconducting CPRs were initially used (and still are) as a direct method for measuring the absolute penetration depth, from measurements of the surface impedance. This is favourable to a common indirect measurement technique involving the extrapolation of the penetration depth to a temperature of absolute zero from changes in the resonant frequency of a microwave cavity [12, 13].

Superconducting CPRs find use as tuned cavities for the interrogation and manipulation of the state of quantum bits (Qubits), for Quantum Electrodynamic (QED) experiments [1]. They have been used to communicate information between two phase qubits [2]. They also can be used as detectors of radiation, such devices are called Kinetic Inductance Detectors [3, 8, 9, 14]. There is a great deal of interest in the development of novel superconducting CPRs due to their wide application as sensitive measurement devices in other expanding fields of research.

## *1.4 Original Contribution.*

Much of the experimental work undertaken and discussed here, contributes to the study of CPRs as detectors of radiation and devices for cavity quantum electrodynamics (CQED). To do this, control over the behaviour of the resonant frequency and $Q$ factor of the CPR device under varying conditions is required. This has been achieved here by measuring the resonant frequency and $Q$ factor as a function of temperature, power, and magnetic field.

The response of the resonant frequency of a CPR to changes in temperature are characterised by changes in the number density of superconducting electrons [33]. At lower temperatures ($T < 2$ K) the resonant frequency drops, and this is attributed to the resonant frequency coupling to two level systems (TLS) within the substrate. Investigations made here confirm observation of these effects. Furthermore, measurements of the resonant frequency and $Q$ factor as a function of temperature, for varying power levels provide additional support for the evidence of TLS as a cause for the dip in the resonant frequency at low temperatures.

The method of applying a magnetic field perpendicular to the surface of the CPR, creates a tunable CPR suitable for use in the coupling process of a CPR with a QUBIT. These investigations show that the resonant frequency behaves quadratically to an increase in the magnetic field. This is attributed to the $H^2$ nature of the superconducting penetration depth. Applying a field of 0.2 mT perpendicular to the CPR geometry is focussed $\approx 400$ times in the gap between the inner and outer conductor, due to the high flux focussing factor of the device. The shift in resonant frequency for this applied field is $\approx 200$ linewidths, with a high and unperturbed $Q$ factor. This method is unique due to the fact that the $Q$ remains constant for magnetic fields applied below the critical magnetic field of the superconductor.

# 2. CPR AND QUBIT EXPERIMENTS: MOTIVATION FOR DESIGNING HIGH $Q$ CPRS

High $Q$ resonators form the basis of two types of technology that are described below. The first technology incorporates high $Q$ CPRs as high resolution detectors of radiation. The second technology couples high $Q$ CPRs with QUBITs to gain a greater understanding of the quantum mechanics that drive the most fundamental atomic processes.

CPRs can be used to detect radiation in the form of Kinetic Inductance Detector (KID) [3, 14] and/or Lumped Element KID (LEKID) [8, 9] devices. KIDs are based on quarter wavelength ($\lambda/4$) resonators, whereas LEKIDs are lumped inductors and capacitors. The operation of both devices differ, in that the KID is capacitively/electrically coupled to a feedline, whereas the LEKID is inductively/magnetically coupled. KID/LEKID circuit designs have a high transmission away from resonance and high absorption of the signal on resonance, as shown in figure 2.1a.

When electromagnetic radiation is incident upon a superconductor with energy greater than the bandgap energy $E = hf >> 2\Delta$ (cut-off frequency for Niobium at $T = 4$ K with $T_c = 9.2$ K is $f = 2\Delta/h \approx (7K_bT_c/h)\sqrt{1 - T/T_c} = 1$ THz, and for Aluminium at $T = 300$ mK with $T_c = 1.2$ K is $f = 150$ GHz), Cooper pairs can dissociate, becoming quasiparticles (for a description of superconducting particles see chapter 4). Changes in the number density of Cooper pairs can be measured with KID/LEKID devices by a change from resonance and phase of a transmitted microwave signal. Figure (2.1a) shows Cooper pairs at the Fermi level, and the density of states for quasiparticles $N_s(E)$ as a function of quasiparticle energy $E$. An increase in incident photon energy implies a reduction in the number density of Cooper pairs. Figure (2.1b) is the circuit diagram of a KID, with $hf$ representing the energy of the incident photon. The figure shows that the

increase in quasiparticle density changes the inductive surface impedance of the film.

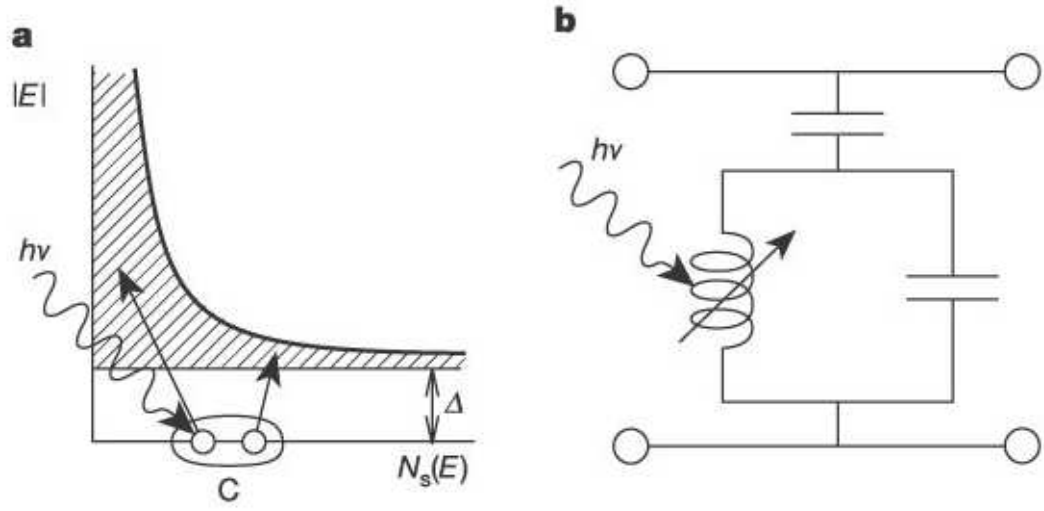


*Fig. 2.1:* **a** The superconducting band energy diagram versus the number density of superconducting Cooper pairs $N_s(E)$, the diagram also contains a schematic of a photon incident on a Cooper pair, generating two quasiparticle excitations. **b** The equivalent circuit diagram of the superconducting KID represented by a parallel LC circuit, capacitively coupled to a feedline. This figure is taken from reference [3].

When a photon interacts with a single KID/LEKID structure, the following results are obtained.

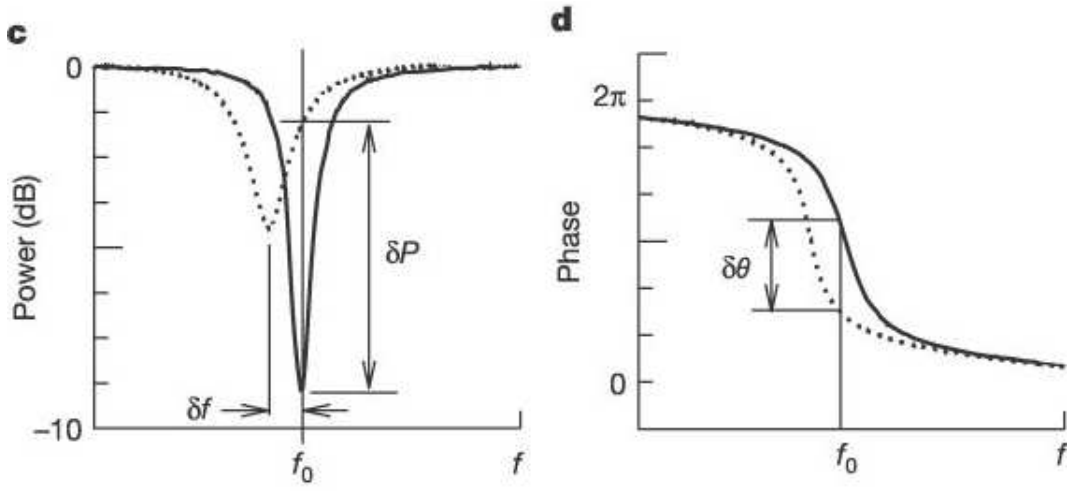


*Fig. 2.2:* **c** and **d** represents the response of a KID before (solid line) and after (dotted line) the absorption of a photon on the resonant frequency and the phase respectively. This figure is taken from reference [3]

The energy gap of superconductors is typically ∼meV (deduced from $2\Delta$ calculated above), which corresponds to photon detection in the region of radio to far infra-red photon energies. KID/LEKID devices are used within the space industry where the range of energies of particular interest are the mid infra-red to the far infra-red spectrum. Photons arriving with these energies are used to study early star formations, active galactic nuclei and galaxy evolution [15].

These KIDs/LEKIDs are typically multiplexed [10], with multiple resonators operating at slightly different frequencies coupled to the same feedline. This allows for individual addressing of each resonator by the feedline and increased cross-sectional area to increase the photon count rate.

When multiplexing these devices size is a crucial factor. It is more advantageous to use LEKIDs, as the cross-sectional surface area accessible for photon absorption is larger than that for KIDs. LEKIDs are typically 50 $\mu m^2$ in area, and can absorb photons arriving anywhere on their surface due to an inherent uniform current distribution. KIDs are typically a few millimetres in length, and can only absorb photons at the uncoupled end of the device where the current is a maximum.

The detection of microwave signals with high resolution and the reduction of cross talk between multiple resonators is possible due to the high $Q$ factors exhibited by these devices. Therefore there is increased interest within the scientific community to develop and fully characterise the response of these KIDs/LEKIDs for detecting radiation.

Half wavelength CPRs can also be used in experiments investigating the strong coupling of a single photon to a superconducting QUBIT. Strong coupling occurs when the CPR resonant frequency and QUBIT frequency coincide (on resonance), and an electric dipole moment lifts this degeneracy, see figure 2.3b. The off resonance microwave response is a single frequency peak located at the CPR resonant frequency, see figure 2.3a.

When the CPR and QUBIT are on resonance, the electric dipole moment that lifts the degeneracy is observed as a shift in the microwave frequency response, producing two new frequency peaks. A minima between these two peaks is centered at the original CPR resonant frequency. The difference between these peak frequencies corresponds to the interaction rate ($2g$), which is also known as the vacuum Rabi frequency. On resonance, a continuous exchange of energy between the CPR and QUBIT occurs, provided that the interaction rate is greater than the loss rate of photons from the cavity ($\kappa$) and the dephasing rate of the QUBIT ($\gamma$). If the interaction rate is less than these loss rates, the coherence between the CPR and the QUBIT is lost, and the effects decribed above are not observed.

The dephasing rate of the QUBIT ($\gamma$) is designed to be long to ensure that when the CPR and QUBIT are on resonance, maximum coherence of the two energy levels is maintained. The loss rate of photons from the CPR is expressed by $\kappa/2\pi = f_0/Q$ and therefore to limit the number of photons lost, the $Q$ is maximized. A high $Q$ CPR also means that it is easier to resolve the splitting of these two states, when the CPR and QUBIT are on resonance.

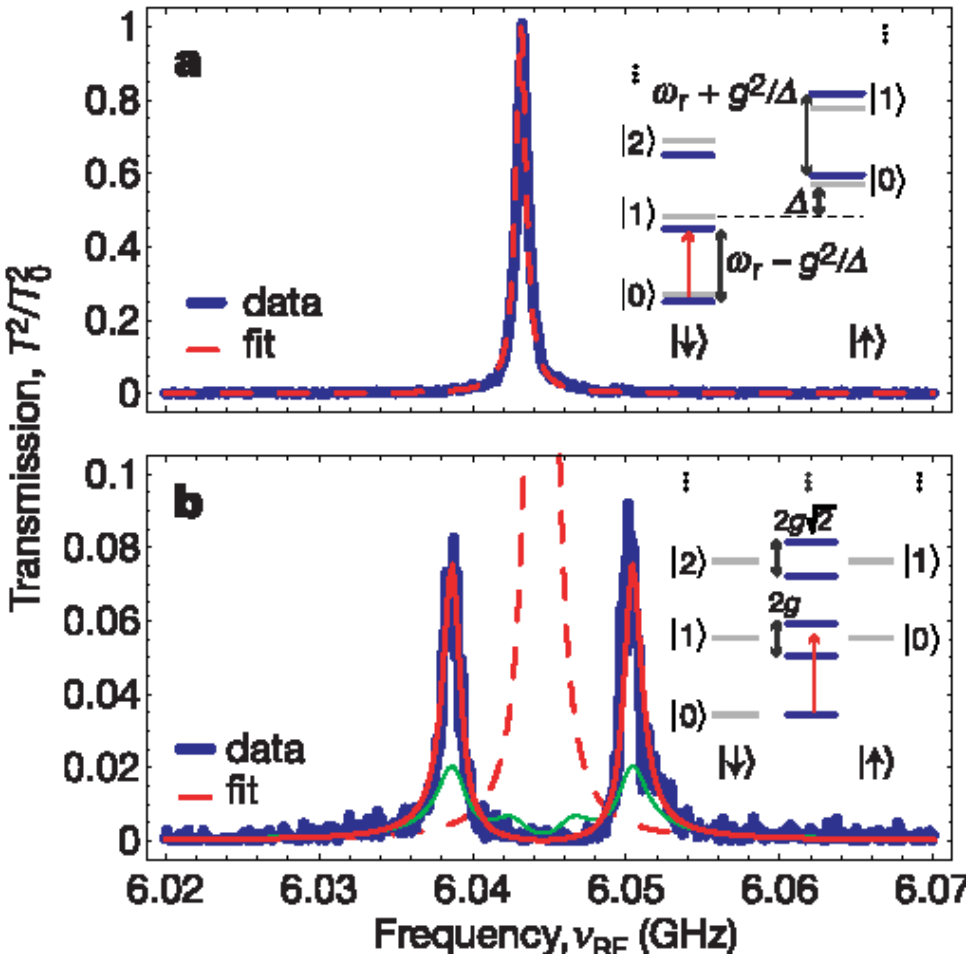


*Fig. 2.3:* **a** Measured CPR transmission as a function of microwave probe frequency for the CPR and QUBIT, off resonance (large $\Delta$). **b** Measured transmission as a function of microwave probe frequency for the CPR and QUBIT on resonance (zero $\Delta$). The inset diagrams represent the energy levels of the coupled systems for both large and zero $\Delta$. Taken from reference [1].

When the CPR and QUBIT are on resonance, two frequency peaks are observed in the spectrum, see figure 2.3b. Off resonance a single frequency peak is observed and located at the CPR resonant frequency, see figure 2.3a.

Wallraff *et al* [1] have measured the spectroscopic splitting due to the degeneracy between a CPR and a QUBIT, with a coupling strength of $g/2\pi = 11.6$ MHz, QUBIT decoherence $\gamma/2\pi = 0.7$ MHz, and photon loss rate of $\kappa/2\pi = 0.8$ MHz. Preliminary calculations based on the coupling between a flux QUBIT with dimensions given in reference

[6] and a CPR (with a Silicon Dioxide substrate) designed here, predicts the coupling rate to be $g/2\pi = 35$ MHz. Derived QUBIT decoherence rate based on present literature is $\gamma/2\pi = 1$ MHz, and an ideal photon loss rate based on $Q \approx 1,000,000$ is $\kappa/2\pi = 6$ KHz.

Considering the $Q$ of the CPR alone as the source of decoherence, then there will be $\approx 5500$ oscillations before the coherence between the coupled CPR and QUBIT state are destroyed, this is compared with $\approx 15$ oscillations currently observed and reported in reference [1]. Including decoherence of the QUBIT, the number of Rabi oscillations for both devices are similar, suggesting further investigation into reducing QUBIT decoherence should be undertaken.

Different QUBIT structures have also been investigated in concurrence with CPRs. They are the charge [1], flux [6], phase [16], quantronium [17] and transmon [18] QUBITs. These QUBITs and CPRs have all been shown to exhibit strong coupling interactions. There is an extensive current field of research investigating different strengths of coupling interactions [19] ranging from weak, dispersive weak, dispersive strong to quasi-dispersive strong [20]. Effects such as vacuum Rabi splitting and the Purcell effect [21] for example, are observed with CPRs and QUBITs, and are analogous to optical photon and atom coupling experiments [22].

# 3. TUNABLE QUBIT AND CPR EXPERIMENTS

## *3.1 QUBIT Tunability*

To perform Coplanar resonator/Quantum bit (CPR/QUBIT) experiments, either the CPR or the QUBIT has to be tunable. QUBIT tunability has been extensively studied by a number of groups [1, 16, 23]. One of the main leaders in this field of research is J. E. Mooij, who successfully demonstrated the ability to change the energy level spacing of a QUBIT under a flux bias with three Josephson Junctions (JJ) in a superconducting ring (the flux QUBIT) and a current control line, see figure 3.1.

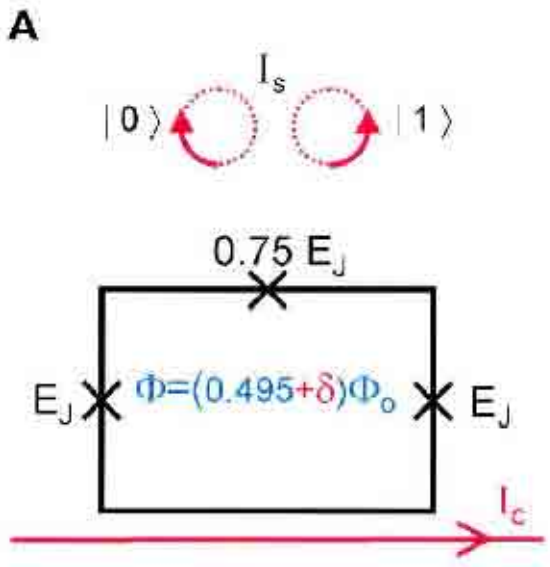


*Fig. 3.1:* Diagram of a 3 JJ QUBIT with directions of circulating current generated by the current control line ($I_c$). Taken from reference [23].

The simplest QUBIT is constructed from a single JJ in a superconducting loop. This device has a well known washboard energy-phase diagram, that can be tilted by an external magnetic field. This tilt of the washboard energy-phase diagram means that stable,

accessible energy states can be created, see figure 3.2. Experimentally, these energy states are generated by two directions of the circulating currents, as shown in figure 3.1.

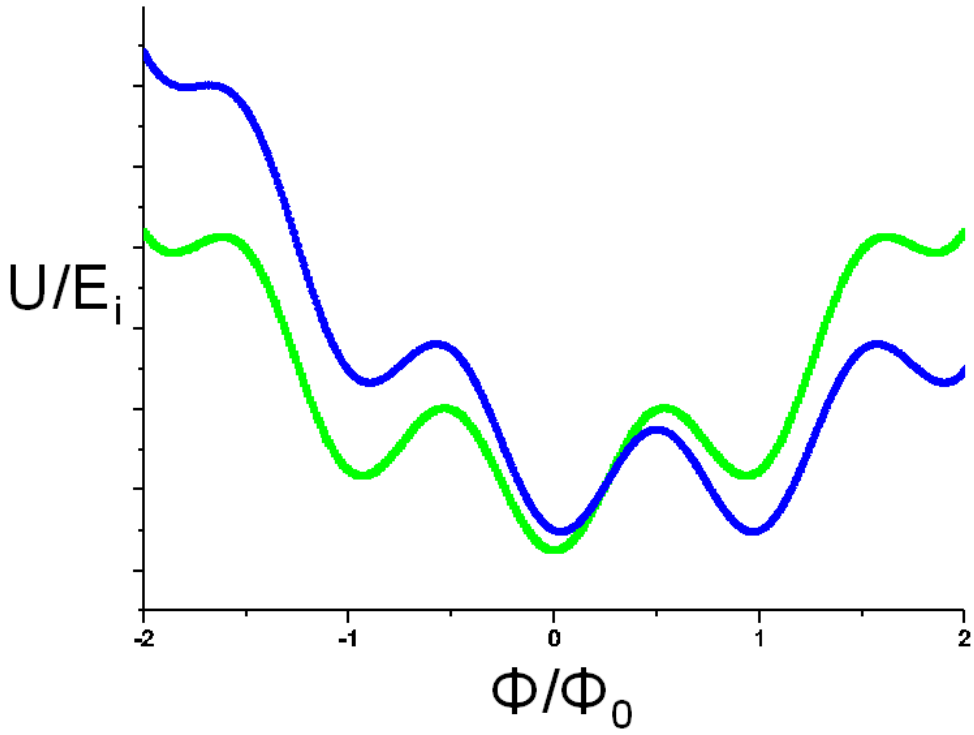


*Fig. 3.2:* Ratio of the energy applied ($U$) to the Josephson energy ($E_i$) of a QUBIT as a function of the ratio of the phase applied ($\Phi$) to the flux quantum $\Phi_0$, across a single JJ in a superconducting loop. The green washboard is representative of the QUBIT with no flux bias, whereas the blue washboard is representative of the QUBIT with 0.5 $\Phi_0$ bias.

When the field applied to the QUBIT by the current control line is 0.5 $\Phi_0$ (0.5 flux quantum), the two lowest energy states are symmetric and antisymmetric superpositions of the clockwise and anticlockwise circulating currents [24]. These two lowest energy states can be coupled resonantly to a CPR for CPR/QUBIT experiments. Strong coupling between the QUBIT and CPR can be achieved without a degradation of the $Q$ of the CPR, despite the small magnetic fields generated by the current control line perturbing the state of the QUBIT or the presence of the QUBIT itself.

The flux QUBIT is made scalable by introducing more JJ's into the superconducting loop, which is the size limiting factor for a QUBIT (as in figure 3.1). The extra JJ's add increased inductance in the loop, which allows a reduction in the size of the loop for no

overall change in QUBIT inductance. One advantage of this size reduction is that the QUBIT is less susceptible to flux noise. The extra JJ's also gives more flexibility over the tunability of QUBIT energy states, making it easier to resonantly couple the QUBIT with a CPR.

Figure 3.2 above, is based on the response from superconducting - insulating - superconducting (SIS) QUBIT, where low energy basis states are created by applying 0.5 $\Phi_0$. Research using superconducting-ferromagnet-superconducting (SFS) QUBITs with specific values of ferromagnet thickness have shown that low energy basis states can be created without applying an additional flux [25]. This may make the process of observing the strong coupling interaction between the CPR and QUBITs potentially easier, by excluding the need to manipulate the QUBIT with a current control line.

## *3.2 CPR Tunability*

Tunability of a CPR can be achieved by many techniques including changing the capacitance and inductance of the device, by changing the effective permittivity of a dielectric buffer layer, changing the permeability of a ferrimagnet ferrimagnet-CPR-dielectric sandwich and changing the non-linear Josephson inductance in a SQUID in the middle of the CPR conducting strip.

M. J. Lancaster *et al.* [26], have developed a technique for manipulating the dielectric constant of a buffer layer by a large electric field and as a result produce large tuning frequencies. The CPR sample is constructed from three layers; $Y_1Ba_2Cu_3O_x$/Buffer layer/$SrTiO_3$.

There are many different buffer layers such as (Ba,Sr)$TiO_3$, (Pb,Sr)$TiO_3$, (Pb,Ca)$TiO_3$, Ba(Ti,Sn)$O_3$, Ba(Ti,Zr)$O_3$ and $KTaO_3$, that are added to pure Strontium Titanate ($SrTiO_3$) substrate that are particularly sensitive to changes in the dielectric constant by large electric fields. The investigators report that adding 3% barium doping to Strontium Barium Titanate (SBT) buffer layer, and applying an electric field of 200 V, produces a 2.5 % shift from the resonant frequency and a change in $Q$ from $Q(0\text{ V}) = 450$ to $Q(200\text{ V}) = 250$. See figure 3.3 below:

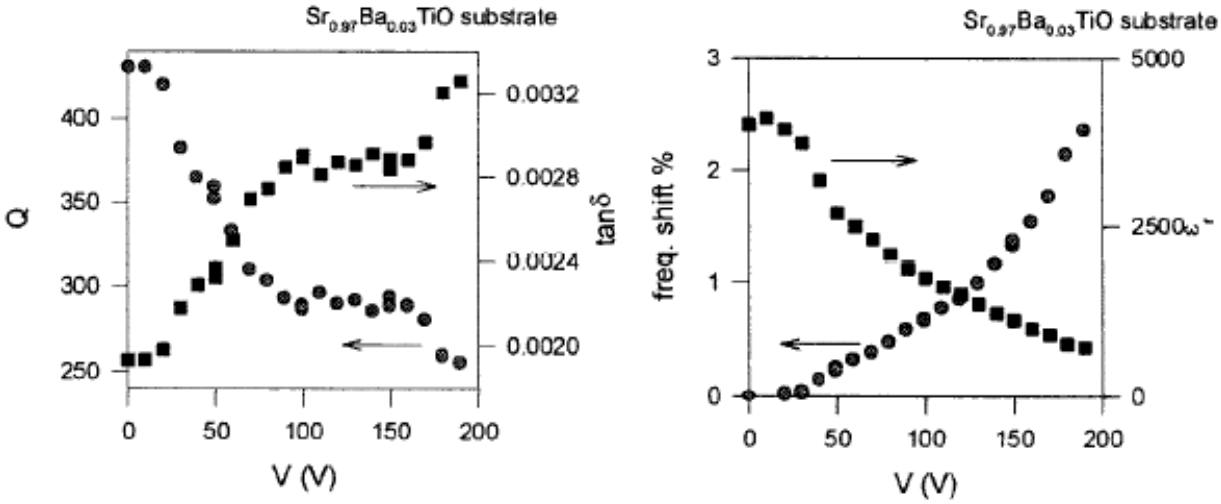


*Fig. 3.3:* $Q$, tan$\delta$, percentage frequency shift and dielectric constant ($\xi_r$) response for a 3% Barium doped SBT buffer layer. Taken from reference [26]

The relatively low $Q$ in this case renders this method insufficient for observing the strong coupling between a CPR and a QUBIT. This is because the coupling rate of the CPR/QUBIT system is less than the decay rate of the CPR, due to its low $Q$. However, this does make a suitable broadband filter, for which they are primarily designed.

The next two examples discussed rely upon changing or adding to the inductance of the resonator. D. Seron *et al* [27] add a ferrite layer to the top of the CPR to alter the magnetic permeability of the CPR, and hence change the resonant frequency. A. Palacios-Laloy [28] inserts a series of DC SQUIDs (superconducting quantum interference devices) into the central conducting strip of the resonator line to add an extra superconducting non-linear inductance. The SQUID is addressed by a small localized flux to perturb its state, change its inductance, and hence the total inductance of the conducting strip.

Seron *et al*, designed a multilayered sample based on the materials; $LaAlO_3$ substrate, $Y_1Ba_2Cu_3O_x$ superconducting CPR, followed by a ferrimagnetic layer consisting of Yttrium Iron Garnet (YIG) or Calcium Vanadium Garnet (CVG). In the absence of the ferrimagnetic layer, and passing a DC field in the $(a, b)$ plane of the YBCO, the following results are generated:

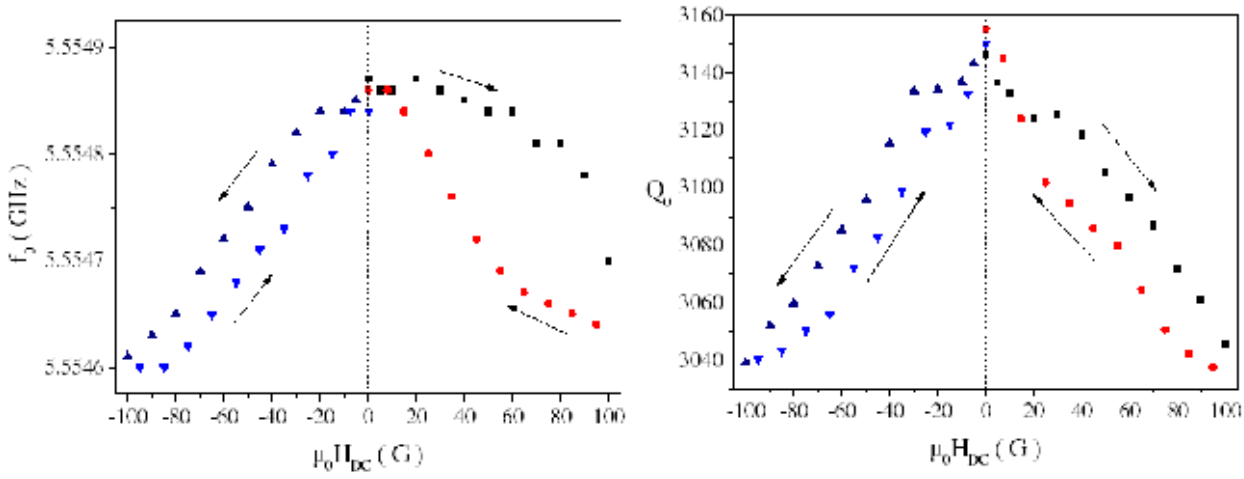


*Fig. 3.4:* Resonant frequency and $Q$ as a function of the DC magnetic field applied to the $(a, b)$ plane of YBCO. Taken from reference [27]

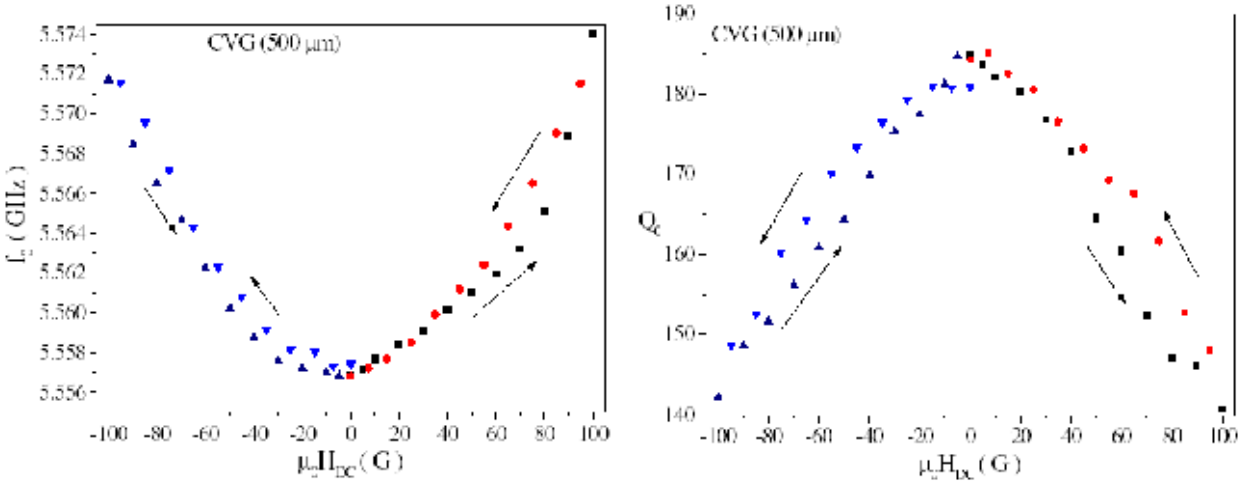


*Fig. 3.5:* Resonant frequency and $Q$ as a function of the DC magnetic field applied to the $(a, b)$ plane of YBCO in the presence of the CVG layer. Taken from reference [27]

The decrease in resonant frequency with an applied magnetic field parallel to the YBCO CPR is associated with an increase in the penetration depth of the superconductor. With the added ferrimagnetic layer they find a lower zero field resonant frequency and $Q$, and an increase in resonant frequency for an increase in the applied magnetic field. The resonant frequency in this case, is proportional to the magnetisation of the ferrimagnetic layer that is proportional to the applied magnetic field. The dependence of

the magnetisation on the resonant frequency outweighs the decrease associated with the change in the penetration depth.

Firstly, the difference in the zero field resonant frequency for figures 3.4 and 3.5 is solely associated with the change in the magnetic permeability associated with the presence of the ferrimagnetic layer. The zero field $Q$ is seriously degraded by the presence of the ferrimagnet. They attribute this to a ferrimagnetic resonance of the ferrite at the temperature of operation that is close to the resonance of the device, and leads to strong absorption of the microwave field.

The difference in the change in resonant frequency from the CPR with, and without the ferrimagnetic layer is about 50 times. The change in frequency for the ferrimagnetic layer is 0.29 % from the zero field frequency and this is attributed to an enhanced change in the permeability due to the high magnetic susceptibility of the ferrimagnetic layer.

This percentage change is not as large as the results demonstrated by Lancaster *et al*, and the $Q$ is not as high. Another method for perturbing the resonant frequency is given below.

A. Palacios-Laloy *et al*, place a seven Aluminium SQUID array into the central conducting strip of the CPR, below is the figure of the SQUID array (figure 3.6).

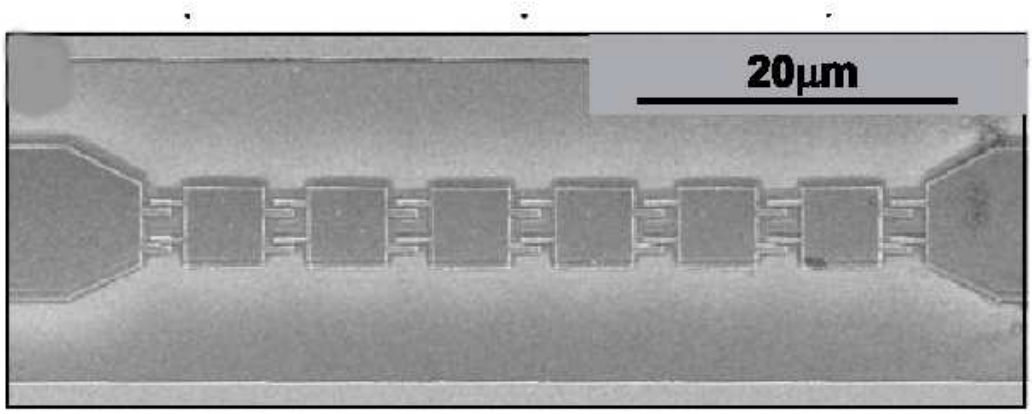


*Fig. 3.6:* A seven Aluminium SQUID array image taken by electron micrograph and fabricated using electron-beam lithography and double angle evaporation. Taken from reference [28]

A single SQUID contributes a non-linear inductance component to the total inductance of the line. This non-linear inductance varies with the magnetic flux that threads the SQUID loop. As the magnetic flux in the superconducting loop varies between 0 and $\Phi_0/2$ (where $\Phi_0$ is the flux quantization as discussed in the previous chapter), the non-linear inductance ($L_{J0}$) changes from $L_{J0} = \Phi_0/2\pi I_c$ to $L_{J0} \to \infty$, where $I_c$ is the critical current of the SQUID. Therefore the resonant frequency of the CPR when the magnetic flux is $\Phi_0/2$, is zero.

In fact, they report a 30 % tunability from the zero field frequency, and a change in $Q$ from $Q(\Phi_0/\Phi = 0) = 3.4 \times 10^3$ to $Q(\Phi_0/\Phi = 0.5) = 0$. See figure 3.7.

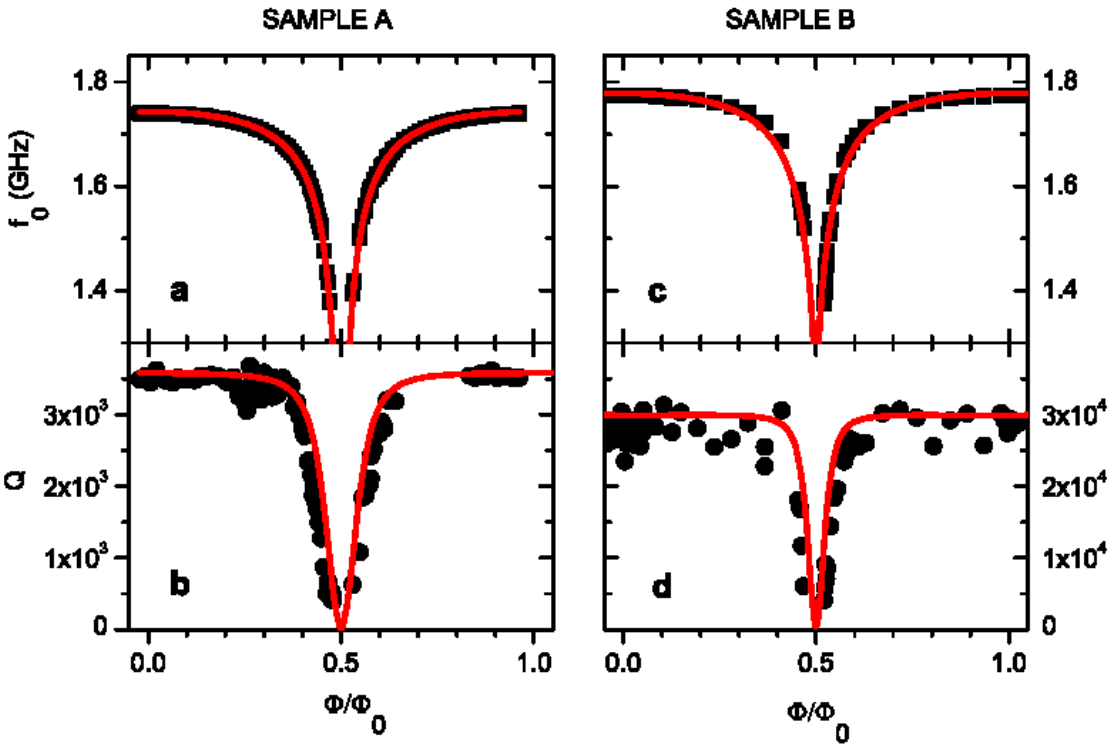


*Fig. 3.7:* The frequency and $Q$ of sample A with parameters: Coupling capacitance 27 fF, self inductance of one SQUID 40 pH and $I_{c0} = 330\ nA$, compared with sample B with parameters; coupling capacitance 2 fF, self inductance of one SQUID 20 pH and $I_{c0} = 2.2\ \mu A$ as a function of $\Phi/\Phi_0$. The red curve is a fit to the data at $T = 60$ mK. Taken from reference [28]

The result demonstrates a large change in the resonant frequency and $Q$ for a small change in the applied magnetic field. The $Q$ plateau for $\Phi/\Phi_0 < 0.5$ and $\Phi/\Phi_0 > 0.5$ is not

well understood, but is believed to be associated with the presence of low frequency noise in the sample (specifically critical current noise), or a dissipation source associated with the SQUID (and arising from dielectric losses in the tunnel barrier). They attribute the dip in $Q$ at $\Phi/\Phi_0 = 0.5$ to thermal noise. They recall that the resonant frequency depends on the energy stored in the resonator. At thermal equilibrium, thermal fluctuations in the photon number translate into fluctuations of the resonant frequency that causes this inhomogeneous broadening of the bandwidth, and reduction in the $Q$.

There have been many attempts to place SQUIDs in the gap between the central conducting strip, and ground conductor planes of CPRs [29, 30]. Essentially all of these experiments depict the same characteristic resonant frequency and $Q$ dip with applied field. If the CPR/SQUID system are used as tuning elements to couple to QUBITs, then the SQUIDs are not operated near the $\Phi/\Phi_0 = 0.5$ limit, therefore the change in the resonant frequency is not as high ($\sim$ Mhz). This is not ideal and essentially a loss-less tunable CPR is more desirable.

## 3.3 QUBIT and CPR Tunability

Both QUBIT and CPR tunability are employed in scientific research into cavity quantum electrodynamics. QUBIT tunability is achieved by changing the current in the current control line, that perturbs the energy states within the QUBIT. CPR tunability has been achieved by changing the capacitance and inductance of the CPR, by changing the effective permittivity of a dielectric buffer layer, changing the permeability of a ferrimagnet, ferrimagnet-CPR-dielectric trilayer and changing the non-linear Josephson inductance in a SQUID in the middle of the CPR conducting strip.

QUBIT tunability is difficult to realise experimentally owing to the difficulty in fabricating QUBITs. These QUBITs are micron sized and fabricated using electron-beam lithography. Choosing a suitable substrate that is compatible with this process determines the resolution of these QUBITs, this is discussed in more detail in chapter 11. Essentially it is difficult to reproducibly make these QUBITs. Secondly any impurities present in the fabrication process can cause pin holes in the Josephson Junctions causing an electrical

short, essentially eliminated any quantum effects. These impurities may also contribute to the decoherence of the QUBIT. Both effects cause loss meaning that the strong coupling between the CPR and QUBIT is difficult to achieve. It should be noted that when the QUBIT is coupled with the CPR, the $Q$ of the CPR does not degrade.

The tunability of the resonant frequency of a CPR has been shown to be in excess of 30 %, by exploiting the non-linear Josephson inductance of a SQUID in the middle of the CPR conducting strip [28]. The other methods show equally large tuning frequencies. All methods demonstrate a degradation of the $Q$ of the CPR. Ideally large tuning frequencies and unperturbed $Q$ of the CPR are required to make good measurements of the coupling between the CPR and the QUBIT.

## 3.4 Summary of Results

| Author | $\delta f/f_0(\%)$ | $Q_0$ | Reference |
|---|---|---|---|
| M. J. Lancaster | 2.5 | 450 | [26] |
| D. Seron | 0.29 | 185 | [27] |
| A. Palacios-Laloy | 30 | $3.4 \times 10^3$ | [28] |

*Tab. 3.1:* Table contains the author, percentage change in frequency, $Q$ and reference paper for different methods of perturbing the resonant frequency.

# 4. BASIC SUPERCONDUCTIVITY THEORY

## *4.1 Properties of Superconductivity.*

There are two key properties that define superconductivity, they are zero electrical resistivity and perfect diamagnetism [31]. Zero resistivity is demonstrated in the figure below:

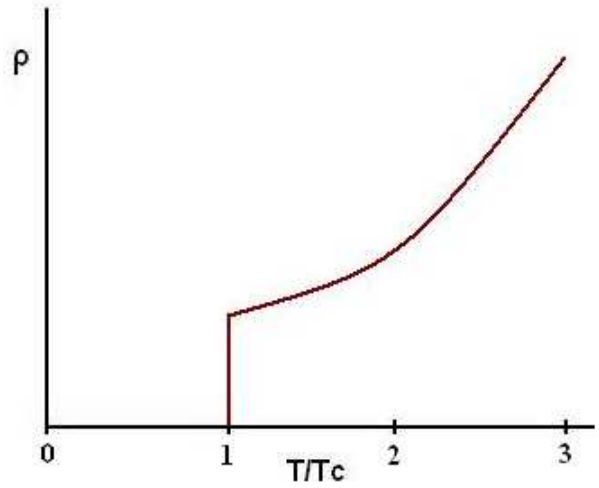


*Fig. 4.1:* Resistivity $\rho$ of a metal as a function of reduced temperature. At $T = Tc$, the metal undergoes a phase transition to a superconducting state characterised by zero electrical resistivity.

The electrical resistivity (which is inversely proportional to the electrical conductivity) of a type one superconductor such as Aluminium, changes from a finite value to zero when a material undergoes a first order phase transition from a normal conducting state to a superconducting state (type two superconductors such as YBCO undergo a second order phase transition). In this state, if a transient current is applied to the superconductor it will cause a current to flow that will not decay away with time.

A normal metal exhibiting perfect conductivity requires that the transient current does not decay away, meaning that scattering of electrons or other processes must be inhibited. However the superconducting state is different and exhibits perfect conductivity because of an ordered state of loosely associated pairs of electrons called Cooper Pairs [32].

Cooper pairs in BCS superconductors, are created by a weak attractive interaction between the electrons, generated by an electron-phonon interaction with the lattice. This causes an instability in the ordinary Fermi-sea ground state of the electron gas, and the result is the formation of bound pairs of electrons occupying a state with equal and opposite momentum and spin. These Cooper pairs have a spatial extension of order of the coherence length $\xi$, that is the length in which the number density of Cooper pairs cannot change dramatically in a spatially varying magnetic field. The energy required to break apart a Cooper pair and create two electron/hole-like particles called quasi-particles is $E_g = 2\Delta(T)$ (where $\Delta(T)$ corresponds to the order parameter of a superconductor). There is no mechanism for scattering processes to occur when an energy applied to the condensate is less than the energy gap $E_g$ of the system (neglecting Andreev Reflections), hence this process is loss-less. The energy required to break a Cooper pair can arise from increasing the temperature, magnetic field and/or applying a high powered microwave field [33].

The other property specific to superconductors is perfect diamagnetism. When a superconductor is placed in a weak magnetic field it will act as a perfect diamagnet, with zero magnetic induction in its interior. The superconductor expels the magnetic field applied and this is called the Meissner effect. The depth to which a magnetic field penetrates the superconducting surface is called the London penetration depth $\lambda_L$ [34].

## *4.2 B and J field Distributions in CPRs.*

In 1 dimension the magnetic field distribution and current density in a superconductor has the solution, $B = B_0 e^{-Z/\lambda_L}$ and $J_y = (B_0/\mu_0\lambda_L)e^{-Z/\lambda_L}$.

The current distribution for a long thin rod is shown below:-

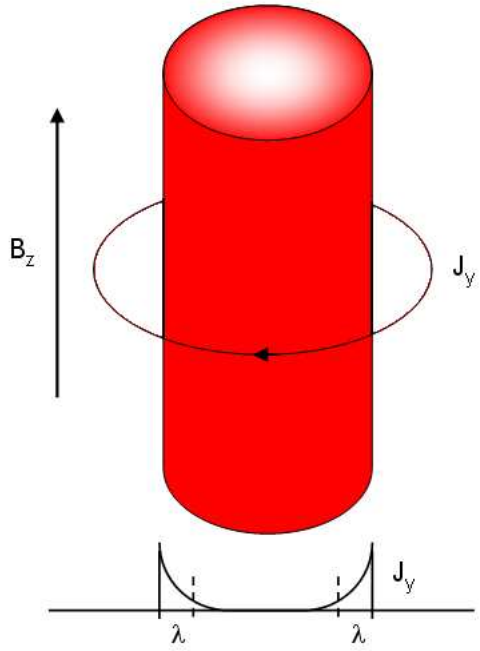


*Fig. 4.2:* A diagram of the induced current flow, $J_y$ in a superconducting long thin rod by an applied magnetic field, $B_z$.

The current distribution for a half wavelength CPR is shown below:

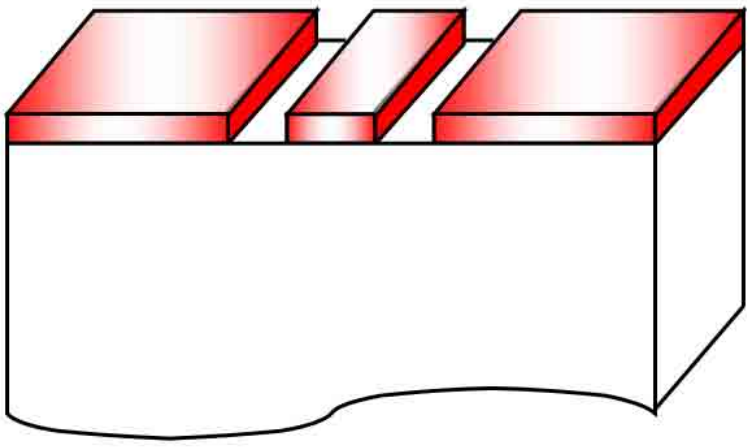

*Fig. 4.3:* Current density (red colour) for a CPR, ignoring resonant microwave effects.

In both cases the depth to which a magnetic field penetrates the superconductor is determined by the effective mass $\hat{m}$, the number density $\hat{n}_s$, and the effective charge $\hat{e}$ of

the Cooper pairs.

$$\lambda_L = \sqrt{\frac{\hat{m}}{\mu_0 \hat{n}_s \hat{e}^2}} \tag{4.1}$$

The current distribution is also shown to be related to the kinetic inductance as shown in the derivation below.

The kinetic energy ($K$) of the supercurrent ($I_s$) is given by $K = 1/2 \int \hat{m}\hat{v}_s^2 \hat{n}_s dV$, and the supercurrent density is $J_s = -\hat{n}_s \hat{e} \hat{v}_s$, where $\hat{v}_s$ is the supercurrent velocity and $\int dV$ is the integration over the volume. Substituting for $\hat{v}_s$ and introducing $\lambda_L$:

$$K = \frac{1}{2}\mu_0 \lambda_L^2 \int J_s^2 dV \tag{4.2}$$

The kinetic energy is also related to the kinetic inductance per unit length ($L_K$) by $K = 1/2 L_K I^2$:

$$\frac{1}{2} L_K I^2 = \frac{1}{2}\mu_0 \lambda_L^2 \int J_s^2 dS \tag{4.3}$$

where $I$ is the total current along the inductor. Re-arranging in terms of the $L_K$:

$$L_K = \mu_0 \lambda_L^2 \int \frac{J_s^2}{I^2} dS \tag{4.4}$$

The kinetic inductance can be made large by making $J_s$ as large as possible by non-uniform current distribution or by making the CPR thickness thin compared with $\lambda_L$.

## 4.3 The Temperature Dependent Penetration Depth.

The temperature dependence of the penetration depth is expressed as:

$$\lambda_L(T) = \frac{\lambda_L(T = 0K)}{\sqrt{1 - t^4}} \tag{4.5}$$

Where $\lambda(T = 0\ K)$ is the zero temperature penetration depth, $t$ is the reduced temperature factor and is equal to $T/T_c$. $T$ is the temperature and $T_c$ is the critical temperature at which a material changes state from a normal metal conductor to a superconductor. This equation arises from the temperature dependence of the number density of quasiparticles and Cooper pairs in the superconducting condensate.

The two fluid model describes the conductivity and the temperature dependent penetration depth that is associated with the temperature dependence of the quasiparticles

and Cooper pairs in the superconducting condensate, see Gorter and Casmier [35]. This model is based on a circuit containing two different conducting paths expressed by the impedence associated with the quasiparticles and Cooper pairs. The circuit diagram shown below includes resistors and an inductor. The resistance and the inductance of the embedded parallel circuit is associated with electron/hole-like particles (quasiparticles), with an impedance similar to normal metals. The inductance of the quasiparticles occurs because they cannot respond instantaneously to changes in the electromagnetic field. The inductor in the first parallel circuit is associated with the superconducting Cooper pairs.

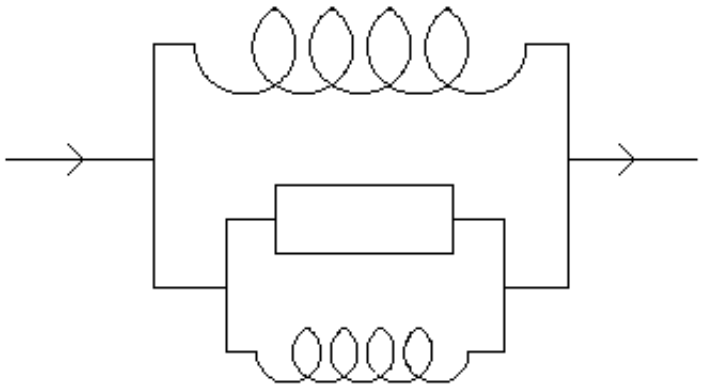

*Fig. 4.4:* Circuit diagram of a superconductor.

When the frequency applied to this circuit is zero (e.g. DC), the current flows solely through the inductor in the first parallel circuit (this has no resistence associated with it). At a finite frequency and in accordance with the first London equation [34], a time-varying supercurrent requires an electric ($E$) field to accelerate and decelerate the Cooper pairs, and this is loss-less. This electric field also acts on the electron/hole like quasi-particle excitations that scatter from impurities, and it is this mechanism that causes losses in superconducting resonators. This model is qualitative but extremely powerful as it demonstrates zero resistance when the applied frequency is zero and loss when the frequency is non-zero.

The total number density $n_T$ is given by the sum of the number density of quasiparticles

($n_n$) and number density of Cooper pairs ($n_s$), $n_T = n_s + n_n$. The temperature dependence of $n_s$ and $n_n$ is:

$$\frac{n_s}{n} = 1 - \left(\frac{T}{T_c}\right)^4 \tag{4.6}$$

$$n_n = n - n_s = n\left(\frac{T}{T_c}\right)^4 \tag{4.7}$$

Since the penetration depth is inversely proportional to the square root of the number density of superconducting Cooper pairs (as shown in section 4.2), then, $\lambda_L \propto 1/\sqrt{n_s} \propto 1/\sqrt{1-(T/Tc)^4}$.

## 4.4 The Demagnetisation Factor for Different Geometries.

The field to which a magnetic field penetrates a superconductor is determined by the London penetration depth, and the assumption has been that the magnetic field acts uniformly over the surface of the superconductor. This implies that the demagnetisation of the superconductor is zero. For geometries in which the demagnetisation factor of the sample is not zero, the magnetic field over part of the surface can exceed the applied field, see figure 4.5 below:

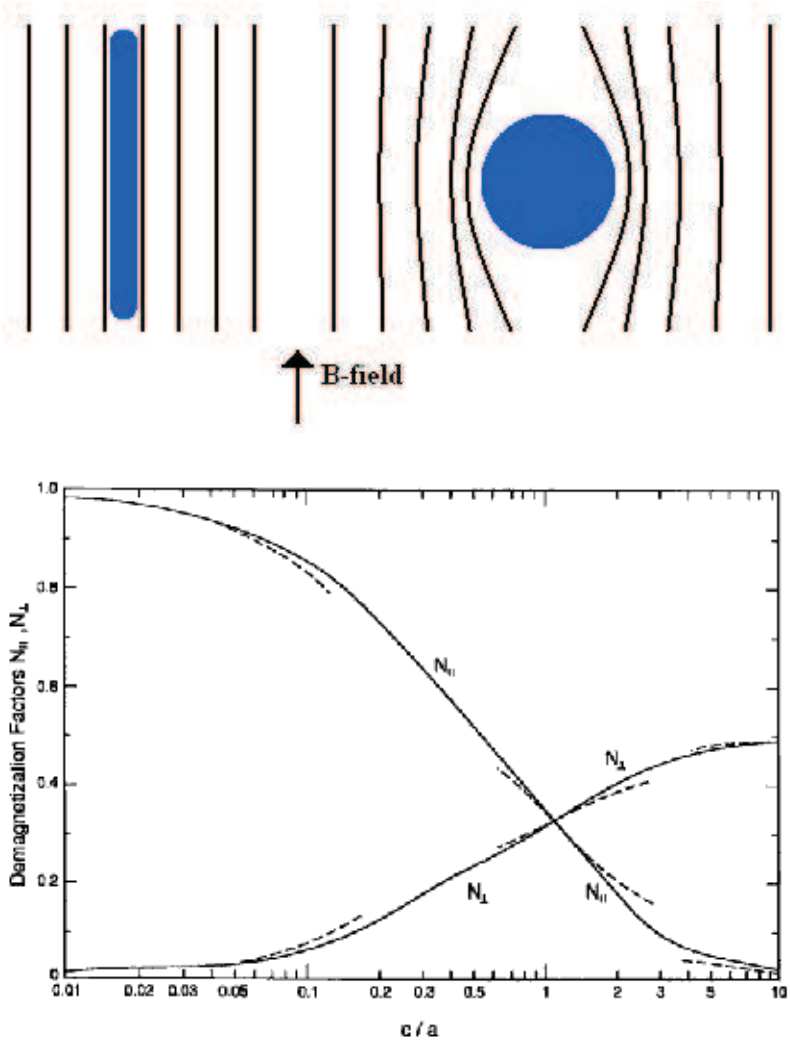


*Fig. 4.5:* **Top**, A superconducting long thin rod and sphere in an applied magnetic field. **Bottom**, The demagnetisation as a function of the aspect ratio, where $c/a$ corresponds to the length/diameter, $N_{\perp}$, perpendicular to the axis of an ellipsoid with semi-major axis $a = b \neq c$ and $N_{||}$ parallel the axis of an ellipsoid. Taken from reference [36].

For a long thin rod positioned parallel to the magnetic field the demagnetisation factor is zero, and for a sphere it is 1/3 [34]. The field inside ($H_{ins}$) a superconductor is expressed as:

$$H_{ins} = \frac{B}{\mu_0} - DM \tag{4.8}$$

Where $B$ is the magnetic field applied, $D$ is the demagnetisation factor and $M$ is the magnetization of the superconductor.

For a spherical ideal type 1 superconductor when the applied field reaches $2/3B_c$, the

field on the equator of the sphere reaches $B_c$. At this point normal regions invade the sphere, not as a thin equatorial belt of normal material, because if this were to happen, the whole sphere would turn normal. This is because the demagnetisation would disappear completely, leaving $B = B_{ins} \approx 2/3B_c$ and hence the internal field is less than the critical field allowing superconductivity to reappear. What does happen for a range of fields $2/3B_c < B < B_c$ is a coexistence of superconducting and normal regions which is known as the intermediate state. An intermediate state therefore exists for general ellipsoidal shapes in the field region:

$$1 - D < \frac{H}{H_c} < 1 \tag{4.9}$$

The demagnetisation factor generally only applies to spheres and ellipsoids, because the demagentisation factor is constant over the whole surface. The demagnetisation factor for a CPR is not constant over the whole surface, therefore it is more appropriate to apply the term flux focusing to the magnetic field perturbed by the superconductor.

To place the CPR in context with the example given in figure 4.5, the CPR ground plane is say equivalent to a long flat ellipsoid. For a long flat ellipsoid, $c/a \rightarrow 0$, and hence demagnetisation/flux focusing is maximised. The magnetic field applied perpendicular to the surface of the CPR is therefore highly focused in the gap between the conducting strip and outer ground conductor planes. This increased magnetic field affects the penetration depth, discussed in more detail below.

## *4.5 The Magnetic Field Dependence of the Penetration Depth.*

The Ginzburg-Landau theory is based on general observed features of superconductivity and not on any particular microscopic model, which is dealt with in BCS theory [37]. The particular importance of the Ginzburg-Landau theory is that it describes regions in which the state of the superconductor is non-uniform such as neighboring magnetic domain boundaries, quantized flux lines and more importantly with respect to microwave superconductivity is the surface superconductivity.

Ginzburg-Landau theory considers the free energy of any system to be an expansion

in powers of $n_p$, which is the effective Cooper pair density ($n_p = n_s/2$), so that:

$$F(n_p, T) = F_n(T) + \alpha(T)n_p + \frac{1}{2}\beta(T)n_p^2 + ... \tag{4.10}$$

This expansion of the free energy is only in terms of the temperature of the system. Since $\alpha$ and $\beta$ are dimensionless factors that are obtained from experimental observation, then they are easily modified to include the magnetic field dependence of the free energy on the system. This is shown in the first Ginzberg-Landau equation, see reference [38].

$$\Delta\epsilon = \Delta F/2\Delta F_0 = -\frac{1}{\kappa^2}\nabla^2 f + (|a|^2 + f^2 - 1)f = 0 \tag{4.11}$$

This is obtained using equation 4.10, $f$ is the order parameter equal to $\Psi/\Psi_0$, $\Psi_0 = \sqrt{\beta/|\alpha|}$ and $\Delta F_0 = \alpha^2/2\beta$. $\Delta\epsilon$ is the free energy density difference, $\kappa = \lambda_L(T)/\xi(T)$, and $a = A/\sqrt{2}B_c\lambda_L$ is the vector potential.

The equation shows that for high current densities, where $|a| \to 1$, $f$ will be depressed in the surface region. This increases $\lambda_L$ and the surface critical current density is correspondingly reduced.

Since the free energy difference is dependent on the square of the vector potential, then in the Meissner state the penetration depth in conventional superconductors exhibit a weak $H^2$ dependence near $T_c$ and at low temperatures [39, 40].

$$\frac{\lambda_L(T, H)}{\lambda_L(T, 0)} \propto \frac{H^2}{H_c^2} \tag{4.12}$$

where $\lambda_L(T, H)$ is the penetration depth at temperature $T$ and applied field $H$, $\lambda_L(T, 0)$ is equivalent to $\lambda_L$ described previously, and $H_c$ is the thermodynamic critical field.

When a magnetic field is applied to the surface of the CPR, the penetration depth, and the microwave currents that flow in the CPR are changed. This alters the kinetic inductance and the resonant frequency, and this is exploited when designing tunable resonators, as shown in the following chapters. It should also be noted that changing the kinetic inductance by either raising the temperature or changing the magnetic field, is achieved by changing the number density of Cooper pairs.

# 5. ELECTROMAGNETIC THEORY APPLICABLE TO SUPERCONDUCTORS

Coplanar resonators are made from both normal metals and superconducting materials. The $Q$ of normal metals and superconducting CPRs is inversely proportional to loss, and this loss can be related to the surface resistance ($Q_{int} = \omega L/R_s$, where $\omega$ is the frequency of the applied $EM$ field and $L$ is the inductance). The surface resistance is dependent on the depth to which a magnetic field penetrates the surface of the CPR. This distance is called the skin depth $\delta$ in normal metals and the penetration depth $\lambda$ in superconductors.

For a normal metal conductor the skin depth $\delta$, is equal to $\delta = \sqrt{(2/\mu_0\mu\sigma\omega)}$, where $\mu$ is the permeability of the material (=1 for non-magnetic material), $\mu_0$ is permeability of free space, and $\sigma$ is the electrical conductivity [41, 42].

The resistance of a metal is determined by $R = \rho l/A$, where $\rho$ is the electrical resistivity, $l$ is the length, $A$ is the cross-sectional area and $A = l \times \delta$. Therefore the surface resistance, $R_s$ of a normal metal is given by $R_s = \sqrt{\omega\mu\mu_0/2\sigma}$ and is a measure of the time-averaged power dissipated per unit surface area. Therefore the $Q$ of a normal metal is inversely proportional to square root of the frequency ($Q \propto \sqrt{\omega}$).

The depth to which the $EM$ field penetrates the superconductor is called the penetration depth of the material. This is different to the skin depth in normal metals because the penetration depth is not dependent on the frequency of the applied $EM$ field, as shown in section 4.2. The surface resistance of a superconductor is more complicated than the surface resistance of a normal metal, because of the two conducting channels represented by the quasiparticles and Cooper pairs.

The London theory considers the total surface current to be the sum of the normal component ($J_n$) and the supercurrent component ($J_s$), $J_T = J_n + J_s$. This is directly anal-

ogous to the number density of particles in the superconducting condensate as described by the two fluid model.

The complex conductivity of a superconductor is also expressed as the sum of two components; the normal component ($\sigma_{1s}$) and the superconducting component ($\sigma_{2s}$), where $\sigma_T = \sigma_{1s} - j\sigma_{2s}$. Provided that the superconductor is thick enough ($t >> \lambda_L$) to prevent transmission of the $EM$ field travelling through it, then the total surface impedance only depends on the frequency dependent complex conductivity. The complicated rectangular geometry (like a CPR) can therefore be reduced to a single boundary with a single boundary impedance value.

$$Z_s = R_s + jX_s = \sqrt{\frac{j\omega\mu_0}{\sigma_T}} = \sqrt{\frac{j\omega\mu_0}{\sigma_{1s} - j\sigma_{2s}}} \tag{5.1}$$

The total impedance of a superconductor, $Z_s$ is expressed by the sum of the surface resistance $R_s$ which is real, and the surface reactance $X_s$ which is imaginary.

The surface impedance for a plane wave incident on a superconductor such as Niobium, with $\sigma_{1s} << \sigma_{2s}$ is simplified to $Z_s = \sqrt{\omega\mu/\sigma_{2s}} \cdot (\sigma_{1s}/2\sigma_{2s} + j)$. Since the conductivity of the superconducting state is $\sigma_{2s} = 1/\omega\mu\lambda^2$, then the total impedance is given by:

$$Z_s = \frac{1}{2}\mu_0^2\omega^2\lambda^3\sigma_{1s} + j\mu_0\omega\lambda \tag{5.2}$$

The surface resistance extracted from the equation above is shown to be $R_s = 1/2\mu_0^2\omega^2\lambda_L^3\sigma_{1s}$. The surface reactance is given by $X_s = j\mu_0\omega\lambda$, and the surface inductance, $L_s$ is equal to $L_s = L_K + L_M$, where $L_K = \mu_0\lambda_L$ is the kinetic inductance and $L_M$ is the internal magnetic field. There is also a geometric inductance $L_G$, associated with a finite magnetic energy density ($\mu_0 H^2/2$) stored within the thin film. The total inductance $L_T$ is therefore determined by $L_T(T) = L_K(T) + L_G + L_M$.

It should be noted that the validity of this model is restricted to frequencies below the energy gap frequency ($\omega_g$) of the superconductor, since above that frequency additional loss mechanisms set in and the dissipation approaches that of the normal conductor state. It is assumed that $\omega << \omega_g$ when comparing the two materials.

As shown above, the $Q$ of normal metals is proportional to the square root of the frequency, and for superconductors the $Q$ is inversely proportional to the frequency. The

applied frequency therefore also determines the $Q$ of the material. From figure 5.1 below, it is shown that at lower frequencies the surface resistance is lower and therefore the $Q$ is higher for superconducting CPR.

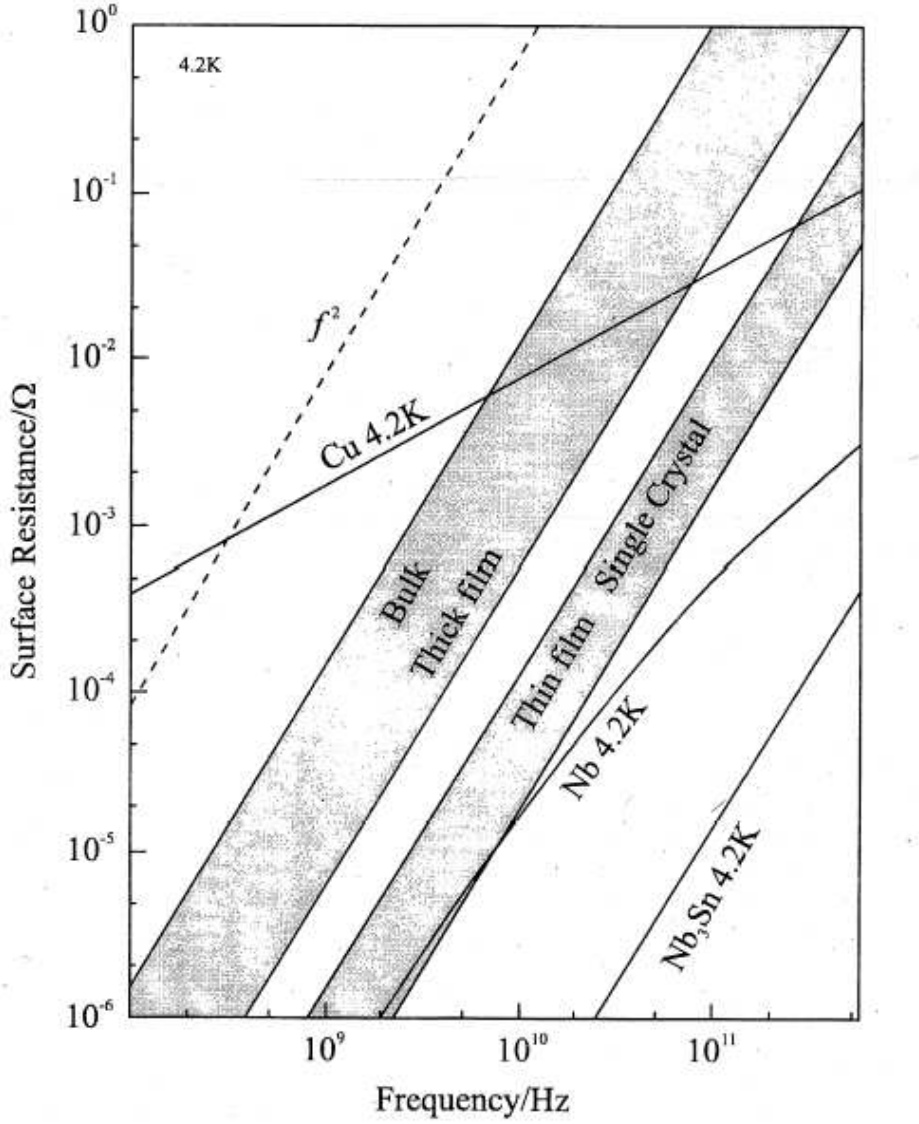


*Fig. 5.1:* The surface resistance of different materials as a function of frequency. The gray rectangle represents YBCO, where the width is associated with the varying transition temperatures of the material, dependent on the oxygen content. Taken from reference [43].

In fact it is reported [43] that the reduction in the surface resistance of superconducting Niobium below its critical temperature, at $T = 4.2$ K, and for a frequency of 10 Ghz, can

result in a $Q$ that is 500 times greater than Copper at the same temperature. Also the magnetic field and electric field intensities can be very high for superconducting resonant cavities making them suitable for CPR/QUBIT measurements due to their high coupling strengths.

# 6. TWO LEVEL SYSTEMS IN DIELECTRIC SUBSTRATES

Substrates form one of the most fundamental components of CPRs. They are necessary to support the patterened superconducting film, and have electrical properties such as high resistivity and low loss. Substrates such as Sapphire and Silicon naturally lend themselves for this purpose. A disadvantage common to all substrates is the presence of two level systems (TLS).

Two level systems (TLS) naturally occur in all man made and naturally occuring single crystals such as Sapphire and Silicon. TLS occur as paramagnetic impurities such as Chromium in Sapphire, and dangling bonds at the unpassivated interface in oxidized Silicon [44, 45, 46].

These TLS in the substrate of superconducting CPRs are becoming increasing problematic as our ability to sensitively measure the microwave response of these devices increases. In previous chapters, it has been shown that the resonant frequency increases monotonically while the conductor losses decrease, as described by the two fluid model. At temperatures $\sim T_c/10$, these mechanisms saturate and other effects become prominent, most notably a decrease in the resonant frequency as the temperature is reduced. This "back-bending" is now believed to be due to the presence of these TLS in the substrate.

At these low temperatures one would expect the properties of a dielectric to stay constant [47, 48]. However experimentally variation in both the effective dielectric constant and losses are observed. The TLS couple via an electric dipole moment to the CPR resonant frequency, much like the coupling occuring between a charge QUBIT and a CPR. This coupling results in a reduction in the resonant frequency and the $Q$ of the CPR.

The variation in the dielectric constant $(\epsilon(T) - \epsilon(T_0)/\epsilon(T))$ is expressed as, and taken

from reference [48]:

$$\frac{\epsilon(T) - \epsilon(T_0)}{\epsilon(T)} = -\frac{2nd^2}{3\epsilon}\left(ln\frac{T}{T_0} - [g(T,\omega) - g(T_0,\omega)]\right) \tag{6.1}$$

where $g(T,\omega) = Re\Psi(1/2 + \hbar\omega/2\pi i k_B T)$, $T_0$ is the reference temperature, $\Psi$ is the complex diagamma function significant only for $K_B T \leq \hbar\omega/2$, and $nd^2$ is the material dependent numerical factors.

Using cavity perturbation theory, the shift in resonant frequency is given by $\Delta f_0/f_0 = -(F/2)\Delta\epsilon/\epsilon$, where F is the filling factor which depends on the geometry and the electric field distribution. Therefore any change in the dielectric constant is proportional to the change in the resonant frequency.

The nature of the filling factor can also give some evidence of where the TLS exist. If TLS exist in the bulk of the superconductor then the filling factor is expressed as $F \approx \epsilon_r/(\epsilon_r + 1)$, and is independent of the CPR parameters, $w$ and $s$. If TLS exist on the surface layer, $F$ scales with the CPR geometry $w$ and $s$, and this is because the energy stored in the TLS load the total energy stored in the CPR resonance [49].

# 7. CPR DESIGN

The capacitance and inductance of a conventional CPR are associated with the geometry of the device and the superconducting material. To determine the capacitance of the CPR, the CPR is divided into regions and the electric field is assumed to exist only in that region. In this manner the capacitance of each region is determined separately. The total capacitance is therefore the sum of the capacitance of each region. This allows for a more accurate method of determining the resonant frequency [50].

The first derivation is based on a CPR residing on a infinitely thick dielectric substrate and measured in a vacuum. The later part of this chapter includes the solutions for a CPR on an infinite thick dielectric substrate, and measured in liquid Helium. The majority of equations given below are taken from reference [51].

## *7.1 Calculations of the Inductance and Capacitance of a Simple CPR on a Dielectric Substrate.*

A diagram of a CPR residing on a single Sapphire or Silicon substrate and measured in a vacuum is shown below.

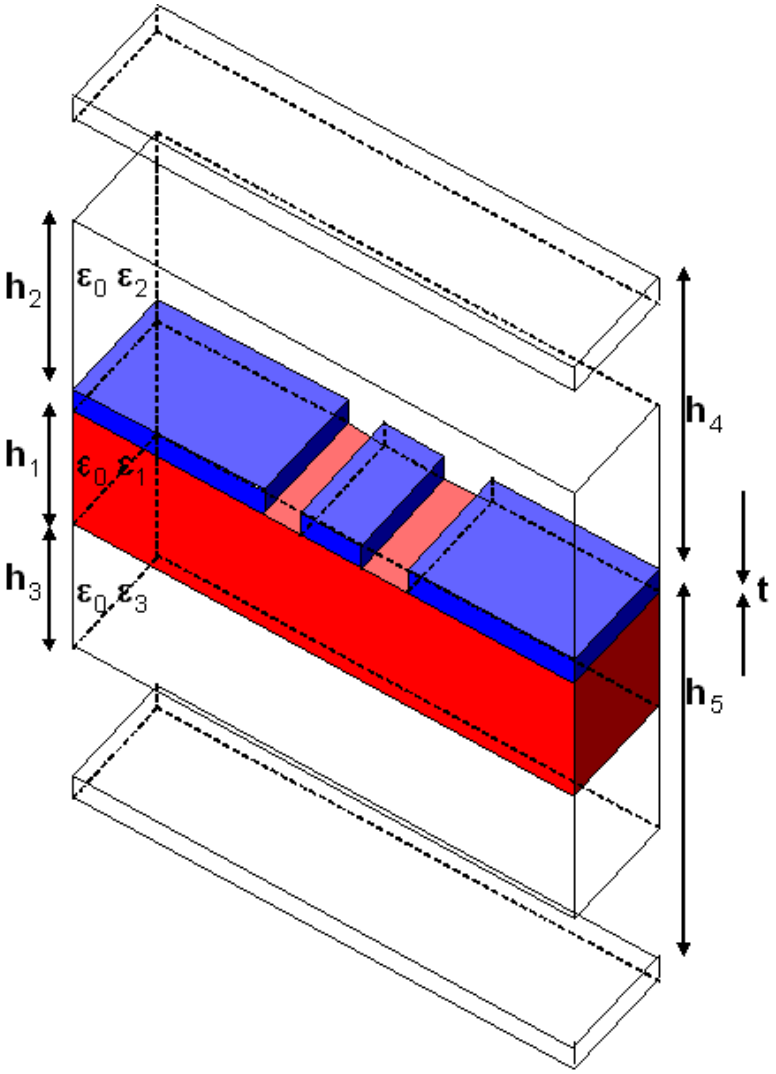


*Fig. 7.1:* Picture of a CPR (blue) residing on a dielectric substrate (red) and measured in a vacuum (clear).

The geometric capacitance of the CPR is determined by the sum of the capacitance of the lower dielectric material ($C_1$) that has a dielectric constant of $\epsilon_{r1}$ and a thickness of $h_1 = \infty$, and the capacitance of the air $C_{air}$ that has a dielectric constant of $\epsilon_{air} = 1$ and a thickness of $h_{air} = \infty$. The capacitance of the lower dielectric material is:

$$C_1 = 2\epsilon_0(\epsilon_{r1} - 1)\frac{K(k_1)}{K(k_1')} \tag{7.1}$$

$K(k_1)$ and $K(k_1')$ are the complete elliptical integrals and are given below. The complete elliptical integrals are used to describe the electric fields everywhere in the partial

regions and include fringing fields present near the corners of the CPR.

$$k_1 = \frac{\sinh(\pi s/4h_1)}{\sinh([\pi(s+2w)/4h_1])} \tag{7.2}$$

$$k_1^{'} = \sqrt{1-k_1^2} \tag{7.3}$$

where $w$ is the separation distance between the inner and outer conductor planes, $s$ is the width of the conductor strip, and $t$ is the thickness of the CPR. The electric field pattern for a CPR is shown below:

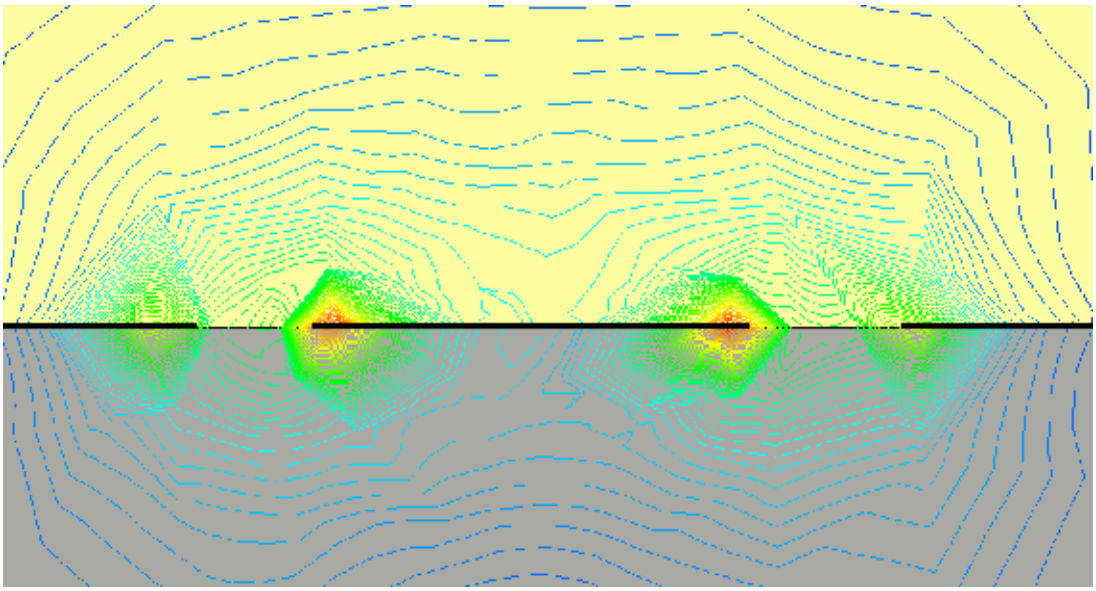

*Fig. 7.2:* A picture of the simulated electric field from one side of the CPR, looking end on. The grey colour represents the substrate and the yellow colour represents the air. The coloured lines that originate from the CPR represent the magnitude of the electric field. The strongest electric field is when the contour lines are closely packed and are represented by the colour red, the weakest electric field is represented by low density of contour lines and are represented by the colour blue. This is simulated in HFSS [52].

The capacitance of the air is:

$$C_{air} = 2\epsilon_0 \frac{K(k_3)}{K(k_3^{'})} + 2\epsilon_0 \frac{K(k_4)}{K(k_4^{'})} \tag{7.4}$$

where the complete elliptic integrals $K(k_3)$, $K(k_4)$, $K(k_3^{'})$ and $K(k_4^{'})$ are:

$$k_3 = \frac{\tanh(\pi s/4h_3)}{\tanh([\pi(s+2w)/4h_3])} \tag{7.5}$$

$$k_4 = \frac{\tanh(\pi s/4h_4)}{\tanh([\pi(s+2w)/4h_4])} \tag{7.6}$$

$$k_3^{'} = \sqrt{1-k_3^2} \tag{7.7}$$

$$k_4^{'} = \sqrt{1-k_4^2} \tag{7.8}$$

For this structure, $k_3 = k_4 = k_1 = k_0 = s/(s+2w)$ and $k_3{}' = k_4^{'} = k_1^{'} = k_0^{'}$, therefore:

$$C_{air} = 4\epsilon_0 \frac{K(k_0)}{K(k_0^{'})} \tag{7.9}$$

The total capacitance ($C_{CPR} = C_1 + C_{air}$) is:

$$C_{CPR} = 4\epsilon_0 \frac{K(k_0)}{K(k_0^{'})} + 2\epsilon_0(\epsilon_{r1}-1)\frac{K(k_0)}{K(k_0^{'})} = 2\epsilon_0(\epsilon_{r1}+1)\frac{K(k_0)}{K(k_0^{'})} \tag{7.10}$$

The effective permittivity is expressed as the ratio of $C_{CPR}$ to $C_{air}$, and is therefore:

$$\epsilon_{eff} = \frac{C_{CPR}}{C_{air}} = \frac{\epsilon_{r1}+1}{2} \tag{7.11}$$

Where $\epsilon_{eff}$ is the average dielectric constant of the structure.

The geometric inductance is expressed as:

$$L_g = \frac{\mu_0}{4}\frac{K(k_0^{'})}{K(k_0)} \tag{7.12}$$

The kinetic inductance as shown before is expressed as $L_K = \mu_0\lambda_L$, and by including geometric constraints the inductance is modified to [51];

$$L_k = \mu_0\lambda_L(T)\frac{C}{4ADK(k_0)}\left(\frac{1.7}{\sinh(t/2\lambda_L(T))} + \frac{0.4}{\sqrt{[(B/A)^2-1][1-(B/D)^2]}}\right) \tag{7.13}$$

It should be noted that these numerical factors (1.7 and 0.4) are derived for an YBCO CPR, and this solution may not be valid for Niobium CPRs. $A$, $B$, $C$, and $D$ are associated with the geometry of the structure and are determined by; $A = -t/\pi + 1/2\sqrt{(2t/\pi)^2+s^2}$, $B = s^2/4A$, $C = B - t/\pi + \sqrt{(t/\pi)^2+w^2}$ and $D = 2t/\pi + C$.

Substituting $C_g$, $L_g$, and $L_k$, then $f_0$ becomes:

$$f(T) = \frac{1}{\sqrt{C_g(T)(L_g+L_k(T))}} = \frac{1}{\sqrt{L_g C_{CPR}(T)}}\cdot\left(1-\frac{L_k(T)}{2L_g}\right) \tag{7.14}$$

$$f(T) = \frac{1}{2l\sqrt{\mu_0\epsilon_{eff}\epsilon_0}}\left(1-\frac{C\lambda_L(T)}{2ADK(k')}\left(\frac{1.7}{\sinh(t/2\lambda_L(T))} + \frac{0.4}{\sqrt{[(B/A)^2-1][1-(B/D)^2]}}\right)\right) \tag{7.15}$$

The temperature dependence of the penetration depth is given in section 4.3, and therefore the resonant frequency takes on the following form.

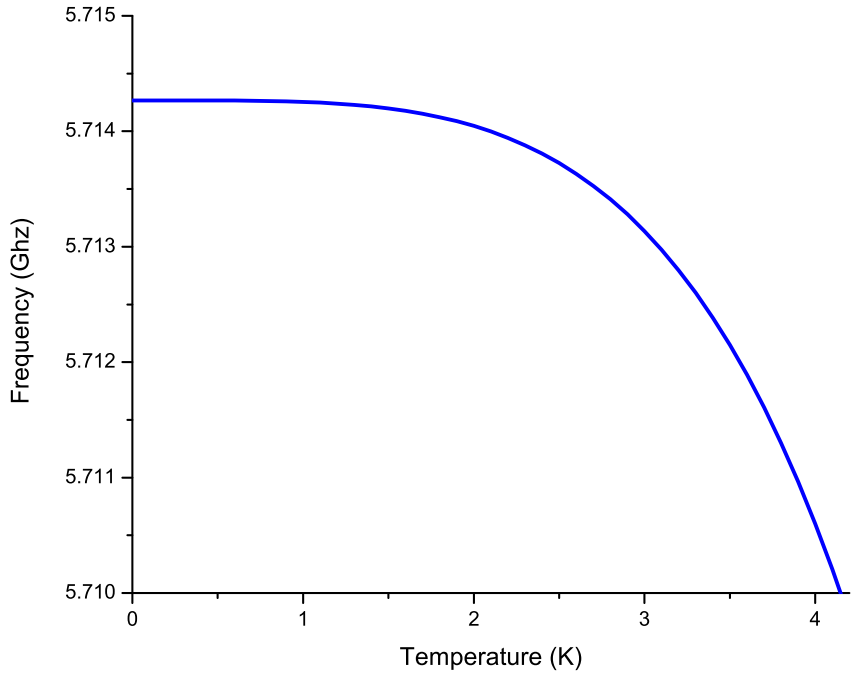


*Fig. 7.3:* A graph of the change in resonant frequency as a function of temperature for a Niobium ($T_c$ = 9.2 K) CPR residing on a sapphire dielectric substrate ($\epsilon_{r1}$ = 9.9 [53]) and assumed to be measured in a vacuum. The half wavelength CPR has a length of 11 mm, with geometry $w = 5\ \mu m$ and $s = 10\ \mu m$.

The resonant frequency sharply rises from zero to a finite value when the superconducting CPR undergoes the phase transition from a normal metal to a superconductor. This increase in the resonant frequency is due to the change in the penetration depth. The plateau occurs because the resonant frequency approaches the geometric resonant frequency of the CPR.

## *7.2 More Complex Structures.*

The calculation of the resonant frequency for more complex structures such as that shown in the figure below is appropriate for some of the structures that have been measured.

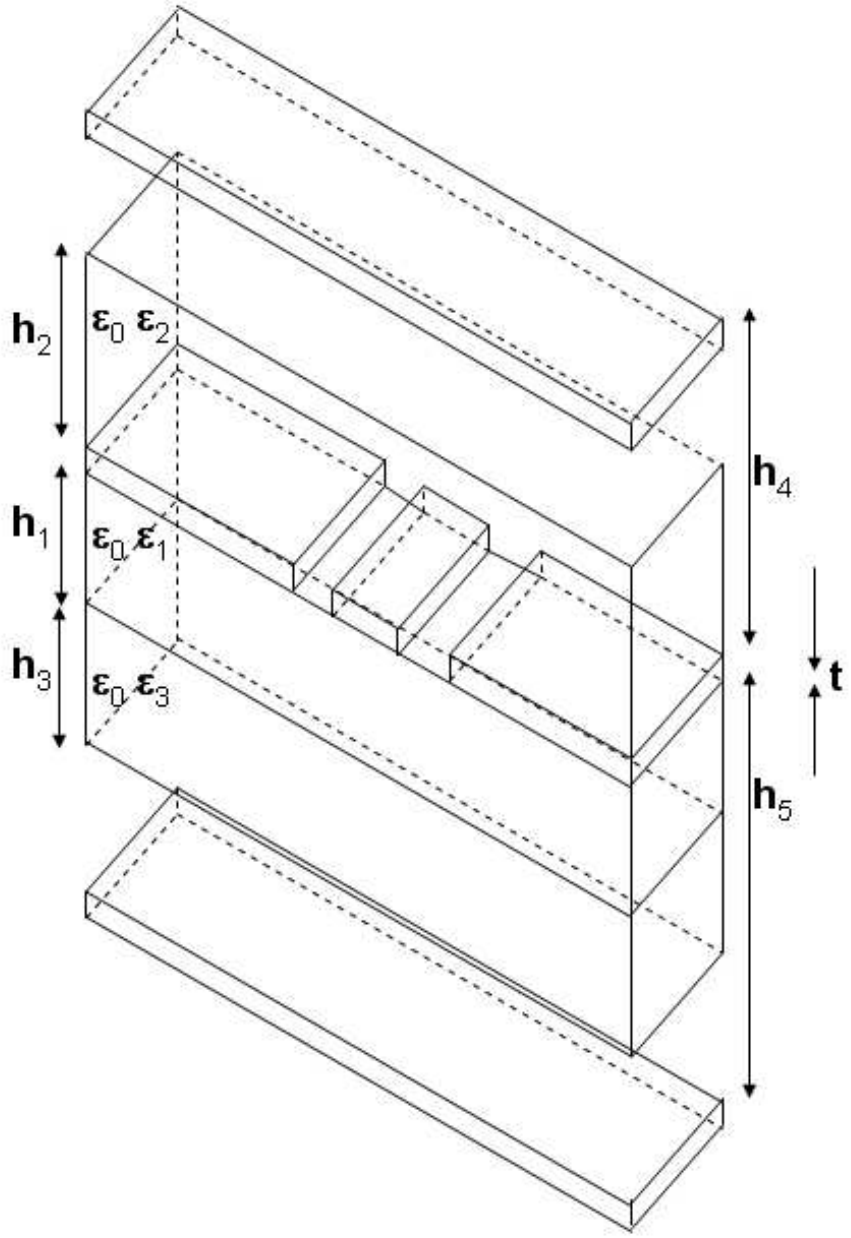


*Fig. 7.4:* Full structure of a CPR contains two lower dielectric substrates, a single upper dielectric substrate, and top and bottom air gaps with metal box covers.

The CPR structures measured here are based upon a CPR on an Sapphire substrate (previously discussed), CPR on an oxidized Silicon substrate and both measured at cryogenic temperatures either within a vacuum or liquid Helium environment. The measured resonant frequency varies quite drastically in all four situations.

### 7.2.1 Niobium CPR on a Sapphire Substrate and Measured in a Liquid Helium Environment.

The permittivity of the Sapphire substrate is $\epsilon_{Al_2O_3} \sim 9.9$ [53] and the capacitance $C_1$ is the same as in equation 7.1. The upper permittivity is nolonger zero, but is dependent on the permittivity of the liquid Helium that varies with temperature ($\epsilon_2(T)$). The air capacitance remains the same as before, $h_3 = h_4 = \infty$, $k_3 = k_4 = k_0 = s/(s+2w)$ and $K(k_1) \neq K(k_2)$ therefore the total capacitance, $C_{CPR}$ is:

$$C_{CPR} = C_{air} + C_1 + C_2 = 4\epsilon_0\left(1 + (\epsilon_{r1} - 1)\frac{1}{2}\frac{K(k_1)}{K(k_1')}\frac{K(k_0)}{K(k_0')} + (\epsilon_{r2}(T) - 1)\frac{1}{2}\frac{K(k_2)}{K(k_2')}\frac{K(k_0)}{K(k_0')}\right) \tag{7.16}$$

The resonant frequency is of the same form as in equation 7.15, however the effective permittivity is modified to, $\epsilon_{eff}(T) = 1 + q_1(\epsilon_{r1} - 1) + q_2(\epsilon_{r2}(T) - 1)$. Where $q_1 = \frac{1}{2}\frac{K(k_1)}{K(k_1')}\frac{K(k_0)}{K(k_0')}$ is associated with the Sapphire and $q_2 = \frac{1}{2}\frac{K(k_2)}{K(k_2')}\frac{K(k_0)}{K(k_0')}$ is associated with the liquid Helium.

### 7.2.2 Niobium CPR on a Silicon Dioxide on Top of a Silicon Substrate and Measured in a Vacuum Environment.

This structure has a double lower dielectric substrate, so therefore $k_1 \neq k_2 \neq k_3$, and $k_4 = k_5 = k_0 = s/(s+2w)$. The effective permittivity in this case is:

$$\epsilon_{eff} = 1 + q_3(\epsilon_{r3} - 1) + q_1(\epsilon_{r1} - \epsilon_{r3}) \tag{7.17}$$

where $q_1$, $\epsilon_{r1}$ is associated with the Silicon Dioxide and $q_3 = \frac{1}{2}\frac{K(k_3)}{K(k_3')}\frac{K(k_0)}{K(k_0')}$, $\epsilon_{r3}$ is associated with the Silicon.

### 7.2.3 Niobium CPR on a Silicon Dioxide on Top of a Silicon Substrate and Measured in a Liquid Helium Environment.

This structure has a double lower dielectric substrate, so therefore $k_1 \neq k_2 \neq k_3$ and $k_4 = k_5 = k_0 = s/(s+2w)$. The effective permittivity in this case is:

$$\epsilon_{eff} = 1 + q_2(\epsilon_{r2}(T) - 1) + q_3(\epsilon_{r3} - 1) + q_1(\epsilon_{r1} - \epsilon_{r3}) \tag{7.18}$$

where $q_1$, $\epsilon_{r1}$ is associated with the Silicon Dioxide, $q_2$, $\epsilon_{r2}(T)$ is associated with the Liquid Helium and $q_3$, $\epsilon_{r3}$ is associated with the bulk Silicon substrate.

Substituting the effective permittivity into equation 7.15 in all cases determines the resonant frequency for all these structures, see table 7.1 below. These values are used for comparisons with the measured values shown in chapter 11.

| CPR configuration | Environment | $\epsilon_r$ | $f_0\ Ghz$ |
|---|---|---|---|
| Nb/$Al_2O_3$ | Vacuum | 9.9 | 5.7095 |
| Nb/$Al_2O_3$ | Lq Helium | 9.9 | 5.6971 |
| Nb/$SiO_2$/Si | Vacuum | Si:11.9, $SiO_2$=4.9 | 5.6859 |
| Nb/$SiO_2$/Si | Lq Helium | Si:11.9, $SiO_2$=4.9 | 5.6721 |

*Tab. 7.1:* Table contains the CPR configuration, environment in which the CPR is measured, the permittivity of the substrates and the estimated geometric resonant frequency $f_0$.

# 8. SCATTERING PARAMETERS

For Transverse Electromagnetic (TEM) devices and non-TEM devices such as CPRs (quasi-TEM), it is difficult to define the voltage and current through these devices and extract the resonant properties. It is more appropriate to extract the resonant properties through measurements of the magnitude (inferred from the power) and phase of the standing wave. The extracted magnitude and phase generally come in the form of incident, reflected and transmitted waves and are given by the scattering matrix (or S parameters) [54].

The S matrix provides a complete description of the network as seen at its N ports (two ports for all CPRs considered here). They relate the voltage waves incident on the ports to those reflected from the ports. These scattering parameters are generally measured directly with a network analyzer and are described in this form in the results chapters.

For a 2-port network, where $V_n^-$ is the amplitude of the voltage wave incident on port n (1 or 2), and $V_n^+$ is the amplitude of the voltage wave reflected from port n, then the scattering matrix (S) becomes;-

$$\begin{bmatrix} V_1^- \\ V_2^- \end{bmatrix} = \begin{bmatrix} S_{11} & S_{12} \\ S_{21} & S_{22} \end{bmatrix} \begin{bmatrix} V_1^+ \\ V_2^+ \end{bmatrix} \tag{8.1}$$

To calculate all four of the S parameters for the 2-port resonator, requires the use of the ABCD matrix. The ABCD matrix takes into consideration the transmission for each 2-port network and includes both the current and the voltage. An example of this is given below:

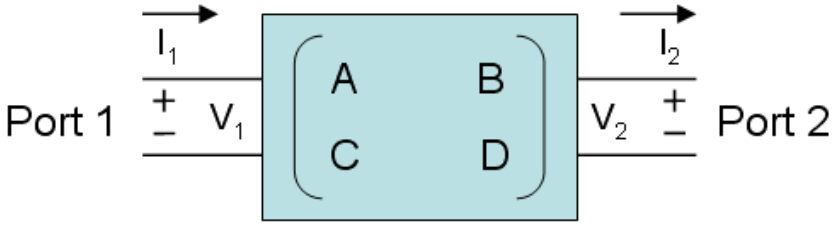


*Fig. 8.1:* A two port network circuit.

and in matrix form.

$$\begin{bmatrix} V_1 \\ I_1 \end{bmatrix} = \begin{bmatrix} A & B \\ C & D \end{bmatrix} \begin{bmatrix} V_2 \\ I_2 \end{bmatrix} \tag{8.2}$$

For various circuit configurations (series or shunt for example) there is a corresponding ABCD matrix. The ABCD parameters of four 2-port circuits that are used in this thesis are shown below:

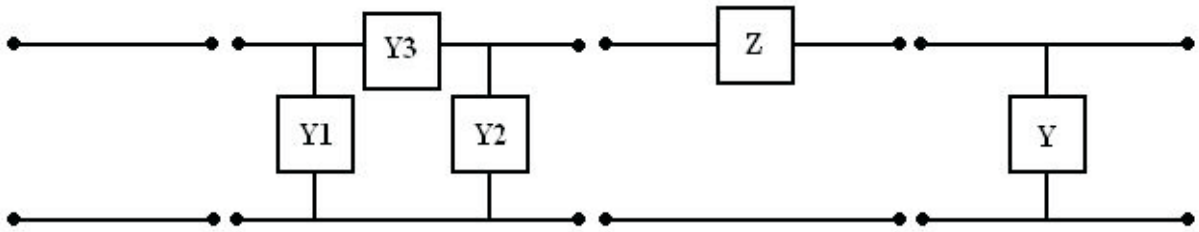


| | *Transmission Line* | *Coupling Capacitance* | *Series Impedance* | *Shunt Admittance* |
|---|---|---|---|---|
| $A$ | $\cos\gamma l$ | $1 + Y_2/Y_3$ | 1 | 1 |
| $B$ | $Z_0 \sin\gamma l$ | $1/Y_3$ | $Z$ | 0 |
| $C$ | $Y_0 \sin\gamma l$ | $Y_1 + Y_2 + Y_1Y_2/Y_3$ | 0 | $Y$ |
| $D$ | $\cos\gamma l$ | $1 + Y_1/Y_3$ | 1 | 1 |

*Fig. 8.2:* Circuit diagram and ABCD parameters for a transmission line, coupling capacitor, series impedance and shunt admittance. Taken from reference [55].

The first model represents a transmission line, where $\gamma = \alpha + j\beta$ is the transmission line wave propagation coefficient, $\alpha$ is the attenuation coefficient and $\beta \approx \omega/c$ is the wave propagation (c is the velocity of the travelling wave). $Z_0$ is the impedance of the

transmission line, and is generally set to 50 Ω as this is compatible with the majority of microwave components. $Y_0$ is the admittance of the transmission line and is inversely proportional to $Z_0$.

The second model is used to calculate the coupling capacitance, e.g. the coupling between the microwave circuitry and the half wavelength CPR. The third model is based on a half wavelength CPR and is represented by a series impedance. The last model represents a quarter wavelength CPR and is represented by a shunt impedance to ground.

The ABCD parameters used to infer the S parameters of these devices can be deduced using the S parameter matrix below [55].

$$\begin{bmatrix} S_{11}\, S_{12} \\ S_{21}\, S_{22} \end{bmatrix} = \frac{1}{Z_0A + B + Z_0^2C + Z_0D} \times \begin{bmatrix} Z_0A + B - Z_0^2C - Z_0D & 2Z_0(AD - BC) \\ 2Z_0 & -Z_0A + B - Z_0^2C + Z_0D \end{bmatrix} \tag{8.3}$$

The above tools are used to solve the S parameters of the coupling capacitance, the half wavelength CPR and the quarter wavelength CPR.

## 8.1 The Transmission Line.

As shown above, the transmission line wave propagation coefficient is described by $\gamma = \alpha + j\beta$, where $\alpha$ can be used to describe the loss and $\beta$ is inferred from the wave velocity of the $EM$ wave in the material. Transmission line loss is due to either the quasiparticles in the superconducting condensate and/or the lossy dielectric, and is generally small for Sapphire and Silicon substrates. To measure the loss in the transmission lines, it is better to express the transmission line parameters in terms of the resistance $R$, inductance $L$, conductance $G$, capacitance $C$, so that $\gamma = \sqrt{(R + j\omega L)(G + j\omega C)}$ and is rearranged to [55]:

$$\gamma = j\omega\sqrt{LC}\sqrt{1 - j\left(\frac{R}{\omega L} + \frac{G}{\omega C}\right) - \frac{RG}{\omega^2 LC}} \tag{8.4}$$

For low loss conductors $R << \omega L$ and for low loss dielectrics $G << \omega C$, then $RG << \omega^2 LC$ and the propagation constant reduces too:

$$\gamma = j\omega\sqrt{LC}\sqrt{1 - j\left(\frac{R}{\omega L} + \frac{G}{\omega C}\right)} \tag{8.5}$$

For zero loss $R/\omega L + G/\omega C$ term is ignored and this corresponds to $\alpha = 0$, i.e. the wave is not attenuated, and $\beta = \omega/\omega_0$ is simply the wave propagation through the device ($\omega_0$ is the resonant frequency). For the following solutions, it is assumed that the superconductor has zero loss as this simplifies the calculations.

## 8.2 Coupling Capacitance.

In Figure 8.2, the coupling capacitance is represented by $Y_3$, and $Y_1$ and $Y_2$ are the coupling capacitance to the box ground. The value of $Y_1$ and $Y_2$ is small compared with $Y_3$ because the separation between the superconducting ground planes and the box ground plane is large compared with the separation between the conducting strip and microwave circuitry.

Using the B parameter of the ABCD matrix ($B = 1/Y_3$) and the conversion chart between 2-port network parameters as set out by D. M. Pozar [55], then:

$$\frac{-1}{B} = -Y_3 = \frac{-Z_{21}}{Z_{11}Z_{22} - Z_{12}Z_{21}} = Y_{21} \tag{8.6}$$

Therefore $Y_3 = Y_{21} = Im(2\pi\omega_0 C_k)$ and hence the coupling capacitance ($C_k$) can be extracted directly from the network analyzer using the transmission admittance.

## 8.3 The Transmission Parameter for a Half Wavelength CPR.

For a half wavelength resonator coupled to two coupling capacitors, the ABCD parameters are determined using:

$$\begin{bmatrix} A & B \\ C & D \end{bmatrix} = \begin{bmatrix} 1 & Z_{in} \\ 0 & 1 \end{bmatrix} \begin{bmatrix} t_{11} & t_{12} \\ t_{21} & t_{22} \end{bmatrix} \begin{bmatrix} 1 & Z_{out} \\ 0 & 1 \end{bmatrix} \tag{8.7}$$

Firstly assume that the coupling capacitance are the same at both ends, therefore $Z_{in} = Z_{out} = Z_c$ and $Z_c = 1/j\omega C_k$, where $C_k$ is the coupling capacitance. The transmission matrix parameters given in figure 8.2 are:

$$t_{11} = \cos\gamma l \tag{8.8}$$

$$t_{12} = Z_0 \sin\gamma l \tag{8.9}$$

$$t_{21} = Y_0 \sin \gamma l \tag{8.10}$$

$$t_{22} = \cos \gamma l \tag{8.11}$$

As stated in section 8.1, when the loss-less CPR is on resonance $\gamma = \beta = \omega\sqrt{LC}$, where $L$ and $C$ are the inductance and capacitance of the CPR. The transmission matrix is simplified to:

$$\begin{bmatrix} t_{11} & t_{12} \\ t_{21} & t_{22} \end{bmatrix} = \begin{bmatrix} 1 & Z_0 \\ 0 & 1 \end{bmatrix} \tag{8.12}$$

The transmission through the CPR is given by:

$$S21 = \frac{2}{A + B/Z_0 + Z_0 C + D}$$

Using a small perturbation of $\beta$ away from resonance, e.g. $\beta = j\Delta\omega/\omega_0$, then the equation becomes:

$$S21 = \frac{1}{\cos(\beta l) + \sin(\beta l) + (Z_c/Z_0)(\sin(\beta l) + 2\cos(\beta l)) + (Z_c/4Z_0)^2 \sin(\beta l)} \tag{8.14}$$

Then S21 on resonance, where $\beta = 2n\pi/\lambda$ and looking at the fundamental mode, ($n = 1$ and $\lambda = 2l$) then $\beta l = \pi$, and $S21_0$:

$$S21_0 = \frac{1}{1 + 2Z_c/Z_0} \tag{8.15}$$

Ignoring the coupling capacitance, e.g. $C_k \to 0$, the resonant frequency is given by equation $f_0 = c/2l\sqrt{\epsilon_{eff}}$. As $C_k$ increases the resonant frequency is pulled lower. The new frequency is $f_0 = f_{0,0}(1 - 4f_{0,0}C_k Z_0)$, which is typically $1 - 2$ % correction to the resonant frequency.

For high unloaded $Q >> 1$, S21 is modified too:

$$S21 = \frac{2g}{1 + 2g + 2jQ\frac{f - f_0}{f_0}} \tag{8.16}$$

where $g = 2Q/\pi(2\pi f_0 C_k Z_0)^2$ is the coupling coefficient. The transmission parameter at resonance determined in terms of the coupling coefficient becomes:

$$|S21| = \frac{2g}{1 + 2g} = \frac{Q}{1 + \frac{4Q}{\pi}(2\pi f_0 C_k Z_0)^2} \tag{8.17}$$

The loaded $Q$ is related to the unloaded $Q$ by; $Q_l = Q/1 + 2g$.

## 8.4 The Transmission Parameter for a Quarter Wavelength CPR.

The quarter wavelength CPR that are currently used as kinetic inductance detectors (KID) are represented by a shunt admittance to ground, as shown in figure 8.2. The transmission parameter for this device is calculated in a similar way to that above.

Using the ABCD parameters shown in figure 8.2, with the conversion to the transmission parameter as shown in equation 8.3, and $Y = 1/Z_i$ which is the impedance associated with inserting a quarter wavelength CPR near to the transmission line, S21 on resonance becomes:

$$S21 = \frac{2}{2 + Z_0/Z_i} \tag{8.18}$$

Here $Z_0$ is the characteristic impedance of the transmission line. When the frequency of the microwave source is set far from the resonance of the quarter wavelength CPR, S21 tends to unity. Near resonance $Z_i$ reduces and on resonance it reaches a minimum. The transmission on resonance in that case is equal to $S21_0 = 2/(2 + g)$, where $g$ is the coupling of the quarter wavelength CPR to the transmission line.

# 9. SIMULATIONS: CAPACITANCE AND LOSS TANGENT ON THE $Q$ OF A CPR.

Simulations are made in high frequency structure simulator (HFSS) and Microwave Office (MWO) (see appendix A for the method for simulating these structures). The coupling capacitance and associated coupling $Q$ is simulated in HFSS and the effect of varying the loss tangent on the resonant frequency is simulated in MWO. The coupling gap for a half wavelength CPR is shown below:

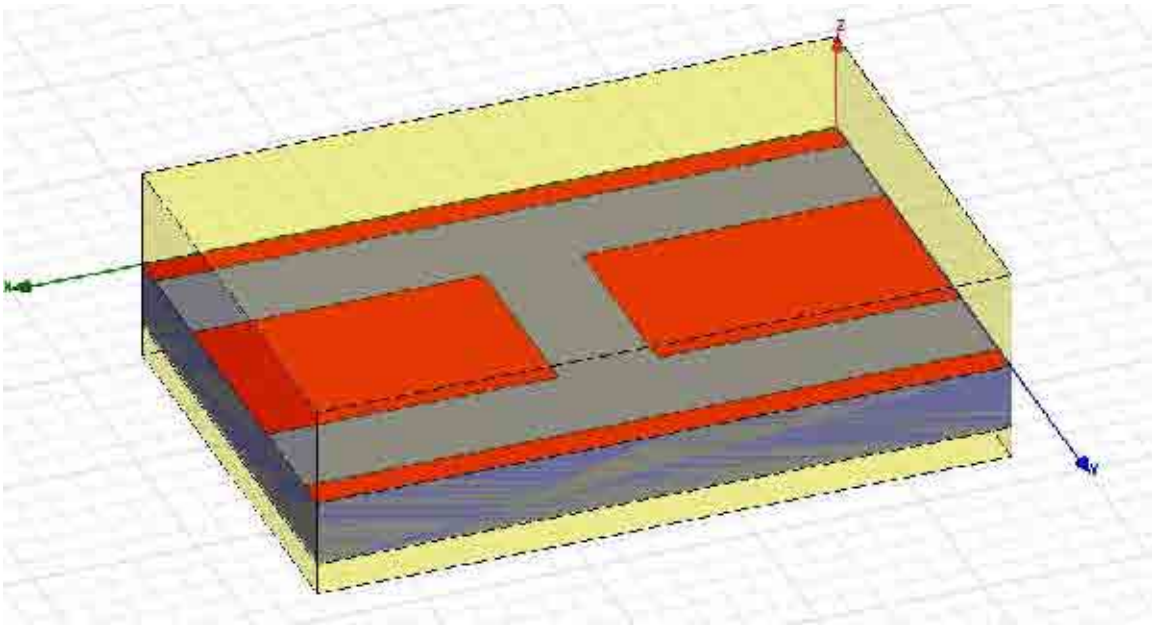

*Fig. 9.1:* A diagram of the coupling capacitor. The coupling gap is a 2D perfect electrically conducting (PEC) film, residing on a silicon dielectric substrate (with $\epsilon = 11.9$ [56]) and enclosed in a box. The size of the box is $x = 140$, $y = 70$, and $z = 30$ $\mu$m

Applying an electric ($E$) field across a parallel plate capacitor produces effects that are different from a thin film capacitor, and therefore the capacitance of a thin film is not assumed to follow $C = \epsilon_0 \epsilon_r A/d$ (where $\epsilon_0$ and $\epsilon_r$ are defined previously, $A$ is the cross-

sectional area of the capacitor, and $d$ is the separation of the two plates). The $E$ field applied to a thin film capacitor extends some distance into the plane of the film. Calculating the capacitance therefore becomes difficult, so a finite element software simulator such as HFSS is employed to simplify this process.

The surface of the capacitor is simulated as a perfect electrical conductor (PEC) and resides on a Silicon substrate with $\epsilon = 11.9$ [56]. The capacitor and substrate are enclosed in a box, and the wall sides are defined by PEC boundaries. Lumped ports are placed at the ends of the thin film capacitor in the $yz$-plane and the direction of the $E$ field is defined by an integration line that extends from the middle of the $y$-plane at the centre of CPR and extends to the end of the box.

The real, imaginary and magnitude of the impedance of the structure is calculated below:

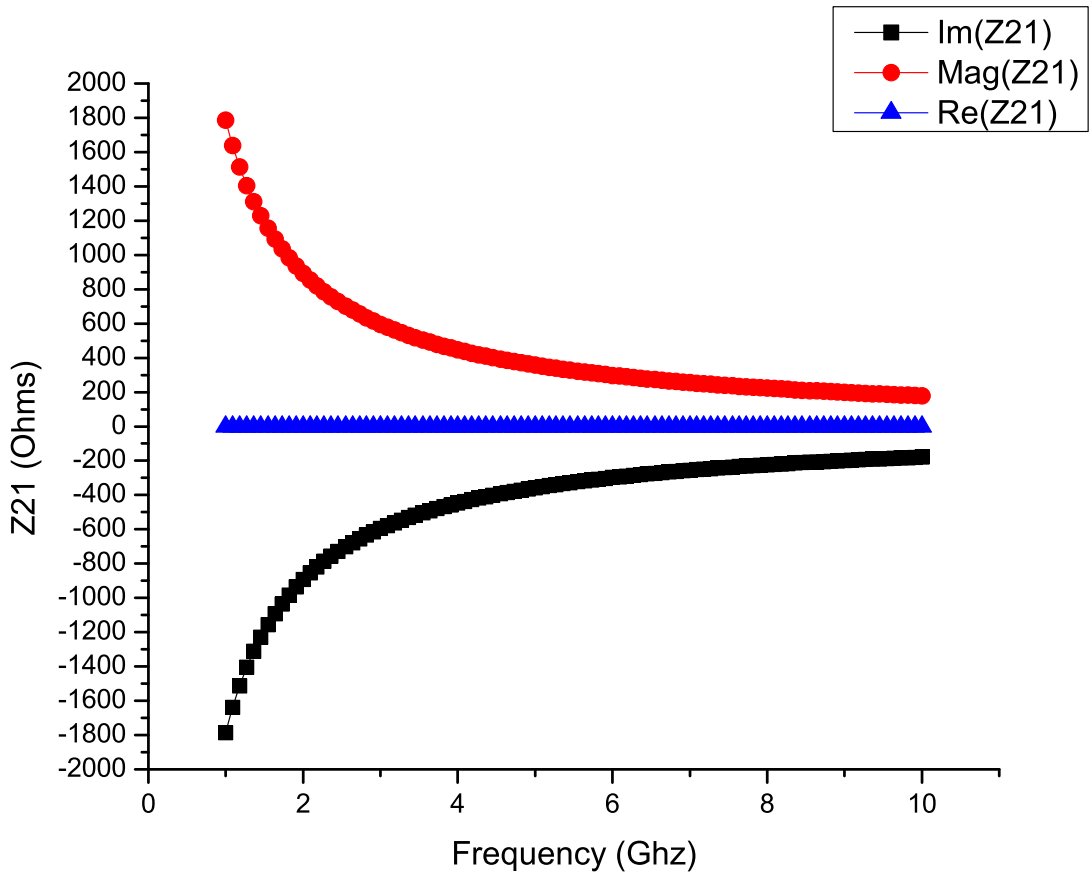


*Fig. 9.2:* The real, imaginary and magnitude of the impedance from port 2 to port 1 as a function of frequency.

This is consistent with what is expected for a capacitor. For example, the real part of the impedance is zero, because the reactance of a capacitor is given by $X_c = 1/\omega C$, hence purely imaginary. The magnitude of the impedance is
$Mag(Z21) = \sqrt{(Re(Z21))^2 + (Im(Z21))^2}$, therefore $Mag(Z21) = Im(Z21) = 1/\omega C$.

The capacitance is extracted using the $Y$ parameter and $c = 2\pi\omega Im(Y21)$ (as shown in section 8.2). The following graph is obtained:

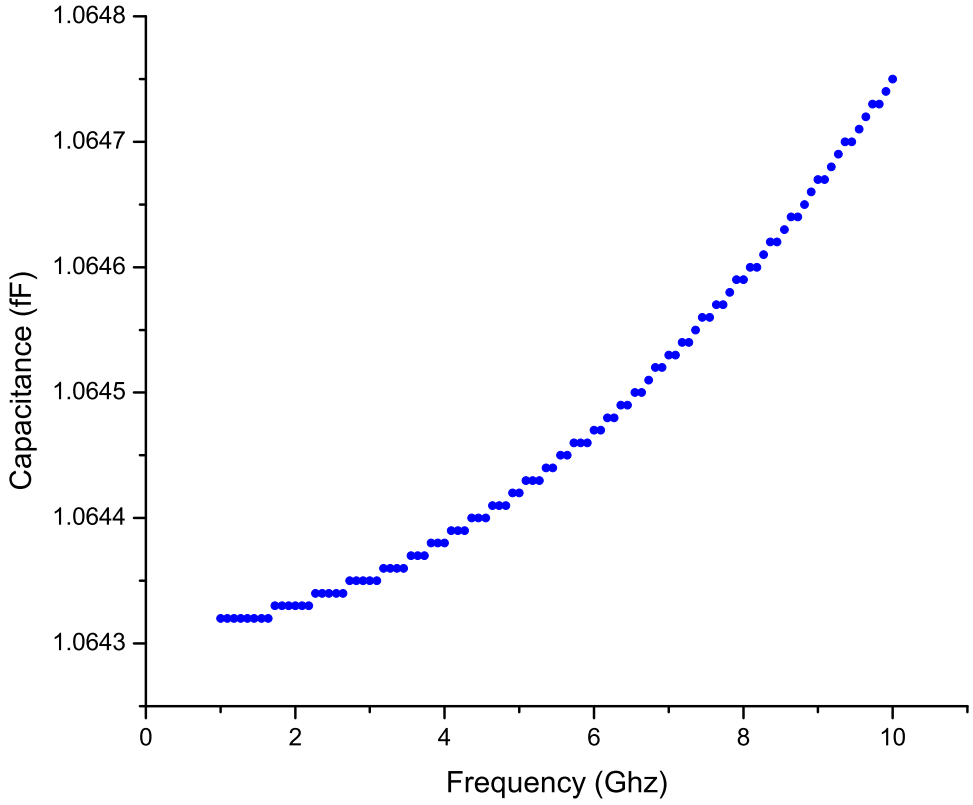


*Fig. 9.3:* The capacitance of a coupling capacitor of a half wavelength resonator as a function of frequency for a Niobium CPR on a Silicon substrate (with $\epsilon = 11.9$) with a coupling gap of 16 $\mu$m and strip to separation width; $s = 30$ and $w = 15$ $\mu$m.

The capacitance of the gap at 6 Ghz is 1.065 fF, using $Q = \omega c/g$ (as shown in section 8.3) then, $Q = 82,277$.

The coupling capacitance for a CPR with $s = 10$ $\mu m$ and $w = 5$ $\mu m$ and varying the coupling gap is given below.

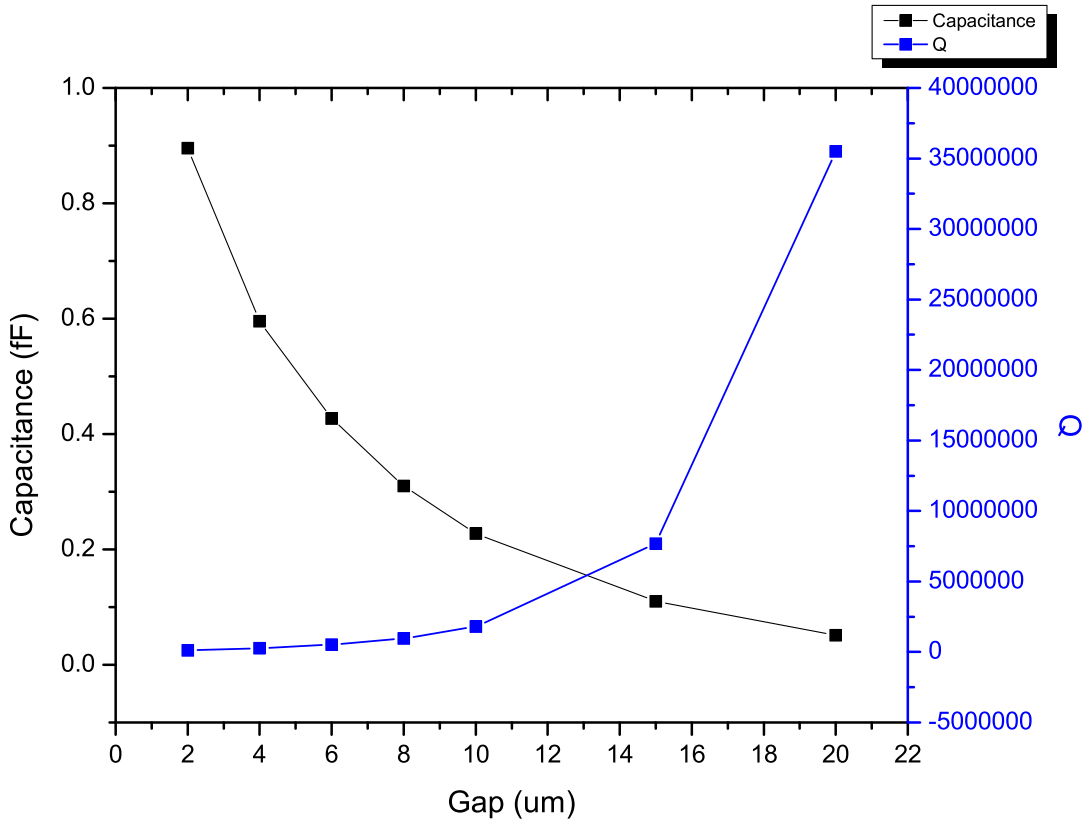


*Fig. 9.4:* The coupling capacitance and $Q$ as a function of a single gap on a CPR as measured at 1 Ghz.

The above graph demonstrates that by increasing the size of the gap, the capacitance reduces and the coupling $Q$ factor increases. It should be noted that within this model, there is no loss introduced in the substrate or surface conductor, therefore the $Q$ in this case is associated with the impedance of the gap and the coupling to the 50 $\Omega$ ports.

It is reported by Frunzio *et al* [5], that the coupling capacitance of their 4 $\mu m$ gap resonators is $\approx$ 0.3 fF. These simulations undertaken in HFSS produce coupling capacitances of 0.59 fF for a single gap. This value is of the same order of magnitude as reported by Frunzio *et al*, therefore these values are consistent.

Internal loss in the CPR structure is introduced by varying the loss tangent of a Silicon dielectric substrate. The loaded $Q$ factor behaves inversely proportional to the loss tangent of the substrate, see figure below.

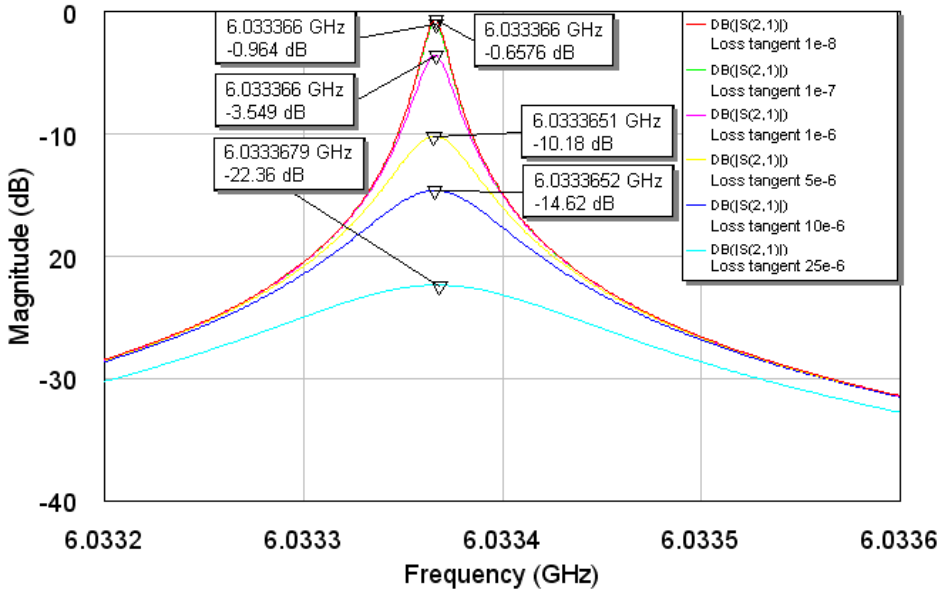


*Fig. 9.5:* Simulation of the transmission spectrum of a Niobium CPR on a Silicon substrate with dimensions $s = 10$ $\mu$m, $w = 5$ $\mu$m with different loss tangents

The loss tangent for Sapphire and Silicon Dioxide on top of Silicon for temperatures $< 4$ K is $\tan\delta \sim 10^{-6}$ [57, 58, 59] and therefore $Q_{substrate} \sim 10^6$.

# 10. EXPERIMENTAL SET-UP

To measure the resonant parameters of CPRs, the following techniques are employed. There are two types of cryostat used in this project and the operation of both are discussed. They are the liquid Helium filled glass cryostat and the carbon fibre cryostat where the sample is placed in a vacuum can. A discussion follows about the sample box and CPR mounting, followed by a discussion about the thermometry and microwave control system.

A simple block diagram below demonstrates how a CPR is measured.

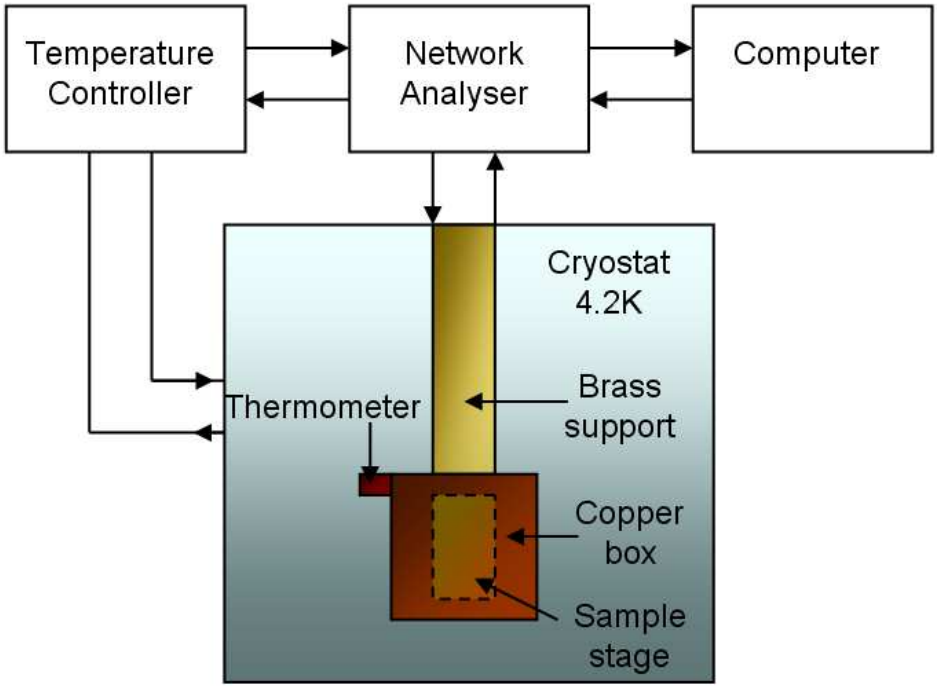


*Fig. 10.1:* Block diagram of the circuit employed to measure CPRs.

These CPRs are operated at low temperatures. The temperature is measured by two thermometers placed around the CPR, and the CPR is measured with a network analyzer. A program written in Labview is used to initialize and probe CPR parameters and record

the temperature of the system. This information is collected, interpreted and results are given in the following sections.

## 10.1 Measurement Technique.

To test the CPR requires a cooling device that can achieve temperatures $\sim 10\%$ of their superconducting transition temperatures. For Niobium resonators this is around 1 K. This can easily be achieved by using a glass cryostat and pumping on the liquid Helium to reduce its vapour pressure. The CPR in this case is placed in direct contact with the liquid Helium bath. The second method for measuring these CPRs is a carbon fibre cryostat, encasing the CPR within a vacuum can. In this case the temperature is reduced by pumping on the liquid Helium within a 1 K pot contained within the vacuum can, and cooled via conduction through the brass and copper supports. A diagram of both cryostats are shown below.

*Fig. 10.2:* Liquid Helium pumped glass cryostat.

*Fig. 10.3:* Photograph of the carbon fibre cryostat and equipment. At the bottom of the cryostat is a Helmholtz coil positioned on a lazy Susan, used to apply a magnetic field with easily adjustable orientation.

Upon achieving a low temperature with these cryostats, a microwave signal is initiated by a computer program written in Labview [60] shown in appendix B, and generated by a microwave automated network analyzer (ANA) (HP model 8720).

The output microwave signal is guided from port one of the ANA, through semi-flexible coaxial cables to the roof of the glass cryostat. SMA (sub miniature version A) connectors are then used to make a transition from semi-flexible coaxial cables outside the cryostat to rigid copper 2.2 mm coaxial cables ($\approx 2$ dB/m attenuation) inside the glass cryostat.

The set-up for the carbon fibre cryostat and vacuum can is similar to that described above. The difference is that within the cryostat the coaxial cables are made from 2.2 mm CuproNickel (CuNi) coaxial cables and then on entering the vacuum can, the cables are changed to 1 mm brass coaxial cables. This is to ensure adequate heat sinking of the wires, to avoid thermal conduction (heat leaks) from the warmer environment outside the vacuum can, that can be transfered to the sample inside the vacuum can.

For both cryostats, the coaxial cables facilitate the microwave signal down to SMA connectors attached to the outside of the copper box that house the CPR. Inside the box are four SMA launchers. The SMA launcher consists of an outer ground connector and inner launcher pin. The inner launcher pin sits on the inner conductor of a copper coated Duroid substrate [61]. This Duroid substrate and Niobium CPR sample resides is a gold coated Copper box, as shown in figure 10.6. This copper coated Duroid (RT 5880.01, thickness 2mm and $\epsilon$2.2) substrate is patterned in to a Coplanar transmission line (size of board: 5 cm x 7 cm x 2 mm), with a designed impedance of 50 $\Omega$. The outer connector sits on the ground plane of the transmission line. The CPR is placed in a gap in the middle of this coplanar transmission line, see figure 10.4. There have been measurements undertaken on a Gold Alumina Coplanar transmission line, patterned similar to that shown in the figure below (size of board: 5 cm x 7 cm x 400 $\mu$m). Aluminium wire bonds are used to connect both the inner and outer parts of the transmission line to their respective parts on the CPR chip, see figure 10.5 below.

The same microwave set-up exists on the other side of the CPR running from cryogenic temperatures to room temperature. On receiving the signal from the device, this is further analyzed using the Labview program to read the information from the ANA.

Additional coaxial cables are added to either pass a dc/ac current or a pulsed microwave signal to the CPR chip. This set-up is the same as that described above. The current passed down the coaxial cables is used to manipulate the resonant frequency of the CPR. The pulsed microwave signal is used to manipulate the state of the coupled CPR/QUBIT system.

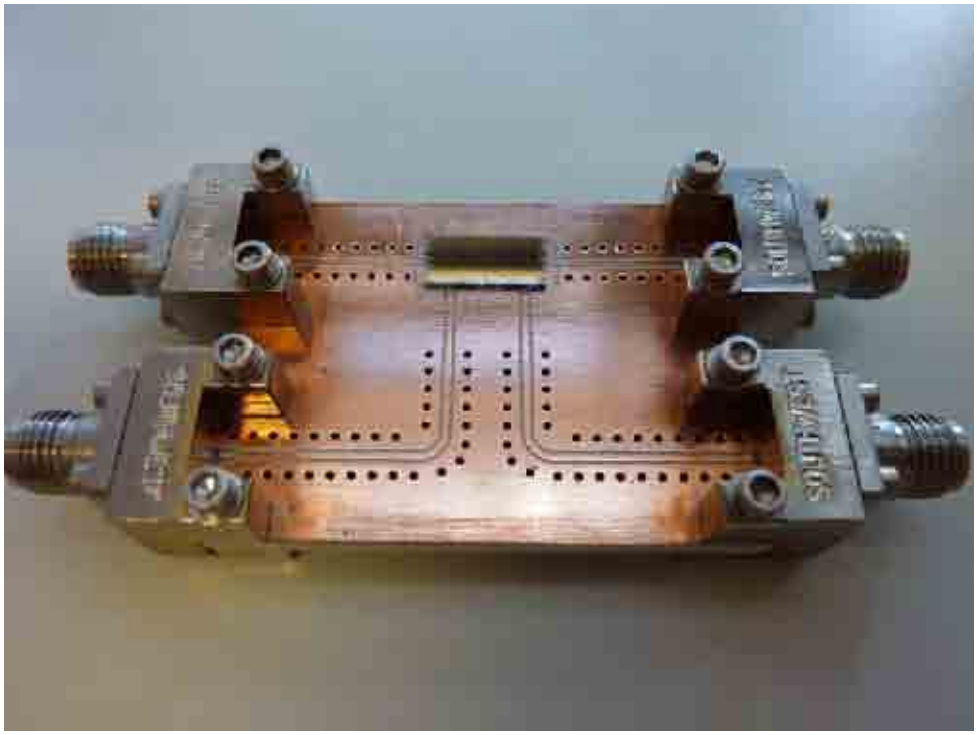

*Fig. 10.4:* A photograph of the Copper transmission line and sample. Two of the SMA connectors are used for the microwave signal, the other two SMA connectors are used as current control lines.

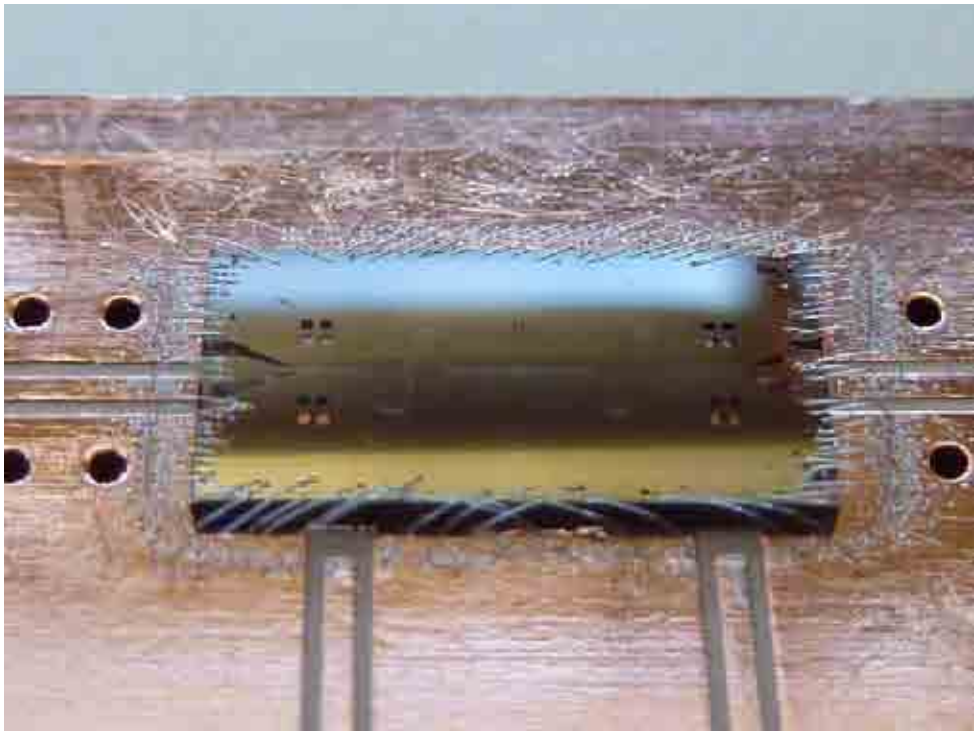

*Fig. 10.5:* A photograph of the CPR chip, wire bonds and Copper coplanar transmission line. Vias can be seen in the duroid substrate, electrically and thermally connecting the top electrode with the bottom. These vias act to reduce slot line modes, that can be potentially generated in the substrate.

The Alumina and Duroid board contain vias connecting the top ground plane with the bottom ground plane. These vias are placed every $d \sim \lambda_0/10$ (where $\lambda_0$ is the standing wavelength of the CPR), as this eliminates undesired frequency modes (e.g. slotline modes) that exist within the substrate.

## *10.2 The Copper Box and Sample Mounting.*

The box is made from high conductivity Copper because it has a very high electrical conductivity and a short skin depth compared with other metals (see section 4.3). The box is then coated with Gold, to stop the Copper from oxidizing.

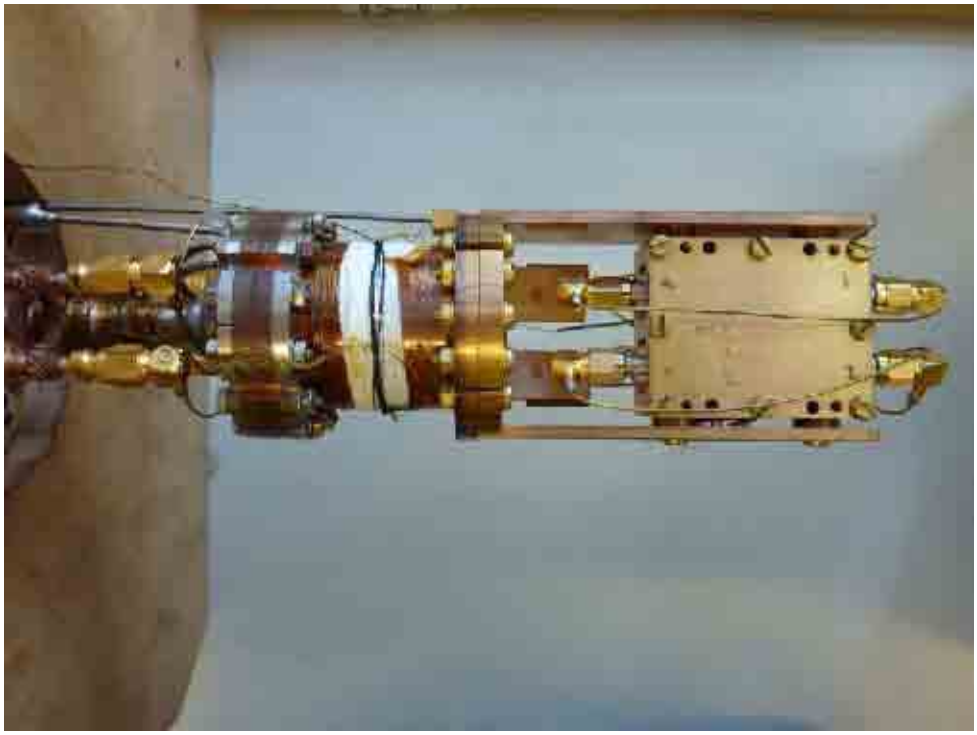

*Fig. 10.6:* Photograph of the sample stage. Shown from left to right is the 1 K pot, followed by the Copper plates for heat sinking the coaxial cable, and followed by the sample box.

Since the box has a high electrical conductivity, then the losses generated by box modes are lower hence $Q_{box}$ is higher (as described in section 5). If a box mode exists close to the frequency of the CPR, since $Q_{box}$ is high, its FWHM is low, and hence it is unlikely that the box mode will coincide and interfere with the resonance of the CPR. Any such interference or coupling of a box mode to the CPR mode will cause the CPR mode to be limited by the $Q$ of the box (as the $Q$ for the metal box is generally lower then the superconducting CPR) and therefore generate unreliable results [42].

## *10.3 Fabrication.*

The first stage of fabricating these sample is to design a photolithographic mask, see appendix C. The photolithographic mask contains samples with different capacitive couplings and different conducting strip to strip separations based on the simulations made in section 9. The mask is designed in KIC [62], an integrated circuit layout editor, and is

exported as a GDS file that is compatible with mask fabricators.

The mask is subsequently sent to Toppan [63] for fabrication. Niobium on single crystal Sapphire and Niobium on Silicon Dioxide on top of high resistivity Silicon samples are prepared by Starcyro [64]. The Niobium is 250 nm thick with a 2 nm uniformity. The Sapphire and Silicon substrates are 400 $\mu$m thick and the Silicon Dioxide layer is thermally grown on top of the Silicon to a thickness of 400 nm. These thin films have been processed by the author and by Starcyro.

The samples that are prepared by the author are fabricated by the method shown in figure 10.7

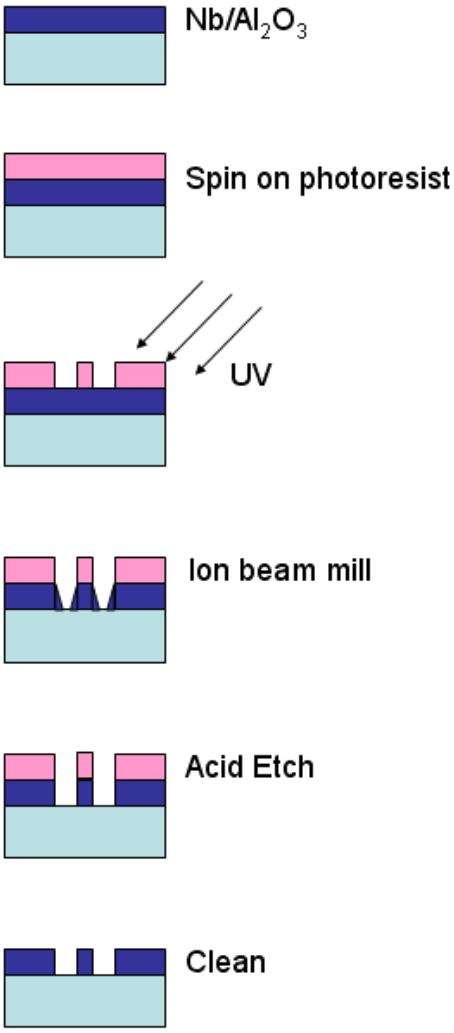


*Fig. 10.7:* A diagram of the steps taken to fabricate a CPR.

The first step to fabricate these samples is to spin a positive photoresist on to the surface of a sample. This is pre-baked at 100 $^0$C for 5 minutes. The photoresist is then exposed to UV under a Karlsuisse Mask aligner, developed and post-baked at 95 $^0$C for 3 minutes. The sample is then placed in an Argon Ion Beam miller to etch the Niobium. This is not a particularly clean method for removing Niobium, see the Atomic Force Microscopic image shown in figure 10.8, therefore subsequent etching is required.

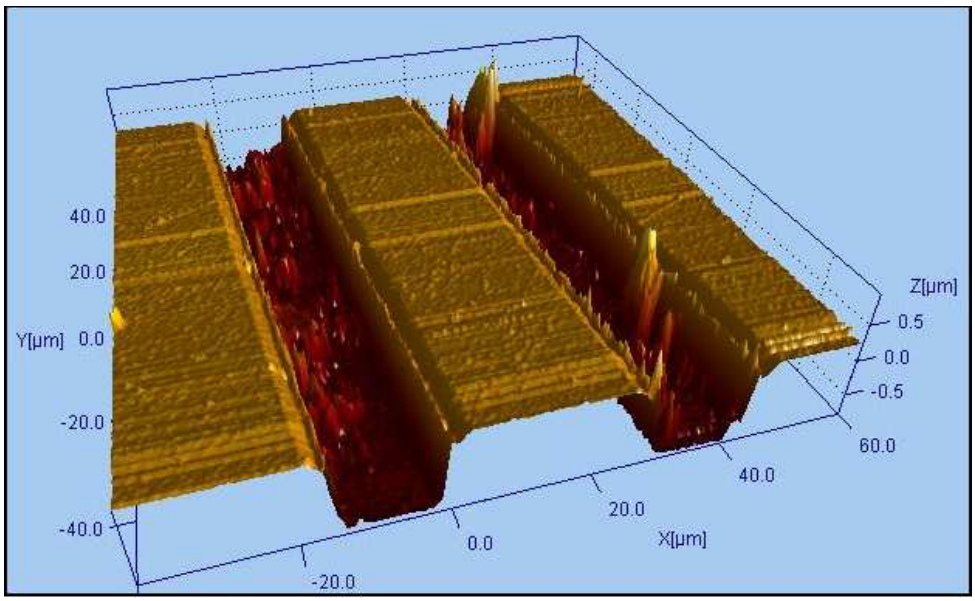


*Fig. 10.8:* AFM images of a niobium CPR on a oxidized Silicon substrate.

The etch that is used is a combination of Hydrofluoric acid, Nitric Acid and water in the following combination: 1 Hf : 9 $HNO_3$ : 20 $H_2O$ (On recommendation from StarCryo [64]). This produces smoother edges, which is crucial for CPRs since the microwave current is mostly concentrated at the surface and edges.

## *10.4 Temperature Measurement and Control.*

The lakeshore 340 temperature controller is used to measure the temperature at the base of the cryostat. The temperature sensor that is used is a calibrated Cernox sensor (CX-1010-MT) [65], calibrated from 100 mK to room temperature. To measure the temperature of the system, a four terminal measurement is made. This is achieved with two twisted

pairs of CuproNickel (CuNi) wires, with I+ and I- wires connected to opposite legs of the Cernox sensor, and likewise for V+ and V-. Twisted paired wires ensure external radiation does not interfere with the measurement system, because the loop inductance has been minimised, and therefore the flux in the loop has been reduced.

At the top of the cryostat, the wires are attached to a 6 pin-D plug and socket, and a further cable is used to connect the measurement system to the back of the temperature controller. The Lakeshore temperature controller reads the sensor units, in this case the resistance of the Cernox sensor, and this is converted to a temperature using the calibrated data values provided with the sensor. This is sent to the GPIB card that is connected to the computer. A Labview program is then used to record this data and store it in a file, see appendix B.

Within the liquid Helium filled glass cryostat, the Cernox thermometer is placed next to the CPR sample. Within the Carbon fibre cryostat, the Cernox thermometer is placed directly onto the 1 K pot. A second RuO sensor (calibration data in Appendix D) is then added to the bottom of the sample stage, on to the sample box and is wired in the same way as described above.

## *10.5 Magnetic Field Measurement Set-up.*

There are two ways to apply a magnetic field to the sample. The first is via a Helmholtz coil positioned externally to the cryostat, as shown in figure 10.3. The arrangement of these coils means that a field of $\approx 1$ mT can be achieved at the centre of the cryostat. The second method is via a current control line patterned into the Niobium film, as shown in figure 10.9.

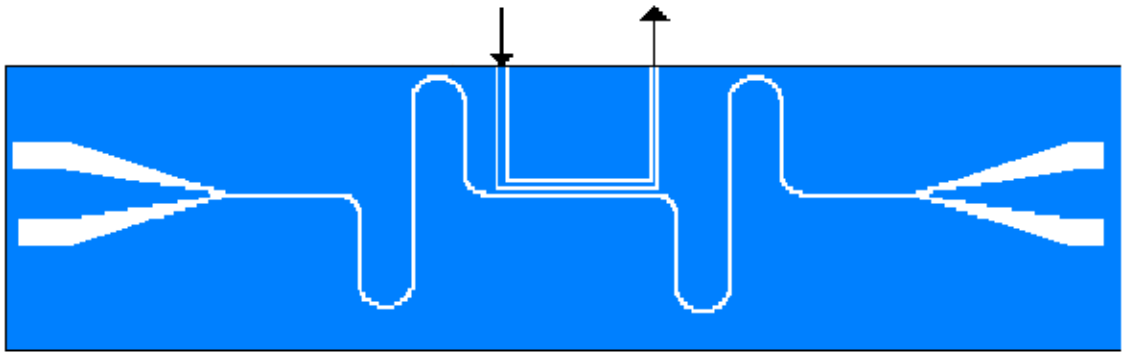

*Fig. 10.9:* CPR with current control line. The arrows dictate the direction of the applied current.

Another method to perturb the resonant frequency of the CPR, is coupling the CPR to an RF QUBIT patterned into the Niobium film, see figure 10.10.

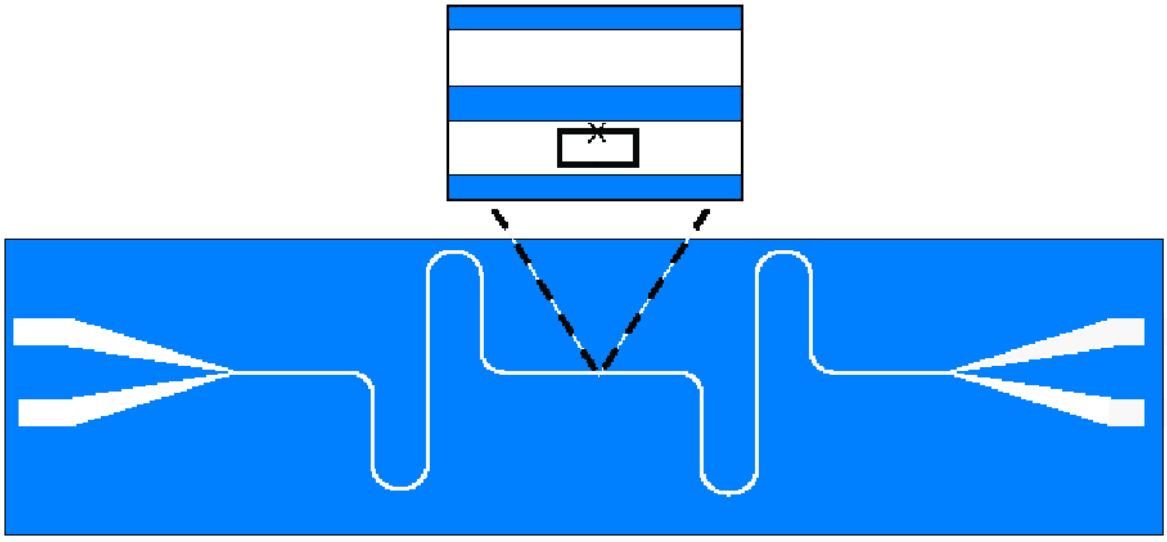

*Fig. 10.10:* CPR with enlarged RF QUBIT in the centre of the CPR.

These structures are patterned using the method shown in figure 10.7.

# 11. NIOBIUM ON SAPPHIRE AND OXIDIZED SILICON RESONATOR MEASUREMENTS

The primary aim of this work is to design CPRs with high $Q$ factors for the purpose of providing an investigative tool suitable for scientific research into quantum computing and cavity quantum electrodynamics [1, 2]. This is achieved by measuring the resonant frequency and $Q$ in terms of changes in temperature, power and magnetic field. High $Q$ CPRs are obtained by investigating device material and geometry. CPRs are measured at low temperatures in two cryostats; liquid Helium filled glass cryostat denoted by cryostat 1, and carbon fibre cryostat denoted by cryostat 2.

The resonant frequency and $Q$ factor are extracted from the transmission parameters of the microwave signal through the CPR cavity. An example of this is shown in figure 11.1.

The typical transmission spectrum of an ideal half wavelength CPR is shown in figure 1.3. Off resonance there is no transmission of the microwave signal, and on resonance there is maximum transmission of the microwave signal. The off resonance response for a non-ideal CPR, results in some transmission of the microwave signal through the cavity. On resonance the microwave signal is not fully transmitted, see figure 11.1.

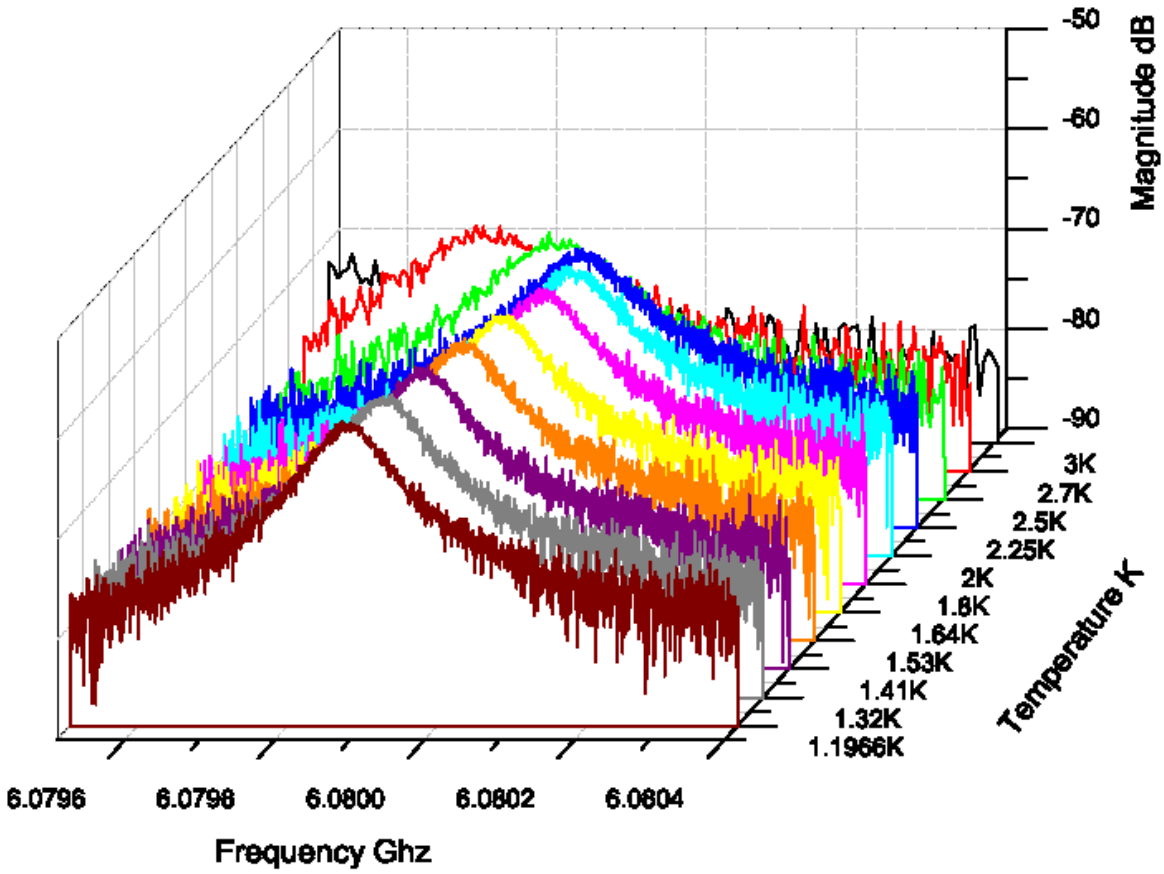


*Fig. 11.1:* Frequency and magnitude versus temperature for a Niobium on oxidized Silicon substrate CPR with parameters $w = 5$ $\mu$m, $s = 10$ $\mu$m, $l = 11$ mm and 6 $\mu$m gaps, measured in a liquid Helium filled glass cryostat.

This measurement is made on a patterned Niobium thin film deposited on top of an oxidized Silicon Substrate. The CPR parameters are $s = 10$ $\mu$m, $w = 5$ $\mu$m, $l = 11$ mm and 6 $\mu$m coupling gaps measured in the liquid Helium filled glass cryostat. The transition temperatures of these CPRs is $T \sim 9.2$ K as determined from SQUID magnetometre measurents.

Additional device parameters investigated are CPRs with conductor strip to strip separation; $s = 10$ $\mu$m, $w = 5$ $\mu$m, and $s = 30$ $\mu$m, $w = 15$ $\mu$m with various coupling capacitors. The device materials investigated are Niobium CPRs on Sapphire and oxidized Silicon substrates.

The high $Q$ measured here is due to the weak coupling of the CPR to the microwave

circuitry. A high CPR $Q$ factor results in low photon loss rate and longer coherence time between CPR and QUBIT systems. These CPR/QUBIT systems can thus be implemented to realise quantum bit experiments. Fabrication of CPR devices are achieved by photolithography and Argon ion beam milling (described in section 10.3). QUBITs are fabricated by electron beam lithography.

Electron beam lithography is a process for fabricating micron sized features in a thin film resist, by exposure to a high energy density beam of electrons. The primary electrons in the incident beam lose energy upon entering the material through inelastic scattering or collisions with other electrons. These primary electrons from the incident beam with sufficient energy to penetrate the photoresist, can be multiply scattered over large distances from underlying films and/or the substrate. This leads to exposure of areas at a significant distance from the desired exposure location [66]. This effect is significant in Sapphire substrates, and leads to over exposure of the photoresist and poor QUBIT resolution. Oxidized Silicon is proven to work better with electron beam lithography processes [66]. Both Sapphire and oxidized Silicon substrates are investigated because of their inherent low loss, but their usefulness in the study of quantum effects in quantum computing and cavity quantum electrodynamics maybe limited due to fabrication limitations.

## 11.1 Frequency Versus Temperature Measurements

The resonant frequency is determined by the kinetic and geometric inductance, and the capacitance of the CPR. The full equation for determining the resonant frequency as a function of temperature is found in chapter 7:

$$f(T) = \frac{1}{2l\sqrt{\mu_0 \epsilon_{eff}(T)\epsilon_0}}\left(1 - \frac{C\lambda_L(T)}{2ADK(k')}\left(\frac{1.7}{sinh(t/2\lambda_L(T))} + \frac{0.4}{\sqrt{[(B/A)^2-1][1-(B/D)^2]}}\right)\right) \tag{11.1}$$

Two unknowns from the equation above are the effective permittivity of the substrate (R-plane sapphire $\epsilon_{Al_2O_3} \sim 9.9$ [53], Silicon Dioxide $\epsilon_{SiO_2} \sim 4.5$ [56], and Silicon $\epsilon_{Si} \sim 11.9$ [56]) and the penetration depth of the superconductor $\lambda_L(T)$. The other factors are associated with the geometry of the CPR.

The dielectric constant is used to predict the geometric frequency, and the penetration depth is used to predict the correct functional form of the temperature dependence. In this model the temperature dependence of the dielectric constant of both Sapphire and oxidized Silicon is neglected as it does not change significantly at these low temperatures [47, 48].

The resonant frequency and $Q$ are measured as a function of temperature in cryostat 1 (the liquid Helium filled glass cryostat), for a Niobium CPR on Sapphire substrate with CPR parameters; $s = 10$ $\mu$m, $w = 5$ $\mu$m, $l = 11$ mm and 6 $\mu$m coupling gaps.

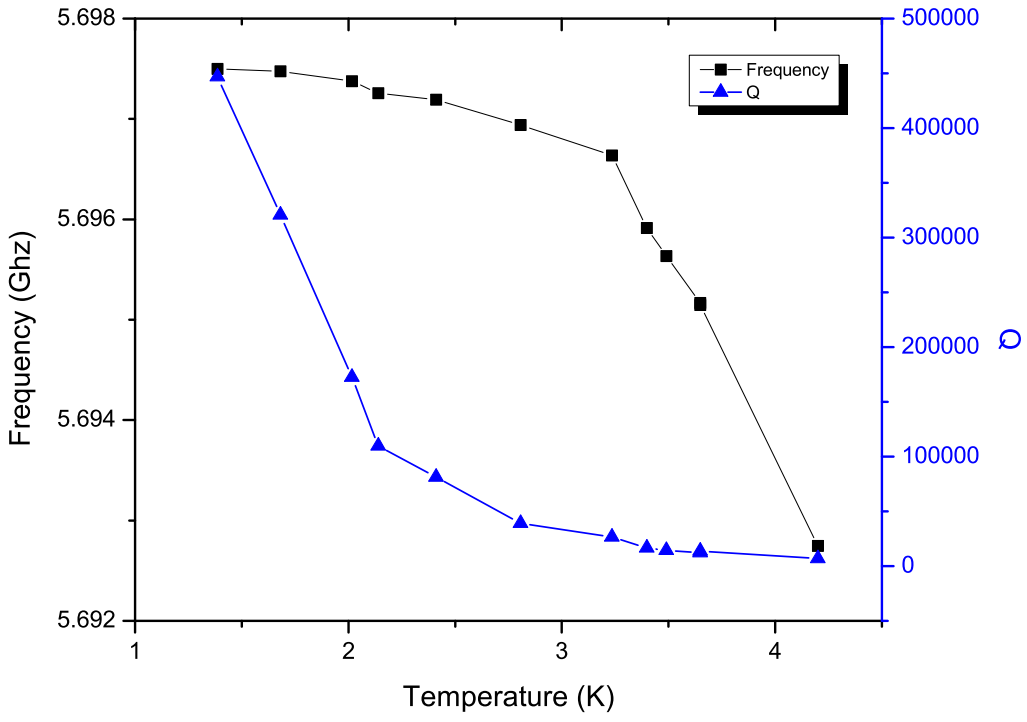


*Fig. 11.2:* Resonant frequency and $Q$ measured as a function of temperature for a $Nb/Al_2O_3$ CPR with parameters; $s = 10$ $\mu$m, $w = 5$ $\mu$m, $l = 11$ mm and 6 $\mu$m coupling gaps, measured in cryostat 1.

The resonant frequency, $Q$ and fitting data are plotted below as a function of temperature for the same CPR as above, and measured in cryostat 2.

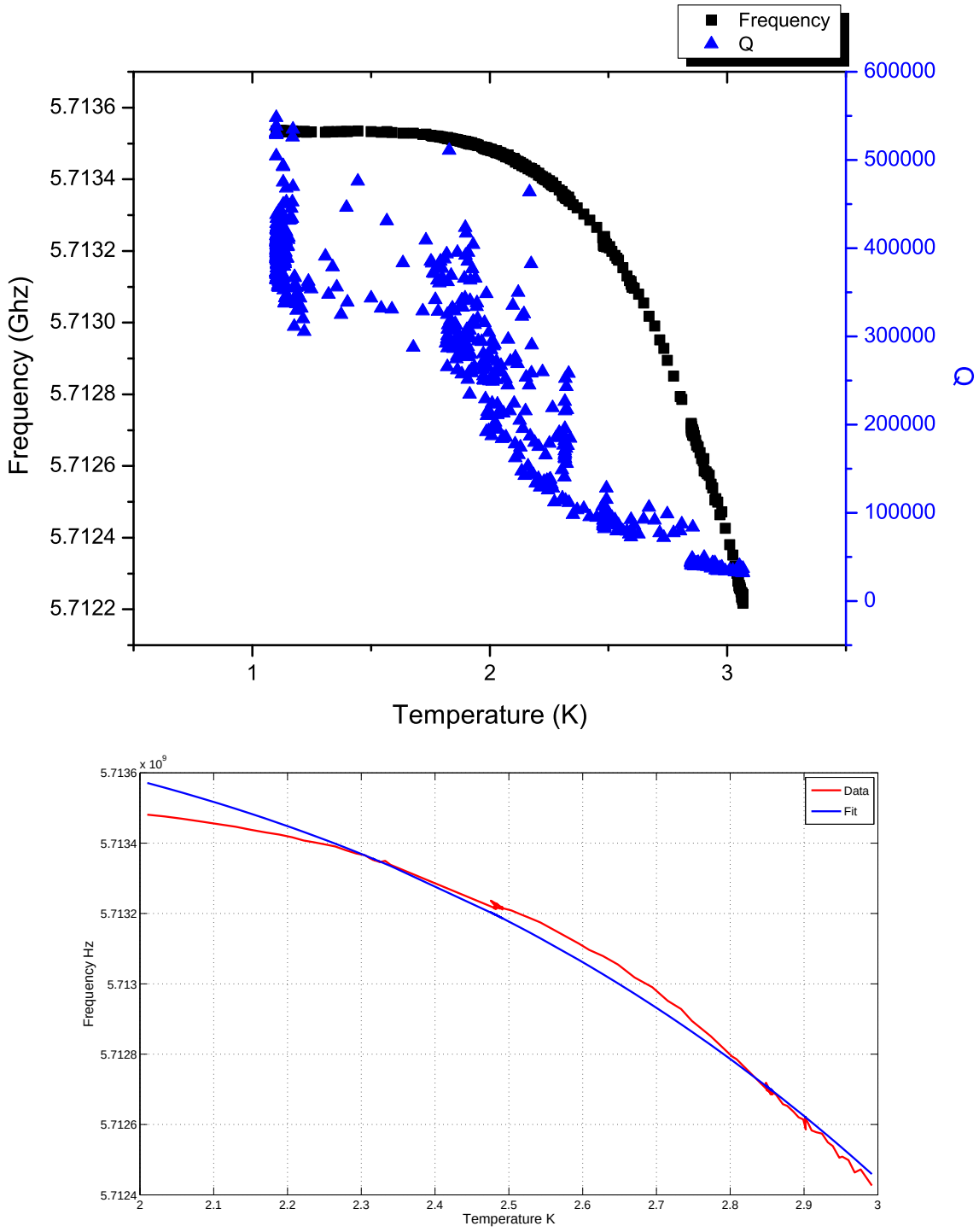


*Fig. 11.3:* Resonant frequency and $Q$ measured as a function of temperature for a $Nb/Al_2O_3$ CPR with parameters; $s = 10$ $\mu$m, $w = 5$ $\mu$m, $l = 11$ mm and 6 $\mu$m coupling gaps, measured in cryostat 2. The figure below contains the resonant frequency fit to the data described in appendix F.2, the penetration depth used here is based on London theory [33].

The process for fitting the function to the resonant frequency data is described in appendix F.2. This fitting process is based on the Nelder-Mead method [67], which is a direct search method of optimisation, based on evaluating the function with estimated values of $\lambda_0$ and $\epsilon_r$. Evaluating the difference between the square of the measured resonant frequency and the estimated resonant frequency gives an estimate on how good the fit is. Choosing new values of $\lambda_0$ and $\epsilon_r$, and re-evaluating this function, means that it is possible to converge on a solution on completing a number of iterations.

Data extracted from the fit in figure 11.3 are $\epsilon_{Al_2O_3} = 9.312$, and penetration depth $\lambda_L = 118.05$ nm. The estimated value of the permittivity of the Sapphire substrate is a reasonable estimate and the penetration depth is of the correct order of magnitude.

The same fitting process applied to results generated from a $Nb/SiO_2/Si$ CPR with parameters; $s = 10$ $\mu$m, $w = 5$ $\mu$m, $l = 11$ mm and 6 $\mu$m coupling gaps measured in cryostat 2, are $\epsilon_{eff} = 1 + q_3(\epsilon_{Si} - 1) + q_1(\epsilon_{SiO_2}) = 4.8741$ and penetration depth $\lambda_L = 87.31$ nm.

The value for the penetration depth of bulk Niobium at $T = 0$ K is 39 nm [31]. The penetration depth for thin films differs from the bulk value, and the amount it differs by is recorded in reference [68]. For a film thickness of 100 nm, the penetration depth is found to be $\lambda_0 = 100$ nm. The penetration depth of $\approx 118$ nm obtained from the fitting process is therefore a reasonable estimate.

The scatter on the measurements of the $Q$ factor are most likely associated with flux jumps in the Niobium film. These flux jumps contribute a resitive element in the microwave circuity altering the losses and hence the $Q$ of the CPR.

The temperature recorded in figure 11.2 in cryostat 1 is measured with a Mercury manometer that responds to changes in the vapour pressure of liquid Helium. There are some inaccuracies in the measured temperature values below $T = 2$ K when it becomes difficult to read the manometer. The data points in figure 11.3 are taken with a RuO sensor and the swept temperature is recorded. The second data set contains more temperature points, therefore to compare figure 11.2 with figure 11.3, it is appropriate to manipulate the second data set rather than the first.

To compare the data sets, the data in figure 11.3 is manipulated to include the temperature dependence of the permittivity of liquid Helium, see appendix E and reference [69]. This is achieved using the following equation:

$$f_{modified} = f_{meas}\sqrt{\frac{1 + q_1(\epsilon_{Al_2O_3} - 1)}{1 + q_1(\epsilon_{Al_2O_3} - 1) + q_3(\epsilon_{hel}(T) - 1)}} \tag{11.2}$$

Comparing the two data sets:

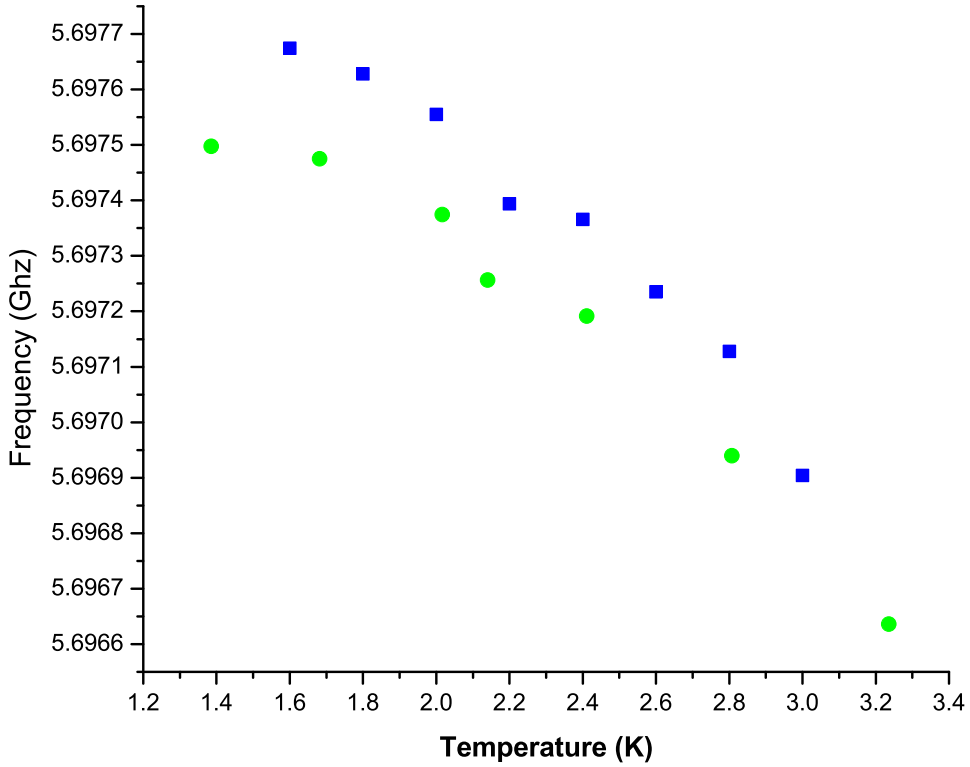


*Fig. 11.4:* The blue square data set is based on the 6 $\mu m$ gap CPR modified to include the temperature dependence of the permittivity of the liquid Helium. This is compared to the green circle 6 $\mu m$ gap CPR data that is taken from the real data set measured in cryostat 1.

There is $\approx$ 0.2 Mhz difference between the two data sets that imply a slight error, probably due to the inaccuracy in measuring the temperature of the system in cryostat 1. The calculated percentage difference in permittivity is negligible.

The ratio of the kinetic to geometric inductance for the CPR is roughly $L_k(1.57K, 0mT)/L_g = 4.32\%$. This value is consistent with other reported values of $L_k(T, 0mT)/L_g$ for CPRs with similar dimensions reported in reference [5].

The figure below is based on a Niobium on Sapphire substrate with CPR parameters; $s = 10$ $\mu$m, $w = 5$ $\mu$m, $l = 11$ mm and 4 $\mu$m coupling gaps.

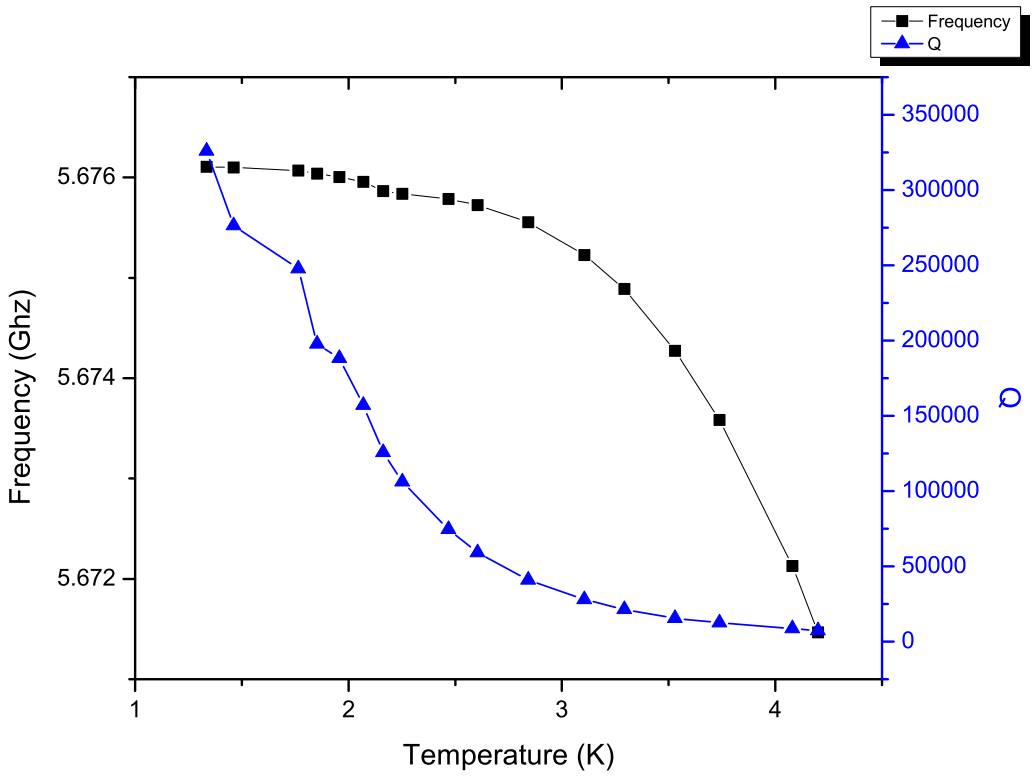


*Fig. 11.5:* Resonant frequency and $Q$ factor versus temperature for a Niobium on Sapphire Substrate with CPR parameters of $s = 10$ $\mu$m, $w = 5$ $\mu$m, $l = 11$ mm and 4 $\mu$m coupling gaps. Measured in cryostat 1.

The resonant frequency and $Q$ factor have a similar temperature dependence to that shown in figure 11.2. Below are results based on the same CPR as that above, but were measured by Tobias Lindstrom [6] in a Adiabatic Demagnetisation Fridge (ADR). The ADR is capable of much lower temperature giving a greater insight into the temperature dependence of the resonant frequency and $Q$ factor. These measurements were made as part of a collaboration between the Condensed Matter Department at The University of Birmingham and the Quantum Physics group at the National Physical Laboratory.

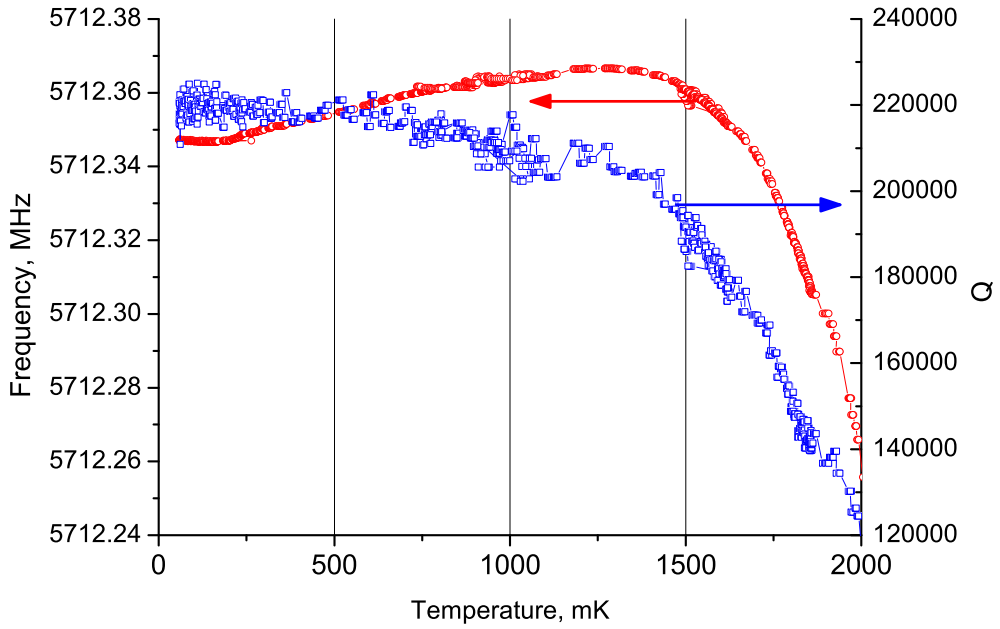


*Fig. 11.6:* Resonant frequency and quality factor $Q$ as a function of temperature for an overcoupled (4 $\mu m$ coupling gap) CPR fabricated on a $Al_2O_3$ substrate. CPR parameters; $s = 10$ $\mu$m, $w = 5$ $\mu$m, $l = 11$ mm and a 4 $\mu$m coupling gap. The rise in resonant frequency for a decrease in temperature is due to the change in the number density of Cooper pairs. The decrease in resonant frequency for $T < 1.5$ K, is an unexpected feature of CPRs, and is attributed to the resonant coupling of the CPR with TLS in the substrate. Courtesy of T. Lindstrom [6].

The first feature to note is the rise in the resonant frequency and $Q$ with decreasing temperature that is present in all four graphs above. This is consistent with London theory [33] that states for decreasing temperatures the number density of superconducting Cooper pairs increases, and this is reflected as an increase in resonant frequency and $Q$.

Present in figures 11.2 and 11.5 is a dip in frequency at 2.2 K. The significance of this temperature point is that this corresponds to the phase transition between liquid Helium and superfluid Helium, and is known as the lambda point. This phase transition is associated with the superfluid fraction affecting the electric properties, i.e. altering the dielectric constant of Helium due to the polarization connected with an elastic deformation of the electron shell at that point, that occurs on a global scale involving the ensemble of electrons within the Helium [69]. Since the effective permittivity is inversely proportional

to the frequency, then any increase in the permittivity of the liquid Helium at this phase change results in a dip in the measured resonant frequency.

The ratio below is found to be quantitatively correct.

$$\frac{f_{helium}(T = 2.2\ K)}{f_{vacuum}(T = 2.2\ K)} \propto \sqrt{\frac{\epsilon_{eff,vacuum}(T = 2.2\ K)}{\epsilon_{eff,helium}(T = 2.2\ K)}} \tag{11.3}$$

The ratio of $f_{helium}(T = 2.2\ K)/f_{vacuum}(T = 2.2\ K) = 0.9972$, taken from figures 11.2 and 11.4, and $\sqrt{\epsilon_{eff,vacuum}(T = 2.2\ K)/\epsilon_{eff,helium}(T = 2.2\ K)} = 0.9973$, where $\epsilon_{eff,vacuum}(T = 2.2\ K) = 5.3885$ and $\epsilon_{eff,helium}(T = 2.2\ K) = 5.4172$ taken from the fit above. The dip in frequency at $T = 2.2$ K measured in cryostat 1 compared with the frequency measured in cryostat 2, is comparable with the difference between the permittivity of the liquid helium ($\epsilon_{helium}(T = 2.2\ K) = 1.05748$) and the permittivity of air.

In figure 11.6 for $T < 2$ K, the general trend of the resonant frequency shows a decrease and an increase in resonant frequency. The final rise in frequency is again a consequence of the change in the kinetic inductance due to the change in the number density of Cooper pairs, however the lowering of the resonant frequency is not easily explained or fully understood.

The reduction in frequency for $T < 2.2$ K is believed to be associated with coupling the resonant mode to two level systems (TLS) in the substrate material. This behaviour is further characterised by a gradual increase in the $Q$, compared with the large increase in the $Q$ between $2.2 < T < 4.2$ K, see figure 11.6. It is generally agreed [**?**, **?**, 70] that the losses at low temperatures are limited by dissipation mechanisms (such as TLS) unrelated to superconductivity.

The evidence for TLS is the shape of the temperature dependences at $T < 2.2$ K, reminiscent of the effects of paramagnetic impurities contributing a Curie term proportional to $1/T$ to the magnetic susceptibility ($\propto \mu$) of the substrate [45], see also figure 11.9. These TLS could also arise from weak/dangling bonds within the Silicon Dioxide [71, 72]. Dangling bonds are an inherent quality of semiconductor surfaces. They act as reaction sites in chemical reactions and surface states in electronic processes. Coupling between the resonant frequency and these surface states and/or paramagnetic impurities produce the same characteristics as observed above.

For TLS to be the root cause of this dip in frequency, the TLS would have to have comparable resonant frequencies to that of the CPR. This is possible because these TLS have a wide distribution of energies and energy level spacings that could couple to the CPR resonance.

The method employed to test this hypothesis is to apply different microwave power levels to the coupled resonant modes of the CPR and the TLS, both on Sapphire and oxidized Silicon substrates. Applying a high microwave power forces the electrons in the TLS into higher energy states, saturating that state. This would make the TLS less likely to absorb energy from the resonant mode of the CPR, hence the modes would become decoupled. This would be observed in the experimental results as an increase in resonant frequency and $Q$ for a decrease in temperature.

## *11.2 Power Dependence*

The power applied to CPRs can alter their resonant features, See figure 11.7.

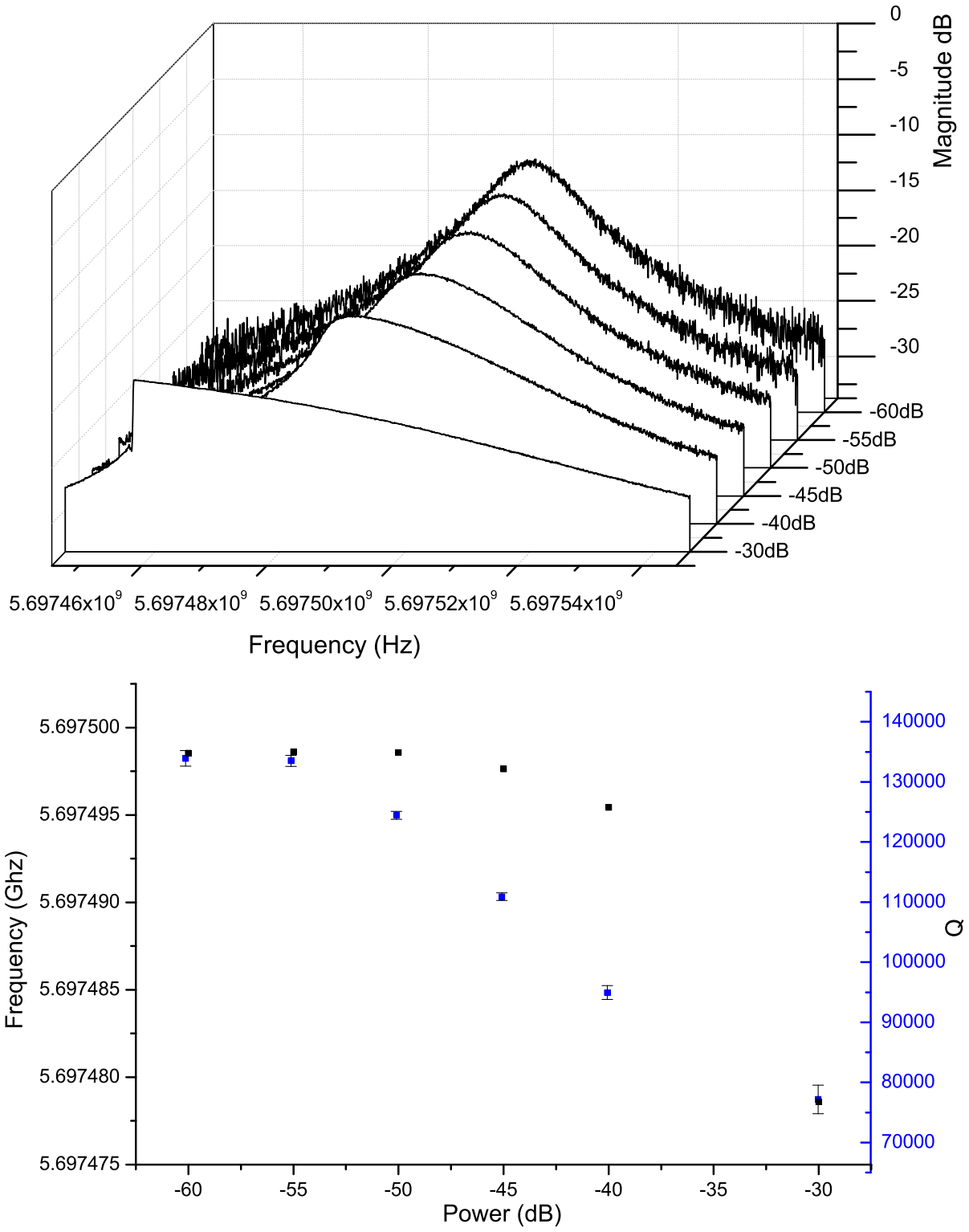


*Fig. 11.7:* **Top**; Power dependence of a $Nb/Al_2O_3$ half wavelength CPR with parameters; $l = 11$ mm, $w = 5$ $\mu m$, $s = 10$ $\mu m$, and 6 $\mu m$ coupling gap. These measurements are taken at a fixed temperature of $T = 1.3$ K and measured in cryostat 1. **Bottom**; resonant frequency (black) and Q (blue) with error bars as a function of power.

The onset of non-linearity for this device occurs between $P = -30$ dBm and $P = -45$ dBm. This non-linearity is characterised by a bending over of the resonant frequency peak to a lower frequency. This is achieved by increasing the microwave power applied to the CPR and dissipating energy in the resonator.

The major non-linear effects are driven by the current in the CPR, which changes as the $Q$ changes. The reduction in resonant frequency is associated with increasing the kinetic inductance by making the current density as large as possible by non uniform lateral current distributions. Increasing the kinetic inductance reduces the number density of superconducting Cooper pairs, which is the same process as increasing the temperature of the superconductor.

The power coupled into the resonator is dependent on the size of the coupling gap. The onset of non-linearity can therefore be altered by changing the size of this gap. All of the measurements reported in this thesis have been undertaken in the linear power regime, as this leads to repeatable measurements and high $Q$ factors.

It should be noted that not all research groups operate their CPRs in the linear regime. P. Meeson from Royal Holloway uses the non-linear characteristics coupled to QUBITs to perform quantum non-demolition experiments [73].

The power dependence of the $Q$ factor has also been measured as a function of temperature. This is not to investigate the difference between the linear and non-linear regions, but rather the ability to decouple TLS from the resonant frequency of the CPR. The graph taken from reference [70], demonstrates the effect of gradually increasing the power applied to the CPR to saturate these TLS, and increase the $Q$.

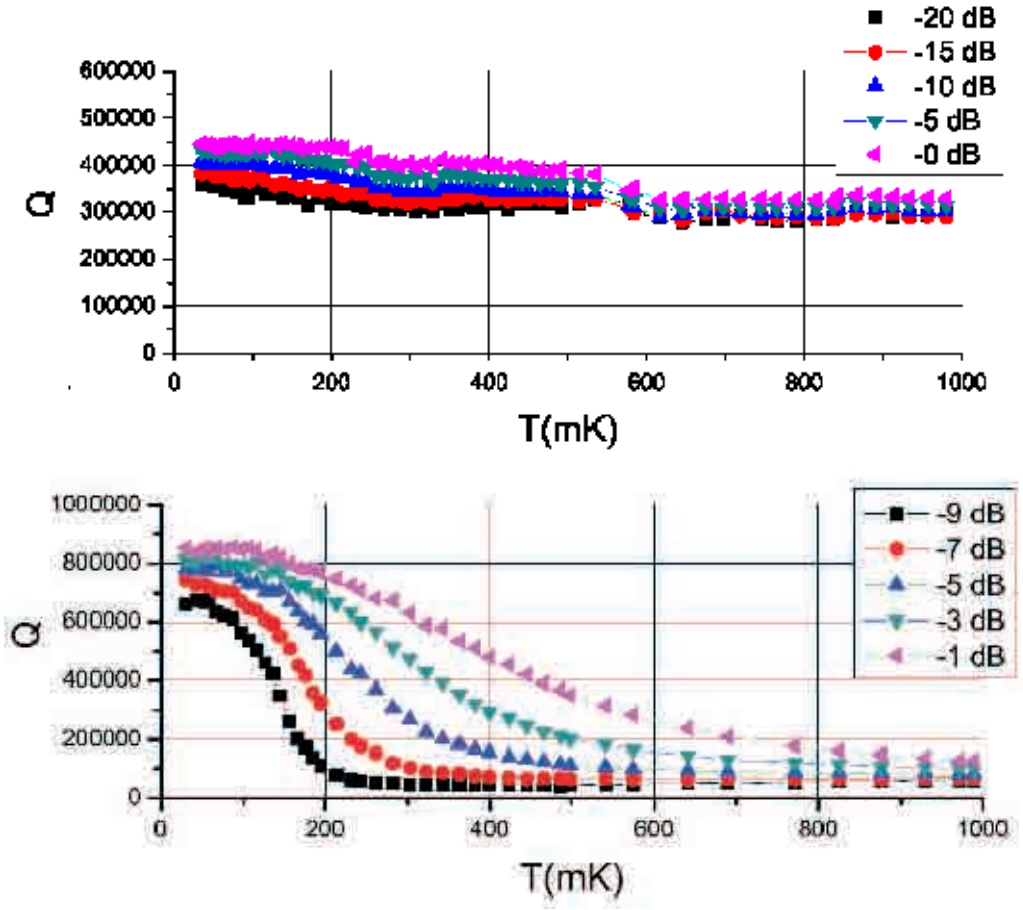


*Fig. 11.8:* **Top**; The $Q$ as a function of temperature for different powers applied to $Nb/Al_2O_3$ CPR with parameters, $l = 11$ mm, $s = 10$ $\mu$m, $w = 5$ $\mu$m, and 4 $\mu$m coupling gap. In their set-up, 0 dB corresponds to $-27$ dBm from the network analyzer and this is attenuated by 70 dB at the sample input. **Bottom**; The same structure as above, but measured on a $Nb/SiO_2/Si$ CPR. Courtesy of T. Lindstrom [70].

The change in $Q$ is larger for CPR structures on oxidized Silicon substrates, compared with Sapphire substrates. For example, an increase in power of 10 dB at $T = 200$ mK, the $Q$ changes from $100,000$ to $750,000$ for a Niobium CPR on oxidized Silicon (from $-9$ to $-1$ dB), and $390,000$ to $450,000$ for a Niobium CPR on Sapphire (from $-10$ to 0 dB). This is probably because the Silicon Dioxide [74] layer is amorphous and contains more TLS compared with Sapphire that is a single crystal [75]. The consequence therefore of increasing the applied power, is reflected in a larger increase in the $Q$ and resonant frequency. This is further demonstrated by the work undertaken by T. M. Klapwijk *et al*

[45].

T. M. Klapwijk *et al*, primarily study the temperature dependence of the resonant frequency and frequency noise of NbTiN CPRs, however they include work on resonators covered with $SiO_x$ dielectric of various thicknesses. Increasing the thickness of $SiO_x$ dielectric layer results in the resonant frequency demonstrating a larger scaling with temperature. This is indicative of increased number density of TLS distributed in the volume of the $SiO_x$ that alters the permittivity. They also find that the thickness of the $SiO_x$ dielectric does not effect the noise on the resonant frequency and the phase.

It should be noted that the change in $Q$ for different powers applied to the CPRs is not the same at all temperatures. For $kT > E$, where $k$ is Boltzmann factor, $T$ is the temperature and $E$ is the energy level separation of the TLS, every state of the TLS has a probability of being equally occupied. If a microwave photon generated by the CPR interacts with a single TLS, then the photon is absorbed and subsequently transmitted. The energy within the CPR is therefore not lost to the TLS but is re-emitted. This effect is equivalent to the strong field limit in atom-photon interactions [22] and typically occurs at $T > 2.2$ K inferred from these measurements.

For lower temperatures ($kT < E$) it is more probable that the ground state of the TLS is occupied, making it more susceptible to absorbing a photon. The TLS in its excited state, looses energy either through spontaneous emission, or through other modes such as phonons. This takes energy out of the CPR.

As stated above, for energy to be absorbed from the CPR, the frequency of the microwave photon has to be resonant with the energy levels within the TLS. Since the resonant frequency is constantly changing, then as the temperature reduces, the resonant frequency becomes resonant with different TLS within the substrate. The number density and nature of TLS that exists within the substrate varies, therefore at different temperatures, the resonant frequency becomes resonant with different TLS, and therefore the amount of energy that is taken from the CPR varies. As a consequence, when these TLS are saturated with a high microwave power, then it can be inferred that a bigger increase in $Q$ is indicative of more TLS being saturated in the substrate.

Below is a comparison between two CPR resonators with a 6 $\mu m$ coupling gap on $Nb/Al_2O_3$ and $SiO_2/Si$ substrates to compare the effect of TLS in different substrates. The frequency points for both sets of data are normalised to $T_0 = 1.19$ K, so easy comparisons can be drawn from the data.

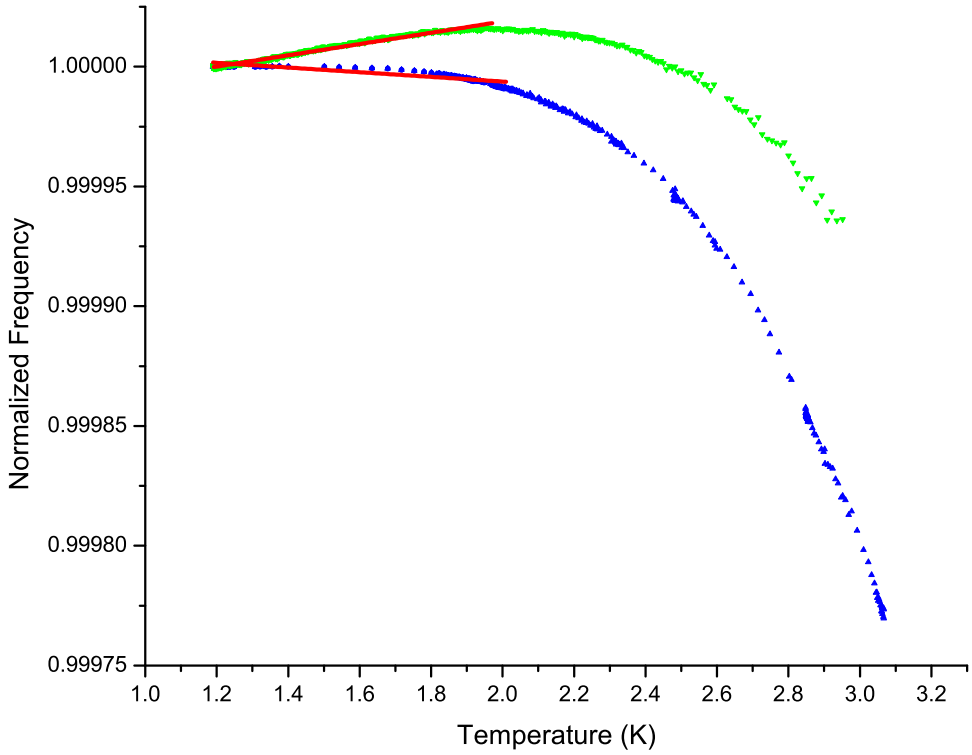


*Fig. 11.9:* Niobium CPRs on Sapphire (blue up arrows) and oxidized Silicon substrates (green down arrows), with CPR dimensions of $w = 5$ $\mu$m, $s = 10$ $\mu$m and $l = 11$ mm and a 6 $\mu$m gap, normalised frequency versus temperature. The frequency points are normalised to a reference temperature of $T_0 = 1.19$ K. Both are measured in the cryostat 2. The red lines are the logarithmic fits to the data. The fit is based on the resonant interaction of the dipole two-level systems with the electric field that results in a temperature dependent permittivity.

At temperatures between 100 mK and 2 K, the resonant coupling between the CPR and TLS, dominates over relaxation. This leads to a temperature-dependent variation of the dielectric constant $(\epsilon(T) - \epsilon(T_0)/\epsilon(T) = -(2nd^2/3\epsilon)(ln\frac{T}{T_0} - [g(T,\omega) - g(T_0,\omega)]))$ as shown in chapter 6 [49], and leading to the logarithmic function plotted in the figure above.

From the figure above it is evident that the Niobium on oxidized Silicon substrate data set suffers greatly from the coupling between the CPR resonant frequency and TLS in the substrate. These measurements are similar to those shown in reference [45].

## 11.3 CPRs with Different Sized Coupling Gaps

The $Q_L$ of CPRs is a measure of the intrinsic and extrinsic loss associated with the CPR configuration, as shown in equation 1.1. At low temperatures, the intrinsic loss decreases as the number density of quasiparticles decrease. The dominant source of extrinsic loss is due to the coupling of the external microwave circuitry with the CPR device. These losses are investigated below. Fluctuations in the $Q$ factor of some devices are due to flux jumping/moving in the Niobium film. These flux jumps cause resistive losses reflected in dramatic changes in the $Q$ factor, these losses are not observed in the measurement of the resonant frequency.

Figure 11.10 contains data from Nb/$Al_2O_3$ CPRs with fixed parameters of $w = 5$ $\mu$m, $s = 10$ $\mu$m and $l = 11$ mm, with various couplings 4, 6 and 8 $\mu$m. Figure 11.11 contains data from Nb/$SiO_2$/Si CPRs with similar fixed parameters with various couplings 4 and 6 $\mu$m.

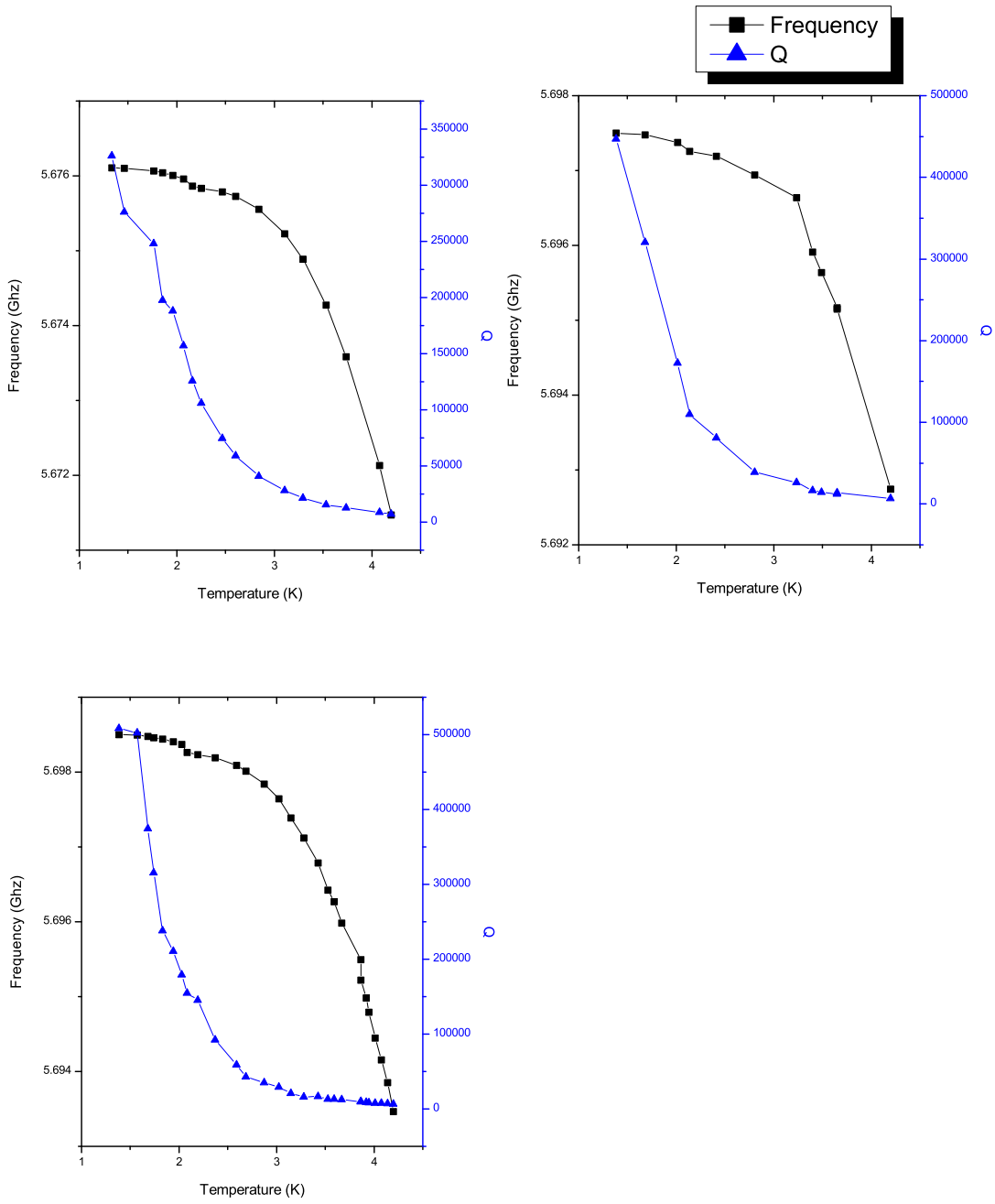


*Fig. 11.10:* Small Nb/$Al_2O_3$ resonators with $l = 11$ mm, $w = 5$ $\mu$m, $s = 10$ $\mu$m and coupling gaps 4 (top left), 6 (top right) and 8 $\mu$m (bottom left) CPRs measured in cryostat 1.

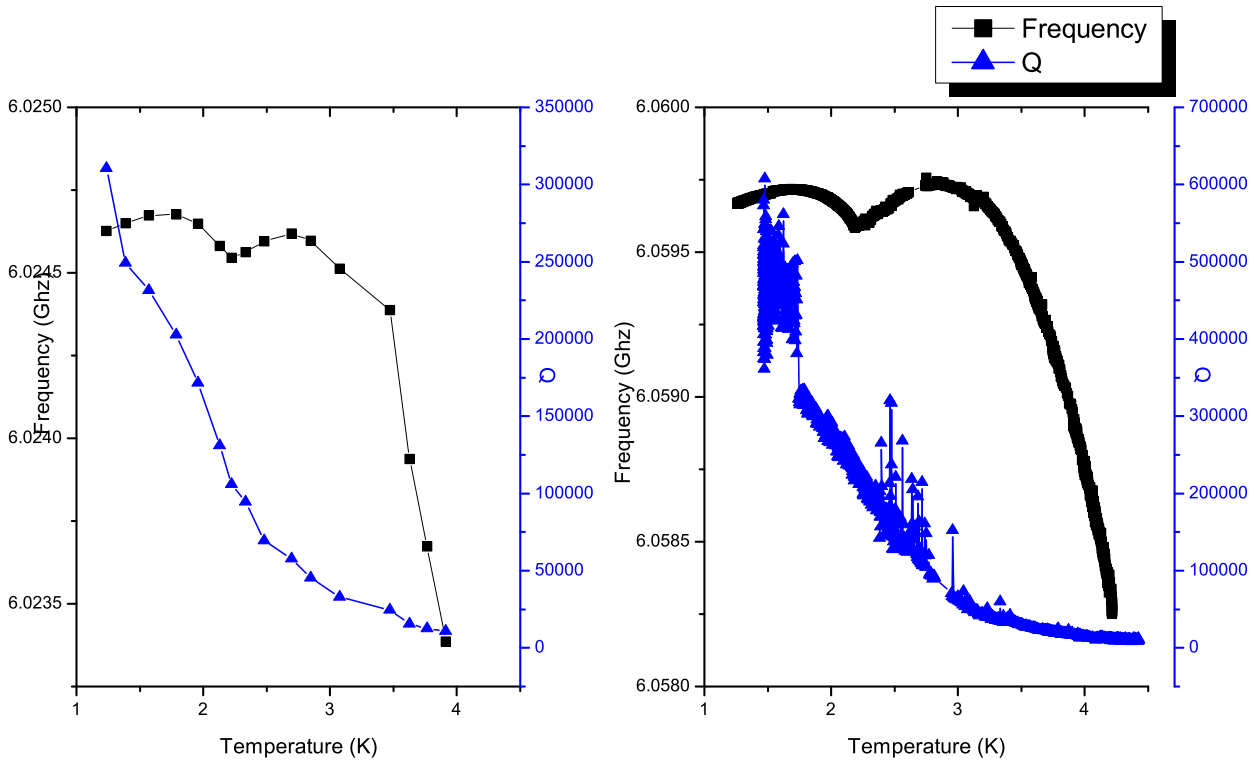


*Fig. 11.11:* Small $Nb/SiO_2/Si$ resonators with $l = 11$ mm, $w = 5$ $\mu$m, $s = 10$ $\mu$m and coupling gaps 4 (left) and 6 $\mu$m (right) CPRs measured in cryostat 1.

The resonant frequency of these devices is similar to that shown in figure 11.2. By renormalising the resonant frequency of all three graphs to a single value at a fixed temperature, all graphs display the same temperature dependence. Therefore the value of the penetration depth as shown previously is consistent for all CPRs measured. The second feature to note is that the loaded $Q$ increases with decreasing temperature, and increases with increasing gap size. As shown in section 8.3, the loaded $Q$ factor is the sum of all the losses in the system. The unloaded $Q_u$ is related to the loaded $Q_L$ by $Q_u = Q_L/(1 - S21)$ at resonance, see section 8.3.

The loaded $Q_L$ for all resonators presented in figure 11.10 are different. However by extracting the loading of the CPR in the cavity, it is found that $Q_u$ is independent of the size of the coupling as a function of temperature, see figure 11.12.

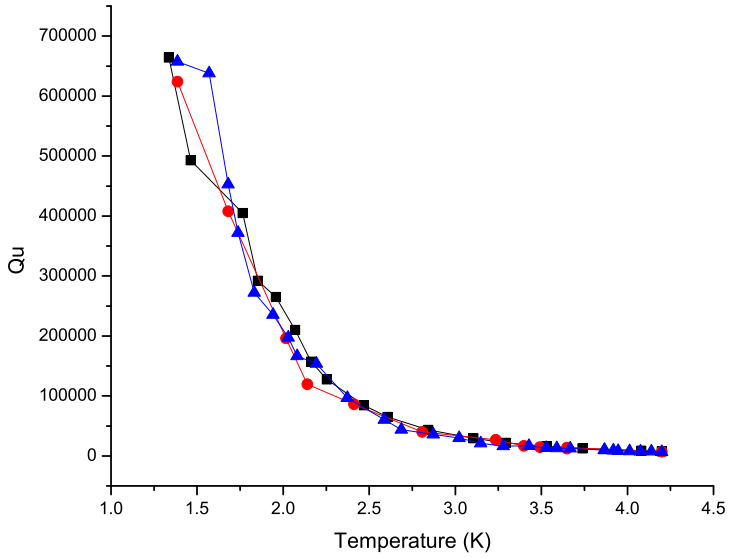


*Fig. 11.12:* Unloaded $Q$ as a function of temperature for $Nb/Al_2O_3$ CPRs with $l = 11$ mm, $w = 5$ $\mu$m, $s = 10$ $\mu$m, with a coupling gap of 4 $\mu$m (black squares), 6 $\mu$m (red circles) and 8 $\mu$m (blue triangles) measured in cryostat 1.

The increase in unloaded $Q$ as a function of temperature is therefore just a property of the change in the number density of Cooper pairs and quasiparticles within the superconducting condensate.

Resonators with strip widths $s = 30$ $\mu m$ and strip to separation width $w = 15$ $\mu$m are measured with various couplings 4, 8 and 15 $\mu$m.

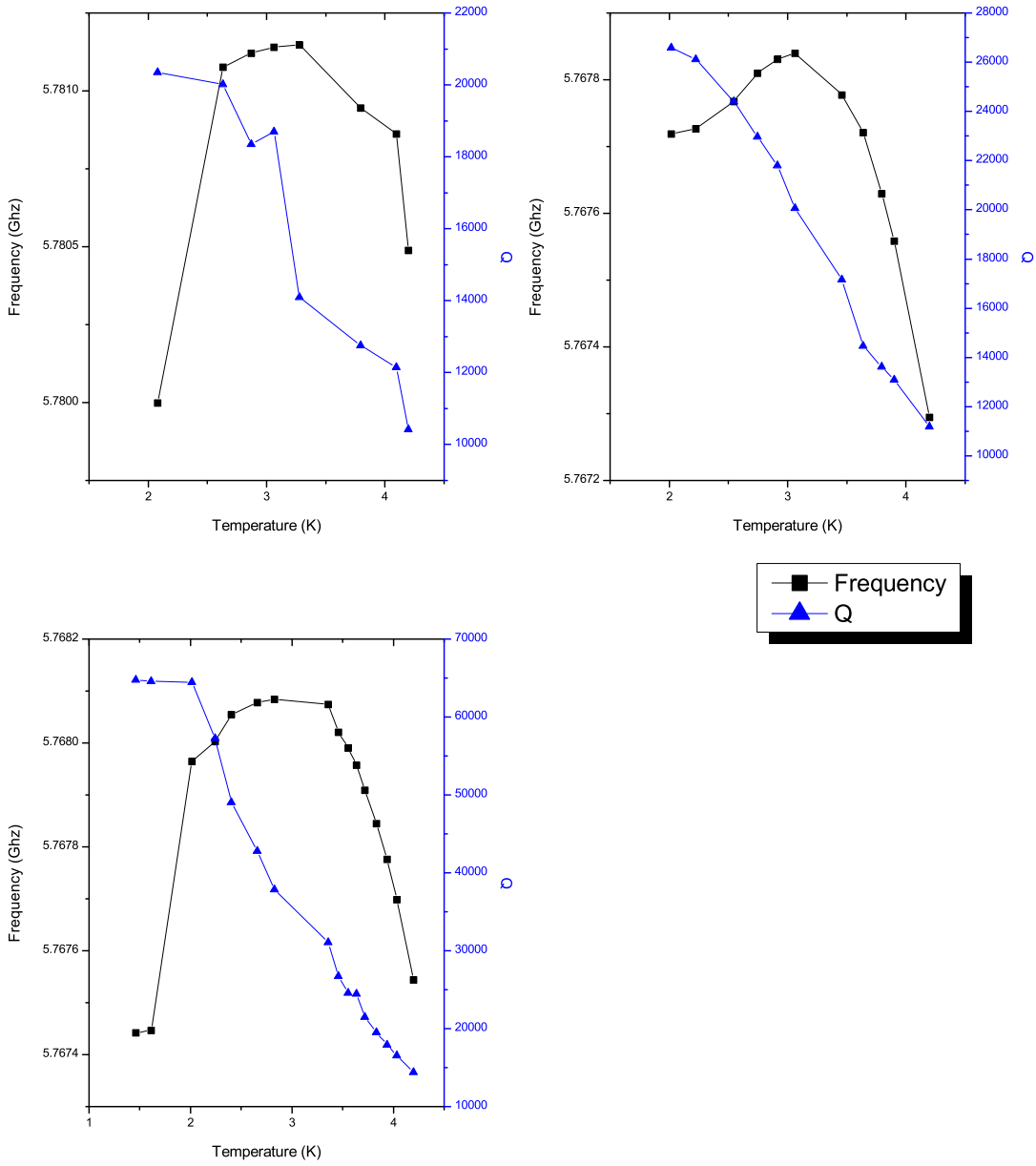


*Fig. 11.13:* The resonant frequency and $Q_L$ versus temperature for $Nb/Al_2O_3$ CPRs, with dimensions $l = 11$ mm, $s = 30$ $\mu$m, $w = 15$ $\mu$m with coupling gaps 4 (top left), 8 (top right) and 15 $\mu$m (bottom), and measured in cryostat 1

The resonant frequency for the 4 and 15 $\mu$m CPRs exhibits jumps in the resonant frequency at $T \sim 2$ K. This is probably associated with trapped flux jumping around within the film of the Niobium altering the resonant frequency.

The unloaded $Q$ of these structures are:

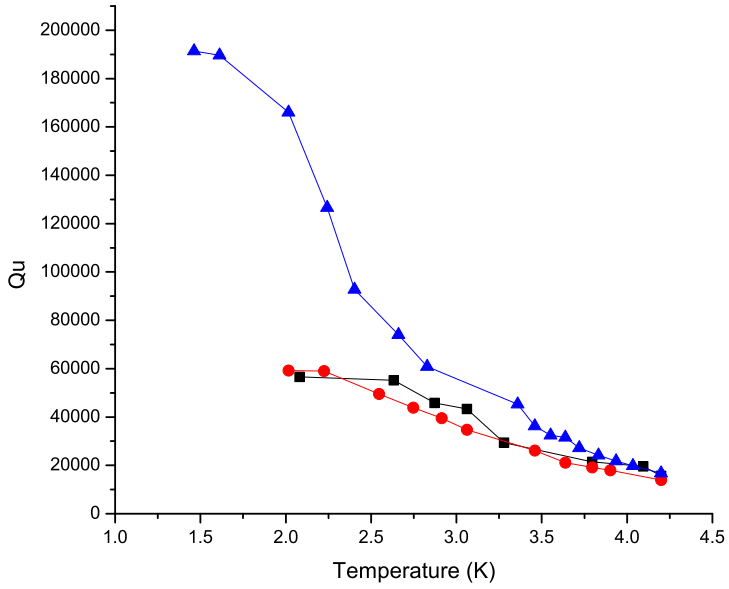


*Fig. 11.14:* Unloaded $Q$ as a function of temperature for $Nb/Al_2O_3$ CPRs, with dimensions $l = 11$ mm, $w = 30$ $\mu$m, $s = 15$ $\mu$m, with coupling gaps of 4 $\mu$m (black squares), 8 $\mu$m (red circles) and 15 $\mu$m (blue triangles) and measured in cryostat 1.

The unloaded $Q$'s in this case do not match, suggesting that other loss mechanisms are limiting the $Q$. It is not fully known why these larger resonators behave in such a perculiar fashion.

Below are two graphs containing the estimated loaded $Q$ and measured loaded $Q$ for the half wavelength CPRs displayed in figures 11.10 and 11.13. The estimated $Q$ is based on the coupling $Q$, discussed in chapter 9.

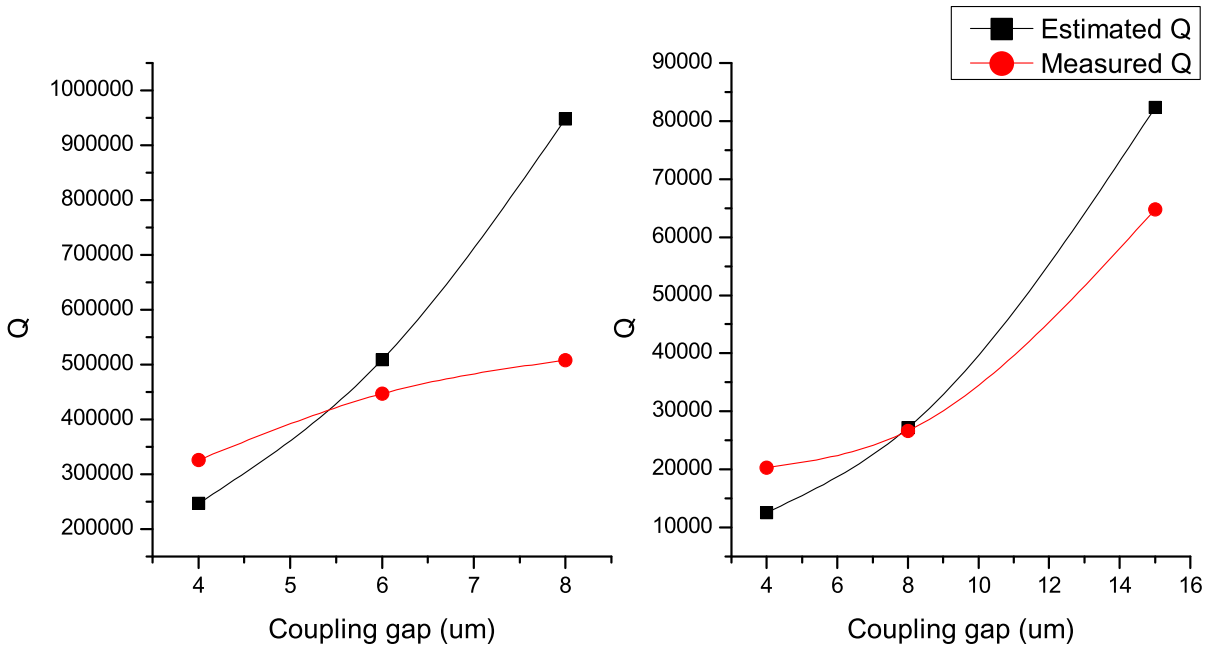


*Fig. 11.15:* Comparison between the estimated coupling $Q$ (taken from section 9) and the measured coupling $Q$ for small (left) and large (right) Niobium on Sapphire CPRs. The measured $Q$ data points are taken at $T = 1.5$ K.

For both the small ($s = 10$ $\mu$m, $w = 5$ $\mu$m) and large ($s = 30$ $\mu$m, $w = 15$ $\mu$m) CPRs the general trend of the graph is that $Q$ increases with increasing coupling gap size. The measured $Q$ should theoretically lie below the estimated $Q$ because measurements contain additional losses. These additional losses are the reason why the experimental and measured points do not exactly match.

## 11.4 Summary of Results

| Fig # | Cryostat # | Structure | $l$ mm | $w$ $\mu m$ | $s$ $\mu m$ | $C_c$ $\mu m$ | Predicted $f_0$ Ghz | $f_0(T = 1.5\ K)$ Ghz | $Q(T = 1.5\ K)$ |
|---|---|---|---|---|---|---|---|---|---|
| Fig 11.1 | 1 | $Nb/SiO_2/Si$ | 11 | 5 | 10 | 6 | 5.6721 | 6.0597 | 450000 |
| Fig 11.2 | 1 | $Nb/Al_2O_3$ | 11 | 5 | 10 | 6 | 5.6971 | 5.6975 | 320480 |
| Fig 11.3 | 2 | $Nb/Al_2O_3$ | 11 | 5 | 10 | 6 | 5.7095 | 5.7135 | 343196 |
| Fig 11.5 | 1 | $Nb/Al_2O_3$ | 11 | 5 | 10 | 4 | 5.6971 | 5.6760 | 276320 |
| Fig 11.6 | 2 | $Nb/Al_2O_3$ | 11 | 5 | 10 | 4 | 5.7095 | 5.7127 | 198000 |
| Fig 11.10 | 1 | $Nb/Al_2O_3$ | 11 | 5 | 10 | 8 | 5.6971 | 5.6984 | 502340 |
| Fig 11.11 | 1 | $Nb/SiO_2/Si$ | 11 | 5 | 10 | 4 | 5.6721 | 6.0246 | 270000 |
| Fig 11.11 | 1 | $Nb/SiO_2/Si$ | 11 | 5 | 10 | 6 | 5.6721 | 6.0597 | 450000 |
| Fig 11.13 | 1 | $Nb/Al_2O_3$ | 11 | 15 | 30 | 4 | 5.6992 | ($T = 2$ K) 5.7780 | ($T = 2$ K) 20347 |
| Fig 11.13 | 1 | $Nb/Al_2O_3$ | 11 | 15 | 30 | 8 | 5.6992 | ($T = 2$ K) 5.7677 | ($T = 2$ K) 26588 |
| Fig 11.13 | 1 | $Nb/Al_2O_3$ | 11 | 15 | 30 | 15 | 5.6992 | 5.7674 | 64754 |

*Tab. 11.1:* Table contains the CPR number and figure that it is taken from, the CPR parameters (length $l$, separation $w$, strip $s$, and coupling gap $C_c$), the predicted resonant frequency, the measured resonant frequency and $Q$ at $T = 1.5$ K unless otherwise stated.

# 12. MAGNETIC MEASUREMENTS

The tunability of the CPR is investigated by an external magnetic field applied by a Helmholtz coils, and an internal field applied through an inbuilt current control line on chip. The resonant frequency properties and tunability of SFS CPRs are also investigated, to determine whether these CPRs produce characteristic similar to normal CPRs. If they produce similar results, then this could be the initial work that could encourage other investigators to use these SFS CPRs coupled with SFS QUBITs, potentially making quantum experiments more feasible.

## *12.1 Externally Applied Magnetic Field*

An external magnetic field is applied by a Helmholtz coil to CPRs and the resonant frequency and $Q$ are measured, see configuration shown in section 10.5 and figure 12.1. The sample measured is a 4 $\mu$m gap Niobium CPR on a Sapphire substrate with dimensions $w = 5$ $\mu$m, $s = 10$ $\mu$m and $l = 11$ mm.

What is shown in the figure below is the shift in the resonant frequency ($\Delta f = f_0(H) - f_0(H = 0\ mT)$) as a function of magnetic field applied perpendicular to the CPR, and for a fixed temperature of $T = 1.38$ K. The inset figure contains data on the shift in the resonant frequency as a function of a fixed field rotated around the circumference of the CPR. The fixed magnetic field is 0.2 mT, and $\phi = 0^0$ is the field applied perpendicularly to the surface of the sample [76].

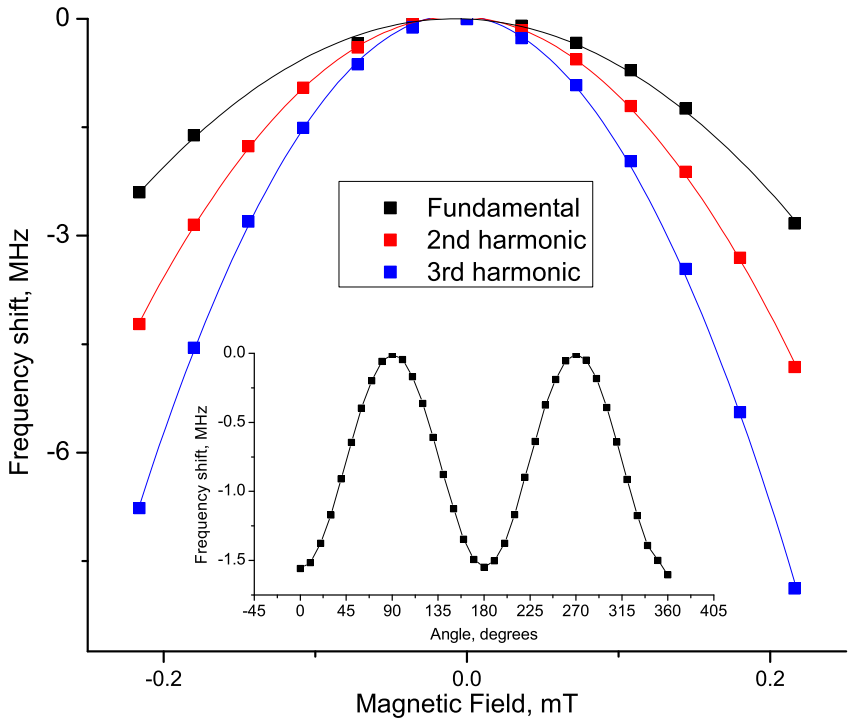


*Fig. 12.1:* A change in the resonant frequency with a perpendicular magnetic field ($\phi = 0^0$) measured for the fundamental, second and third harmonic. The inset shows the dependency of the fundamental frequency shift on the angle $\phi$ at 0.2 mT. The Helmholtz coils are rotated around the circumference of the CPR by using a lazy Susan. These measurements are taken in cryostat 1, on a Niobium on Sapphire substrate CPR with parameters $l = 11$ mm, $w = 5$ $\mu$m, $s = 10$ $\mu$m and 4 $\mu$m gap.

The results are highly reproducible as shown from the figure below. These results are based on a CPR with the same dimensions as above, but are based on a Niobium on oxidized Silicon substrate sample. The results below are courtesy of Tobias Lindstrom.

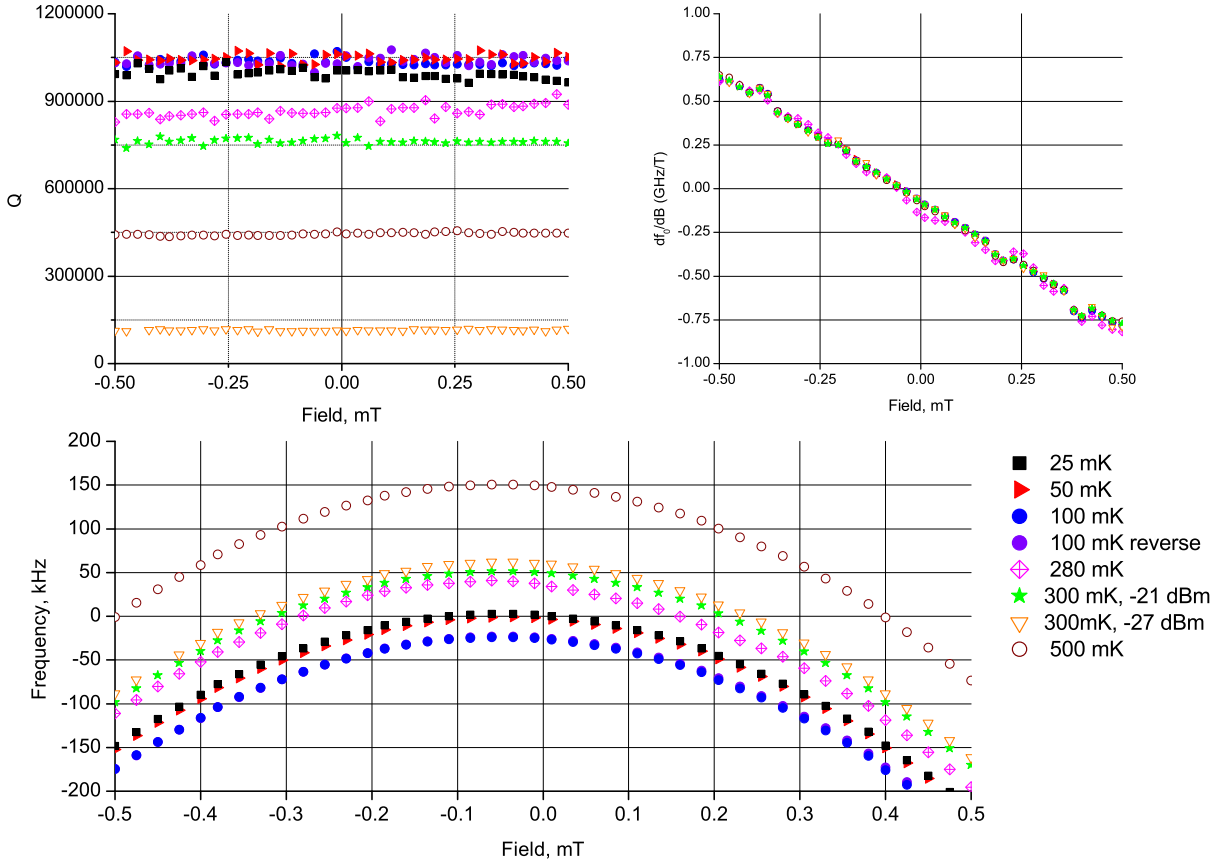


*Fig. 12.2:* Measurements undertaken by Tobias Lindstrom, on a 4 $\mu m$ gap Nb CPR on $SiO_2$/Si for a magnetic field applied at $\phi = 80^0$ from the normal of the CPR. The top left graph demonstrates that the $Q$ does not change under the application of a magnetic field, but it does as a function of temperature. The bottom graph is similar to figure 12.1. The top right is the derivative of the values obtained on the bottom graph, this demonstrates that the behaviour of the resonant frequency to an applied field is quadratic.

The first point to note is that the angle at which the magnetic field applied to the CPR is $\phi = 80^0$ and hence the shift in the resonant frequency is not at maximum. The second point to note is that the perturbation of the resonant frequency is only dependent on the geometry and not on the superconductor or substrate, therefore it is possible to directly relate figure 12.1 with 12.2.

To compare these results, the perpendicular component of the magnetic field measured by Tobias Lindstrom and the shift in the resonant frequency at this point is recorded. So

for $B_{T.L} = 0.4$ mT, the shift in the resonant frequency is $\Delta f = -120$ to $-175$ kHz. Taking the perpendicular component of the magnetic field gives, $B_y = B_{T.L} \cos\phi = 0.0044$ mT. Using this value of $B_y = 0.0044$ mT, and extracting the resonant frequency shift as measured in figure 12.1, then the shift in frequency is $\approx 72$ kHz. These results are not quite equivalent, but it should be noted that there is some trapped magnetic field in the Niobium film shown in the data in figure 12.2, and evidenced by the fact that for zero magnetic field applied, the resonant frequency is not at maximum.

The parabolic nature of the response of the frequency to an applied magnetic field is due to the magnetic field dependence of the order parameter and hence the penetration depth, as shown in section 4.5.

The order parameter is given by $\Delta \propto (H/H_c)^2$. Hence the frequency is modified to:

$$f(T,H) = f(T,0)\left(1 - \frac{L_k(T,0)}{L_T}\beta(T)\frac{H^2}{H_c^2}\right) \tag{12.1}$$

where $L_k(T,0)$ is the zero-field kinetic inductance, $L_T$ is the total inductance, $\beta(T)$ is a scaling factor, $\beta(T)H^2$ is small compared with $H_c^2$, and $L_k(T,0)$ is small compared with $L_T$. From figure 12.2, the derivative of the frequency is plotted as a function of magnetic field. Since the derivative is linear, then the integral is quadratic.

The field at which the frequency response deviates away from the parabolic behaviour and when the $Q$ diminishes is identified as the lower critical field for superconducting Niobium ($B_{c1} \approx 0.1$ T [31]). This occurs when the field applied externally is 0.25 mT (taken from figure 12.1), hence the flux focusing factor for this geometry is $\approx 400$ ($0.1\ T/0.25\ mT$).

An estimate of the flux focusing for such a device can be based on a simple ellipsoid. The field at the edges of the ellipsoid is described by $H_{edge} \propto H_{app}d/t$, where $d$ is the diameter of the ellipsoid and $t$ is the thickness. The diameter of the ground plane is $\approx 3$ mm, the diameter of the inner conductor strip is 10 $\mu$m and the thickness of the Niobium is 250 nm. The flux focusing ($d/t$) is therefore calculated between $50 - 15000$, and the flux focusing factor that is measured is 400, therefore the measured value fits within the range of the calculated flux focusing factor.

As the angle is rotated around the equator of the sample, the amount of flux focusing in the gap diminishes, hence the change in the resonant frequency decreases, see figure 12.1 and 12.2. In fact, when the magnetic field is applied at $\phi = 90^0$ to the sample (parallel), no field is focused in the gap, hence the change in the frequency is at a minimum and equivalent to the zero field situation. The change in the resonant frequency is a periodic function of angle applied to its surface.

The higher harmonics are also subjected to changes in the resonant frequency by an applied magnetic field. The higher harmonics change in the ratio of $f_3 : f_2 : f_1 = 2.8 : 1.8 : 1$. This is different to the $3 : 2 : 1$ ratio expected by this model, but it should be noted that the flux focusing is slightly non-uniform near the ends of the CPR, and that the different resonant modes are sensitive to different parts of the sample. The shift in resonant frequency for the higher harmonics is significantly higher than the shift in resonant frequency for the fundamental mode. It would be ideal to use these higher harmonics to couple to QUBITs because of their larger tuning frequency and also, two level systems (TLS) are more ineffective as their energy level spacings are not comparable to the CPR higher harmonics. However, in practise it is not possible to fabricate QUBITs with these energy levels either, therefore coupling between the CPR and QUBIT would be impossible.

The $Q$ for these measurements remains constant for fields $<< B_{c1}$. This is because the $Q$ is weakly dependent on the number density of superconducting electrons within the condensate at temperatures significantly less than the transition temperature.

Figure 12.2 above shows evidence of TLS. The data contains two measurements taken at a fixed temperature of 300 mK with two different power levels of $-21$ and $-27$ dB. Similar to the data shown in figure 11.9, the resonant frequency and $Q$ differs in an unexpected way. What is found is that for the lower power level applied to the CPR, the Q has degraded and this is attributed to energy drawn from the CPR mode, due to the resonant coupling between the CPR and TLS. Applying a slightly higher power causes these TLS to be saturated, decoupling these TLS from the CPR resonance resulting in a higher $Q$.

Below is the data obtained from a quarter wavelength resonator that was fabricated by the author, and measured in cryostat 1 at a fixed temperature of $T = 1.4$ K. The coupling parameters are $l_1 = 250$ $\mu$m long and $g = 30$ $\mu$m, see figure 12.3.

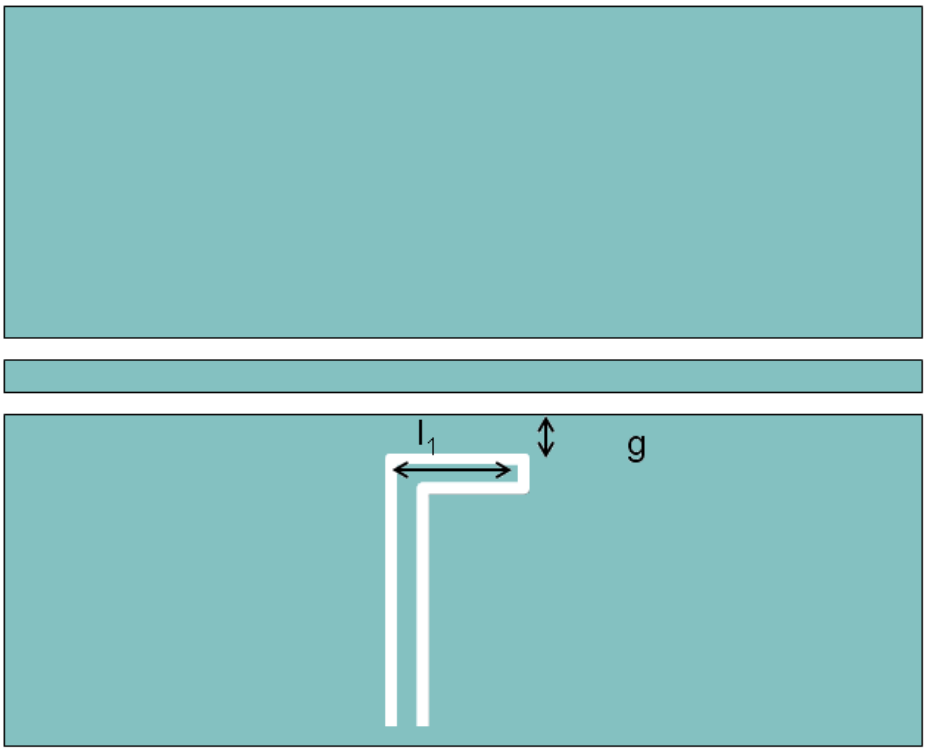


*Fig. 12.3:* A quarter wavelength CPR coupled to the feedline.

The low $Q$ measured for the quarter wavelength resonator suggests that the resonator is over coupled to the feedline.

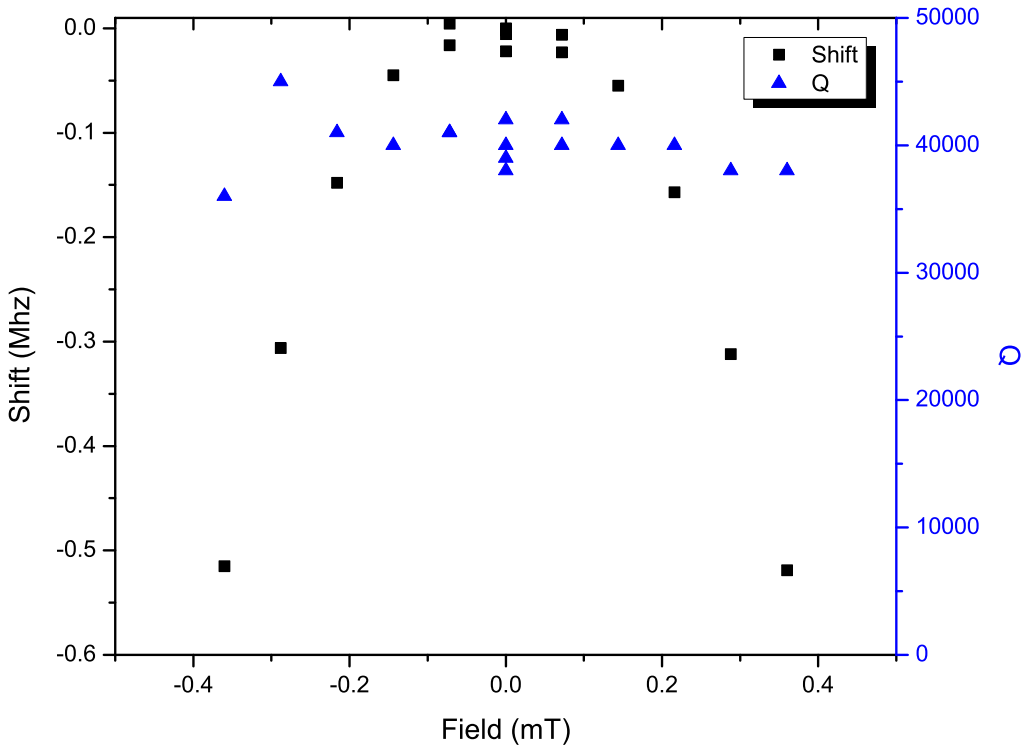


*Fig. 12.4:* Shift in the resonant frequency and $Q$ as a function of the magnetic field applied perpendicular to the surface of the quarter wavelength ($\lambda/4$) CPR. The $\lambda/4$ CPR coupling parameters are $l_1 = 250$ $\mu$m long and $g = 30$ $\mu$m separation, Nb/$SiO_2$/Si fabricated by the author, and measured in cryostat 1 at a fixed temperature of $T = 1.4$ K. The resonant frequency for this device is $f(T = 1.4\ K, B = 0\ mT) = 4.3379$ Ghz.

A shift of 0.5 Mhz is observed and corresponds to about $\approx 5$ linewidths. This is slightly less than the shift measured with the Niobium on Sapphire CPRs shown in figure 12.1. There are two possible reason for this; the samples fabricated on Sapphire and oxidized Silicon are patterned slightly different or it could be associated with the length of the two resonators.

The Niobium on Sapphire samples, under the Atomic Force Microscope (AFM) exhibits redeposited particulates in the gap of the CPR and at the edges. This could result in varying amounts of flux focusing in the gap. This could alter the penetration depth and hence the shift in the resonant frequency. Conversely, the oxidized Silicon samples underwent rigorous etching and cleaning processes. If the Niobium had been over etched, this would produce a lower flux focusing factor compared with the Sapphire samples, and

this would be reflected in a lower shift in the resonant frequency for the same field applied to the CPRs.

The second reason could be associated with the length of the two resonators. A half wavelength CPR has a magnetic field pattern shown in figure 1.2, i.e. the magnetic field peaks in the centre of the CPR. For a quarter wavelength CPR the magnetic field pattern is half of that shown in the figure. Therefore the shift in the resonant frequency for a half wavelength CPR should be half that of a quarter wavelength CPR. This is shown to be correct.

In conclusions the maximum change in resonant frequency is shown in the data in figure 12.1 and for this device is $\approx 5$ Mhz. This corresponds to about 200 linewidths. The high $Q$ factor is also maintained and therefore the perturbation of the resonant frequency is therefore repeatable. This method is useful for changing the resonant frequency by a large amount and would be suitable to be employed in CPR/QUBIT experiments. However it would be more beneficial if this could be achieved by on chip patterning of the Niobium wafer and this is addressed in the following section.

## *12.2 Internally Applied Magnetic Field*

The specimen used here is based on the design shown in figure 10.9. It is a half wavelength Niobium on oxidized Silicon CPR with a current control line $\approx 1\%$ the length of the line situated near to the resonator centre. An external field of 0.122 mT is applied by the Helmholtz coil to provide a non-zero resonant frequency offset $df_0/dB$, to provide sensitivity to the current applied by the control line, see figure 12.5. The following results were obtained.

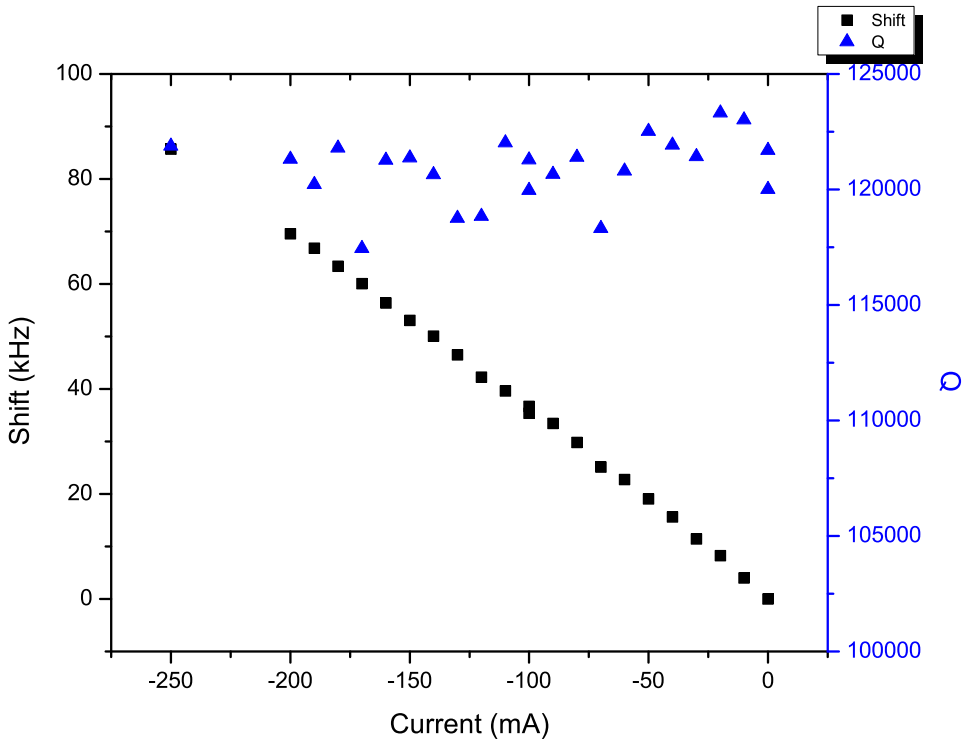


*Fig. 12.5:* The shift in the resonant frequency as a function of the current applied to the control line for a Nb/$SiO_2$Si CPR with dimensions, $l = 13.7$ mm, $s = 10$ $\mu$m, $w = 5$ $\mu$m and coupling gap 4 $\mu m$. This sample was measured in cryostat 1 at a fixed temperature of 1.28 K. The zero magnetic field resonant frequency is 4.54 GHz

It should be noted that the current is applied to generate a field opposite to that applied by the external Helmholtz coil. Therefore an increase in the current applied to the control line results in an overall decrease in the total field, and hence an increase in the resonant frequency.

The shift in the frequency is approximately 3 linewidths. This is small compared with the shift observed by applying the magnetic field externally. It should be noted that the $Q$ in this case is not particularly high, hence the bandwidth is broad, and this limits the number of linewidths by which the resonance moves. The measured $Q$ remains constant with the current applied to the current control line.

There are two possibilities for the small shift in the resonant frequency. The first possibility may be associated with the fact that the current control line is only a small percentage of the total length of the CPR line, hence the field coupled into the CPR is

small and limited to the centre. This can be rectified by producing CPRs with current control lines that extend the whole length of the conductor strip. Secondly, the low $Q$ may be associated with coupling the CPR to the "lossy" 50 Ω current control line, as this can effectively dampen the system.

## 12.3 Magnetic Field Tuning of SFS CPRs

CPRs are fabricated from Niobium (thickness 300 nm)/Cobalt (thickness 3 nm)/Niobium (thickness 300 nm)/Titanium (thickness 2 nm) thin films on Sapphire and oxidized Silicon substrates. As mentioned in section 3.1 Nb/Co/Nb is used as the basis of the Josephson Junction that forms part of the RF QUBIT. The Titanium is deposited on the Sapphire to act as an adhesive to encourage Niobium to grow on top of the titanium film. This film is nanometres in thickness and does not contribute any property to the CPR or the RF QUBIT characteristics, as shown below. Both layers of Niobium are 300 nm thick and the Cobalt layer is 2.21 nm.

CPRs are measured in the absence of RF QUBITs, and this is to deduce whether the Cobalt interacts with the resonant characteristics of the CPR. Measurements are also made on a CPR with a superconducting thin film square in the centre of the gap of the resonator representing the RF QUBIT.

### 12.3.1 CPR in the Absence of the RF QUBIT.

The CPR measured here has dimensions of $l = 11$ mm, $s = 30$ $\mu$m, $w = 15$ $\mu$m and 20 $\mu$m coupling gaps. These thin films are deposited by Jason Robinson from the Material Science group at Cambridge University, and patterned by the author.

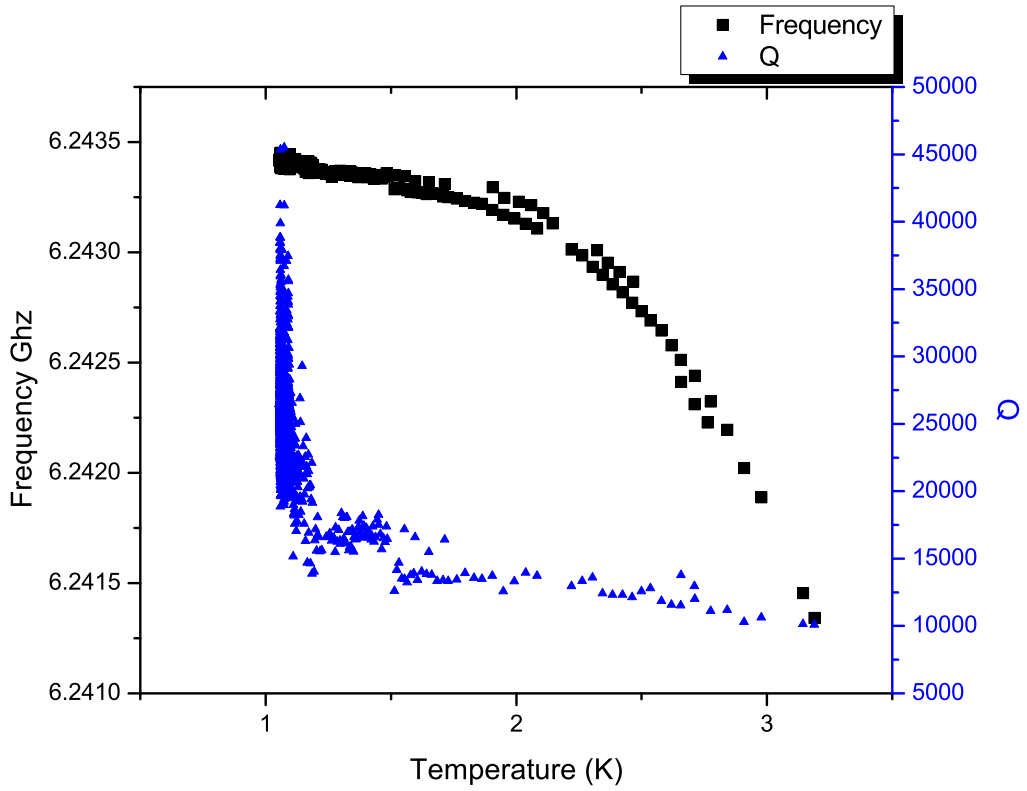


*Fig. 12.6:* The resonant frequency and $Q$ as a function of temperature for a Nb/Co/Nb/Ti/$Al_2O_3$ CPR with dimensions $l = 11$ mm, $s = 30$ $\mu$m, $w = 15$ $\mu$m and 20 $\mu$m coupling gaps, and measured in cryostat 2.

The scatter on the $Q$ can be attributed to flux jumps in the film, the scatter on the resonant frequency is not understood. A magnetic field is subsequently applied by the Helmholtz coils.

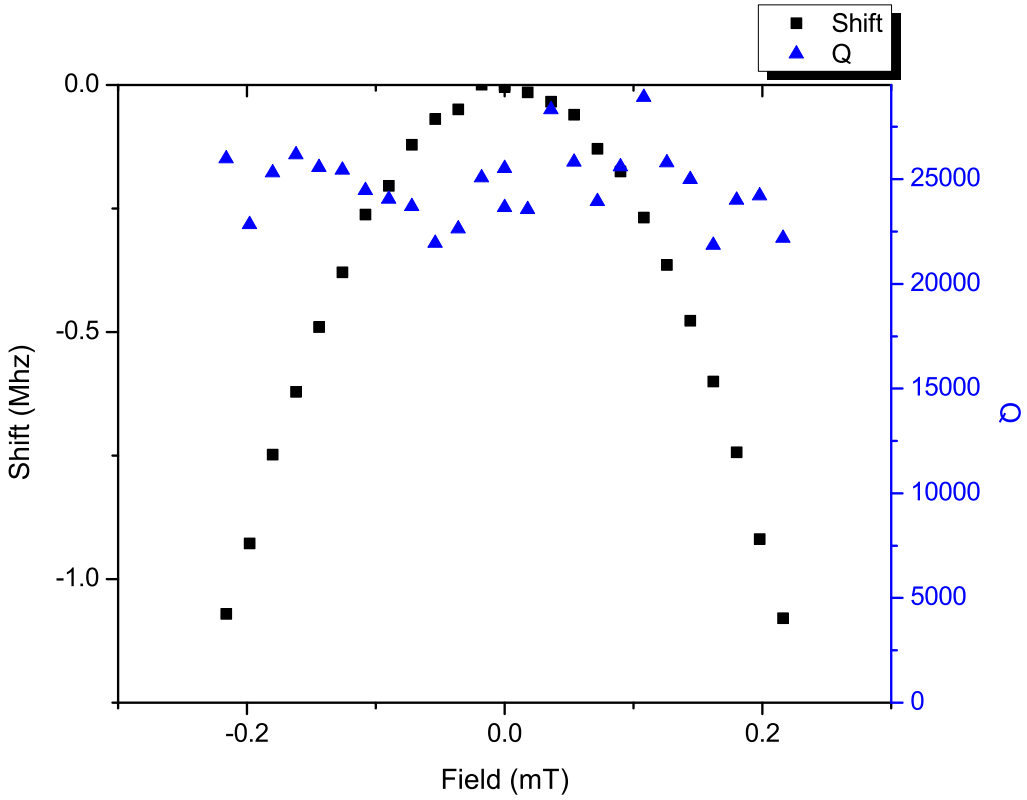


*Fig. 12.7:* The shift in the resonant frequency and $Q$ as a function of the magnetic field applied perpendicular to the surface of the CPR. This resonator is based on the structure; Nb/Co/Nb/Ti/$Al_2O_3$ with dimensions of $l = 11$ mm, $s = 30$ $\mu$m, $w = 15$ $\mu$m and 20 $\mu$m coupling gaps, and measured in cryostat 2.

For a field of 0.216 mT the shift in the resonant frequency is $\Delta f = -1.079$ MHz and corresponds to 4 linewidths. The $Q$ for this sample is low. This could be due to the coupling to the external microwave circuitry, a problem with the deposition of the Niobium film, or the interaction between the CPR resonance and TLS in the Cobalt layer [14].

The coupling gap is larger than the values previously measured for Niobium on Sapphire CPRs, see section 11.3. Since the coupling gap is larger than those previously measured in figure 11.13, then the coupling capacitance is lower and the $Q$ should be higher. Previous measurements have produced $Q \sim 60,000$ for the same dimensions, therefore the low $Q$ measured here is probably not associated with the coupling.

The magnetic field applied to the surface does not exceed the coercive field of the

Cobalt ($1-90$ mT) [77]. The parabolic curve of the resonance with the applied magnetic field is therefore associated with the flux focusing of the field in the gap and not associated with any interaction with the magnetic Cobalt layer. It is assumed therefore that the Cobalt does not interact with the CPR resonant characteristics.

The loss is therefore assumed to be associated with the poor quality of the Niobium film. Previous measurements on other Niobium films have produced low $T_c$ films, with broad transition temperatures. Further research into producing higher quality films should be therefore be undertaken.

### *12.3.2 CPR with a square in the Gap.*

In this experiment, a square of superconducting material is deposited and patterened in the middle of the CPR in the gap between the conducting strip and the outer ground planes. This square represents the position where the QUBIT will be situated, and is used to test whether the resonant frequency is unperturbed by its presence. The square has dimensions of $10 \times 4$ $\mu$m$^2$. Numerous samples have been tested, and no resonance has been observed. The lack of observable resonant frequency is not believed to be associated with the presence of the square, but rather due to poor deposition of the top layer of Niobium that is probably non-superconducting.

## *12.4 Summary of Results*

| Fig | Composition | $l$ mm | $w$ $\mu m$ | $s$ $\mu m$ | $C_c$ $\mu m$ | $f_0(T = 1.5\ K)$ Ghz | $Q(T = 1.5\ K)$ | $\Delta f$ Mhz |
|---|---|---|---|---|---|---|---|---|
| Fig 12.1 | $\lambda/2$ Nb/$Al_2O_3$ | 11 | 5 | 10 | 4 | 5.6756 | 179900 | -2.82 |
| Fig 12.4 | $\lambda/4$ Nb/$SiO_2$/Si | 6.85 | 5 | 10 | $l = 250$ $g = 30$ | 4.3380 | 38560 | -0.15 |
| Fig 12.5 | $\lambda/2$ Nb/$SiO_2$/Si | 13.7 | 5 | 10 | 4 | 4.496 | 12000 | 0.085 ($T = 1.28$ K, 200 mA) |
| Fig 12.7 | Nb/Co/Nb/Ti/$Al_2O_3$ | 11 | 15 | 30 | 20 | 6.24325 | 43000 | -1 |

*Tab. 12.1:* Table contains the figure that the data is taken from, the CPR parameters (length $l$, width $s$, strip separation $w$, and coupling gap $C_c$), the resonant frequency and $Q$ at $T = 1.5$ K, and the shift in the resonant frequency at $T = 1.4$ K ($\Delta f = f_0(1.4\ K, 0.2\ mT) - f_0(1.4\ K, 0\ mT)$) unless otherwise stated.

# 13. CONCLUSIONS

## *13.1 Niobium on Sapphire and Oxidized Silicon Resonator Measurements*

Niobium CPRs on oxidized Silicon and Sapphire substrate device material are investigated in section 11.1. The resonant frequency and $Q$ is shown to increase as a function of decreasing temperature. It is reasonable to assume from London theory [33] a relationship between this increase, and an increase in the number density of Cooper pairs. Measured Niobium CPRs on both types of substrate is shown to produce high $Q$ factors ($Q(T = 1\ K) \sim 500,000$) (figure 11.5 for $Nb/Al_2O_3$ CPR and figure 11.11 for $Nb/SiO_2/Si$). Loss is minimized by the low loss tangent of both substrates at low temperatures [57, 58, 59] (see section 9, figure 9.5).

The $Q$ measured at temperatures $< 3$ K of a CPR on oxidized Silicon substrate (see figure 11.11) is lower compared with that of a CPR on Sapphire substrate (see figure 11.5). This loss is not associated with the differences in loss tangent, which is negligible. It is attributed to the resonant coupling between the CPR resonant frequency and two level systems (TLS) within the substrate layer [70]. Coupling between the CPR resonant frequency and TLS in the substrate layer absorbs energy from the CPR transmission signal, and results in a decrease in the $Q$ and the resonant frequency of the CPR.

It is generally shown that an increase in the microwave power applied to a CPR results in a higher $Q$ factor and resonant frequency. This is evidence of the decoupling of the resonant frequency from TLS. Further evidence of TLS interaction is the logarithmic dependence of CPR resonant frequency with temperature $< 2$ K (see figure 11.9). The theoretical interaction of a dipole TLS with an electric field is also a logarithmic function,

and results in a temperature dependent permittivity [45].

These TLS are present in both types of substrate (see section 11.2). Oxidized Silicon compared with Sapphire substrate devices show a larger increase in resonant frequency and $Q$ with increase in applied microwave power, for a measured temperature range of 150 to 1000 mK (see figure 11.8 top and bottom). This is most likely due to an increased number density of TLS within the oxidized Silicon, as also inferred from measurements of frequency versus temperature (section 11.2). For example, for an increase in power of 10 dB at $T = 200$ mK, the $Q$ changes from $100,000$ to $750,000$ for a Niobium CPR on oxidized Silicon (from $-9$ to $-1$ dB), and $390,000$ to $450,000$ for a Niobium CPR on Sapphire (from $-10$ to 0 dB).

Changes in resonant frequency and $Q$ with temperature and power for Niobium CPRs on both substrate devices with changes in CPR device geometry are also measured (see section 11.3). Different conductor strip to strip separation widths (compare figure 11.10 with 11.13) and varying coupling capacitor dimensions are investigated (see figure 11.10 and 11.11). It is found that decreasing the conductor strip to separation width, for constant width ratio, produces devices with higher $Q$ factors. Increased losses with increase in conductor strip width are attributed to radiation loss and flux noise within the superconductor.

The coupling of CPRs to microwave circuitry has been investigated for different conductor strip and strip separation widths. Three devices with small strip and separation width ($s = 10$ $\mu$m and $w = 5$ $\mu$m), and coupling gaps of 4, 6, 8 $\mu$m were classed as weakly coupled. When extracting the loaded $Q$ of these samples (see section 8), the unloaded $Q$ is shown to be independent of the coupling. Three devices with larger strip and separation width ($s = 30$ $\mu$m and $w = 15$ $\mu$m), and coupling gaps of 4, 8, 15 $\mu$m were classed as strongly coupled. The unloaded $Q$ is not independent of the coupling of the CPR to the microwave circuitry.

Both simulated and measured values of $Q$ show an increase with coupling gap width (see figure 11.15). Deviations of simulated from measured values may be due to additional measurement losses unaccounted for by the simulation. More measurements would be

needed to determine a correlation (see chapter 9 and section 11.3).

The primary aim of this work is to design CPRs with high $Q$ factors for the purpose of providing an investigative tool suitable for scientific research into quantum computing and cavity quantum electrodynamics. As stated in chapter 11, it is difficult to achieve the resolution necessary for the fabrication of QUBITs within the gap of a Niobium CPR with a high $Q$ on a Sapphire substrate. The required resolution for QUBIT fabrication can be achieved with oxidized Silicon substrates. However, the greater number of TLS inherent within this substrate reduces $Q$, making it difficult to produce a device suitable for the study of QUBIT/CPR interaction. As discussed previously, $Q$ can be increased in these devices by the saturation of TLS with the application of high microwave input power.

To observe QUBITs/CPR interaction, the power applied to a CPR must be low enough to ensure a low number of photons within the cavity [46]. High microwave powers, that correspond to $< n > \geq 5$ photons within the cavity, significantly alter the "bare" systems and observed spectrum splitting (see simulations from reference [6, 7]). Therefore it is not possible to saturate these TLS and observe the interaction between the QUBIT and the CPR.

It is the opinion of the author that using a Niobium CPR on a Sapphire substrate to observe the interaction between a CPR and a QUBIT is not possible due to the difficulty in fabricating these devices. This interaction has been observed with Niobium CPR on oxidized Silicon substrate devices within the limits on $Q$ imposed by the presence of TLS [1].

Wallraff *et al* [1] have measured the spectroscopic splitting due to the degeneracy between a CPR and a QUBIT, with a coupling strength of $g/2\pi = 11.6$ MHz, QUBIT decoherence $\gamma/2\pi = 0.7$ MHz, and photon loss rate of $\kappa/2\pi = 0.8$ MHz. Preliminary calculations based on the coupling between a flux QUBIT with dimensions given in reference [6] and a CPR (with Silicon Dioxide substrate) predicts the coupling rate to be $g/2\pi = 35$ MHz. Derived QUBIT decoherence rate based on present literature is $\gamma/2\pi = 1$ MHz, and photon loss rate extracted from measurements is $\kappa/2\pi = f_0/Q = 0.01$ MHz.

A higher CPR $Q$ factor results in low photon loss rate and longer coherence times. A high $Q$ factor CPR also results in a higher resolution for observing the spectroscopic splitting between a CPR and a QUBIT. Due to very precise fabrication techniques CPR devices (on oxidized Silicon substrate) made here exhibit high $Q$ factors in the presence of inherent TLS processes. These CPR devices can thus be implemented to realise quantum bit experiments.

## *13.2 Magnetic Measurements*

The tunability of a CPR by an external magnetic field is $\approx 0.05$ % from $f_0 \approx 6$ Ghz, with a high and unperturbed $Q$ factor $\sim 500,000$ (see figure 12.1). This shift in the resonant frequency corresponds to $\sim 200$ linewidths (linewidth is defined as the shift in resonant frequency divided by the bandwidth of the resonance). Rotating the applied magnetic field around the equator of the CPR, shows a periodic decrease and increase in resonant frequency for the field applied perpendicular and parallel to the surface of the CPR. This is evidence that the perturbation of the resonant frequency is associated with the flux focusing of the magnetic field in the gap between the conductor strip and outer ground planes.

The estimated flux focusing of the device is based upon a simple ellipsoid shape, and is shown to be in the region of $50 - 15000$. Using the Niobium critical field of 0.1 T [31], and the magnetic field data at which the resonant frequency and $Q$ deviates away from the expected response, the CPR has been shown to have a flux focusing of 400. This is within the estimated flux focusing calculated for this device.

The higher harmonics are also subjected to changes in the resonant frequency by an applied magnetic field. The higher harmonics change in the ratio of $f_3 : f_2 : f_1 = 2.8 : 1.8 : 1$. This is different to the $3 : 2 : 1$ ratio expected by this model, but it should be noted that the flux focusing is slightly non-uniform near the ends of the CPR, and that the different resonant modes are sensitive to different parts of the sample.

The effect of flux focusing the magnetic field on the superconducting material, is to modify the penetration depth of the superconductor in accordance with Ginzburg-Landau

theory [37]. The penetration depth is shown to have an $H^2$ dependence, which is reflected in the quadratic nature of the response of the resonant frequency to the applied magnetic field.

A shift in the resonant frequency is also shown for a quarter wavelength Niobium CPR on oxidized Silicon. For a field of 0.36 mT, a shift in resonant frequency of 0.5 MHz is measured (see figure 12.4). This shift in resonant frequency is much less then previously measured. This is attributed to differences in the fabrication process of the two samples.

An inbuilt current control line fabricated on chip is used to perturb the resonant frequency of the CPR. The current control line is $\approx 1\%$ the length of the inner conductor strip, situated near the resonator centre. An external field of 0.122 mT is applied by the Helmholtz coil to provide a non-zero resonant frequency offset $\mathrm{d}f_0/\mathrm{d}B$, this provides maximal sensitivity to the current applied by the control line. Applying a current of 250 mA produces a shift in the resonant frequency of 85 Khz, and this corresponds to $\approx 3$ linewidths (see figure 12.5). It should be noted that the $Q$ in this case is not particularly high, hence the bandwidth is broad, and this limits the number of linewidths by which the resonance moves. The $Q$ however, remains constant with changing current applied to the current control line.

The small shift in resonant frequency is attributed to the magnetic field generated by the current control line that is a small percentage of the total length of the inner conducting strip. Increasing the length of the current control line, should hypothetically increase the shift in the resonant frequency. The low $Q$ is attributed to overcoupling the CPR to the current control line, analogous to overcoupling a CPR via coupling capacitors as discussed above.

Lastly, CPRs made from superconducting-ferromagnet-superconducting (SFS) trilayers on oxidized Silicon are fabricated. The resonant frequency is 6.24 Ghz, and $Q = 25,000$ (see figure 12.6). The low $Q$ is attributed to overcoupling the CPR with the microwave circuitry, that effectively dampens the $Q$. The shift in resonant frequency $\approx 1$ MHz (see figure 12.7), is similar to the shift in resonant frequency of half wavelength Niobium on oxidized Silicon CPRs.

## 13.3 Further Research

Decoherence due to TLS within oxidized Silicon is apparent from the measurements of resonant frequency and $Q$ as a function of temperature and power. This source of loss adds to the decoherence when observing the interaction between a CPR and a QUBIT. It has been shown that these TLS are saturated by high microwave powers, but that this is also shown through simulations to alter the observed energy level spectrum. This makes it difficult to observe the interaction between a CPR and a QUBIT.

The origin of these TLS could be investigated through spectroscopy. This could identify whether TLS are paramagnetic impurities or dangling bonds within the oxidized Silicon. If it is found that TLS are due to paramagnetic impurities within the oxidized Silicon, then it may be possible to either thermally grow/deposit oxidized Silicon with increased purity. If the origin of TLS is found to be dangling bonds, then there are well developed techniques within the semiconductor industry for eliminating these bonds [78, 79].

It has been shown that SFS CPRs are capable of producing $Q \sim 10^4$, further research into sample deposition and fabrication may yield $Q \sim 10^6$. If this is achieved, then SFS CPRs strongly coupled with SFS QUBITs would potentially produce effects similar to, and better than the effects observed by Wallraff *et al* [1], in terms of less decoherence introduced through the coupling of the current control line to the CPR.

# 14. DECLARATION

The results shown in the figures below are from samples fabricated by the author:

| |
|---|
| Figure 11.1 |
| Figure 12.6 |
| Figure 12.4 |
| Figure 12.5 |

*Tab. 14.1:* Samples fabricated by the author.

The results shown in the figures below are from samples fabricated by StarCryo:

| |
|---|
| Figure 11.2 |
| Figure 11.3 |
| Figure 11.6 |
| Figure 11.7 |
| Figure 11.10 |
| Figure 11.13 |
| Figure 11.11 |

*Tab. 14.2:* Samples fabricated by StarCryo.

# BIBLIOGRAPHY


[1] A. Wallraff, D. I. Schuster, A. Blais, L. Frunzio, R.- S. Huang, J. Majer, S. Kumar, S. M. Girvin and R. J. Schoelkopf. "Circuit quantum electrodynamics: Coherent coupling of a single photon to a Cooper pair box", *Nature*, **431**, 162-167, 2004.

[2] M. A. Sillanp, J. I. Park and R. W. Simmonds. "Coherent quantum state storage and transfer between two phase qubits via a resonant cavity", *Nature*, **449**, 438-442, 2007.

[3] Peter K. Day, Henry G. LeDuc, Benjamin A. Mazin, Anastasios Vayonakis and Jonas Zmuidzinas. "A broadband superconducting detector suitable for use in large arrays", *Nature*, **425**, 817-821, 2003.

[4] J. J. Wingfield, J. R. Powell, C. E. Gough, A. Porch. "Sensitive measurement of the surface impedance of superconducting single crystals using a sapphire dielectric resonator", *IEEE Transactions On Applied Superconductivity* **7**, 2, 2009 - 2012, 1997.

[5] L. Frunzio, A. Wallraff, D. I. Schuster, J. Majer, and R. J. Schoelkopf. "Fabrication and characterization of superconducting circuit QED devices for quantum computation", *IEEE Transactions On Applied Superconductivity*, **15**, 2, 860-863, 2005.

[6] T. Lindstrom, C. H. Webster, A. Ya. Tzalenchuk, J. E. Healey, M. S. Colclough, C. M. Muirhead. "Circuit QED with a flux qubit strongly coupled to a coplanar transmission line resonator", *Superconductor Science and Technology*, **20**, 814-821, 2007.

[7] T. Lindstrom, J. E. Healey, M. S. Colclough, C. H. Webster, C. M. Muirhead, and

A. Ya. Tzalenchuk. "Numerical simulations of a flux qubit coupled to a high quality resonator", *Journal of Physics: Conference Series*, 97, 012319, 2008.

[8] A. Porch, P. Mauskopf, S. Doyle, and C. Dunscombe. "Calculation of the characteristics of coplanar resonators for kinetic inductance detectors", *IEEE Transactions On Applied Superconductivity*, **15**, 2, 552-555, 2005.

[9] S. Doyle, P. Mauskopf, J. Naylon, A. Porch and C. Dunscombe. "Lumped element kinetic inductance detectors", *Journal of Low Temperature Physics*, **151**, 1-2, 530-536, 2008.

[10] B. A. Mazin, P. K. Day, J. Zmuidzinas, H. G. LeDuc. "Multiplexable kinetic inductance detectors", *AIP Conference Proceedings*, **605**, 309, 2002.

[11] C. P. Wen. "Coplanar Waveguide, a Surface Strip Transmission Line Suitable for Nonreciprocal Gyromagnetic Device Applications", *Microwave Symposium Digest, G-MTT International*, **69**, 1, 110-115, 1969.

[12] C. E. Gough, A. Porch, M. J. Lancaster, J. R. Powell, B. Avenhaus, J. J. Wingfield, D. Hung and R. G. Humphreys, "High Tc co-planar resonators for microwave applications and scientific studies", *Physica C*, **282-287**, 395-398, 1997.

[13] Introduction to Superconductivity, Second edition. M. Tinkham, *Dover*, Pg 106-109, 2004.

[14] J. J. A. Baselmansa, R. Barendsb, J. N. Hovenierb, J. R. Gaoa, b, H. Hoeversa and T. M. Klapwijk. "Development of high-Q superconducting resonators for use as kinetic inductance sensing elements Development of high-Q superconducting resonators for use as kinetic inductance sensing elements", *Nuclear Instruments and Methods in Physics Research Section A:* **559**, 567-569, 2006.

[15] J. Zmuidzinas, and P. L. Richards. "Superconducting detectors and mixers for millimeter and submillimeter astrophysics", *Proceedings of the IEEE*, **92**, 10, 1597-1616, 2004.

[16] H. Wang, M. Hofheinz, M. Ansmann, R. C. Bialczak, Erik Lucero, M. Neeley, A. D. O'Connell, D. Sank, M. Weides, J. Wenner, A. N. Cleland, John M. Martinis. "Decoherence Dynamics of Complex Photon States in a Superconducting Circuit", *Physical Review Letters*, **103**, 200404, 2009.

[17] M. Metcalfe, E. Boaknin, V. Manucharyan, R. Vijay, I. Siddiqi, C. Rigetti, L. Frunzio, R. J. Schoelkopf, and M. H. Devoret. "Measuring the decoherence of a quantronium qubit with the cavity bifurcation amplifier", *Physical Review B*, **76**, 174516, 2007.

[18] A. A. Houck, J. A. Schreier, B. R. Johnson, J. M. Chow, Jens Koch, J. M. Gambetta, D. I. Schuster, L. Frunzio, M. H. Devoret, S. M. Girvin, R. J. Schoelkopf. "Controlling the Spontaneous Emission of a Superconducting Transmon Qubit", *Physical Review Letters*, **101**, 080502, 2008.

[19] I. Serban, E. Solano, F. K. Wilhelm. "Crossover from weak- to strong-coupling regime in dispersive circuit QED", *A Letters Journal Exploring the Frontiers of Physics*, **80**, 40011, 2007.

[20] D. I. Schuster, A. A. Houck, J. A. Schreier, A. Wallraff, J. M. Gambetta, A. Blais, L. Frunzio1, J. Majer, B. Johnson, M. H. Devoret, S. M. Girvin, and R. J. Schoelkopf. "Resolving photon number states in a superconducting circuit", *Nature*, **445**, 515-518, 2007.

[21] E. M. Purcell. "Spontaneous emission probabilities at radio frequencies", *Physical Review*, **69**, 3906, 1946.

[22] "Quantum Optics: An Introduction, M. Fox." *Oxford Master Series in Physics*, **6**, 126-187, 2006.

[23] J. E. Mooij, T. P. Orlando, L. Levitov, Lin Tian, Caspar H. van der Wal, Seth Lloyd. "Josephson Persistent-Current Qubit", *Science*, **285**, 1036, 1999.

[24] I. Chiorescu, Y. Nakamura, C. J. P. M. Harmans, and J. E. Mooji. "Coherent Quantum Dynamics of a Superconducting Flux Qubit", *Science* **229**, 1869-1871, 2003.

[25] J. W. A. Robinson, S. Piano, G. Burnell, C. Bell, and M. G. Blamire. "Critical Current Oscillations in Strong Ferromagnetic $\pi$ Junctions", *Physical Review Letters* **97**, 177033, 2006.

[26] M. J. Lancaster, J. Powell and A. Porch. "Thin-film ferroelectric microwave devices", *Superconductor Science and Technology*, **11**, 1323-1334, 1998.

[27] D. Seron, H. Kokabi, M. Rabii, M. Boulay and G. Alquie. "A study of magnetic tunability in a superconductor coplanar resonator using a calcium, vanadium and garnet ferrite", *Superconductor Science and Technology*, **17**, 904-907, 2004.

[28] A. Palacios-Laloy, A. F. Nguyen, F. Mallet, P. Bertet, D. Vion, and D. Esteve. "Tunable Resonators for Quantum Circuits", *Journal of Low Temperature Physics*, **151**, 1034-1042, 2008.

[29] M. Sandberg, M. Wilson, C. M. Persson, F. Johansson, G. Shumeiko, V. Bauch, T. Duty, T. Delsing. "Fast tuning of superconducting microwavecavities", *American Institute of Physics, Conference Proceedings*, **1074**, 12-21, 2008.

[30] M. A. Castellanos-Beltran, and K. W. Lehnert. "A widely tunable parametric amplifier based on a SQUID array resonator", *Applied Physics Letters*, **91**, 083509, 2007.

[31] Introduction to Solid State Physics, Eighth edition, *Wiley International Edition*, Pg 259-296, 2005.

[32] L. N. Cooper. "Bound electron pairs in a degenerate fermi gas", *Physical Review*, **104 (4)**, 11891190, 1956.

[33] Introduction to Superconductivity, Second edition. M. Tinkham, *Dover*, Pg 43-46, 2004.

[34] Introduction to Superconductivity, Second edition. M. Tinkham, *Dover*, Pg 18-19 and 22-32, 2004.

[35] C. J. Gorter and H. Casimir. "On Supraconductivity I", *Physica*, **1**: 306-320, 1934.

[36] Superconductivity. Charles P. Poole, Horacio A. Farach, Richard J. Creswick, *Elsevier*, pg 126, 1995.

[37] V. L. Ginzburg, and L. D. Landau. *Zh. Eksp. Teor. Fiz.* **20**, 1064, 1950.

[38] Superconductivity of Metals and Cuprates, J. R. Waldram. *Institute of Physics Publishing, Bristol and Philadelphia*, pg 51-52 1996.

[39] A. B. Pippard. *Proceedings Of The Royal Society A*, "Field Variation of the Superconducting Penetration Depth", **203**, 210-223, 1950.

[40] S. K. Yip, and J. A. Sauls. "Nonlinear Meissner effect in CuO superconductors", *Physical Review Letters*, **69**, 15, 2264-2267, 1992.

[41] Electromagnetism, I. S. Grant and W. R. Phillips. *Wiley*, 2 edition, 388-390, January 1991.

[42] "A Guide to characteristation of dielectric materials at RF and microwave frequencies", *National Physical Laboratory*, Pg 10-81, 2003.

[43] Passive Microwave Device Applications of High-Temperature Superconductors. M. Lancaster. *Cambridge University Press,* Pg 316, 1997.

[44] W. A. Phillips. "Two-level states in glasses", *Reports on Progress in Physics*, **50**, 1657, 1987.

[45] R. Barends, H. L. Hortensius, T. Zijlstra, J. J. A. Baselmans, S. J. C. Yates, J. R. Gao, and T. M. Klapwijk. "Contribution of dielectrics to frequency and noise of NbTiN superconducting resonators", *Applied Physics Letters*, 92, 22, 223502, 2008.

[46] T. Lindstrom, J. E. Healey, M. S. Colclough, C. M. Muirhead, A. Ya. Tzalenchuk. "Properties of superconducting planar resonators at millikelvin temperatures", *Physical Review B*, 80, 132501, 2009.

[47] F. A. Miranda, W.L. Gordon, 0. Heinen, B. T. Ebihara, and K. B. Bhasin. "Measurements of Complex Permittivity of Microwave Substrates in the 20 to 300 K Temperature Range from 26.5 to 40.0 GHz", *NASA Technical Memorandum*, 102123, 1989

[48] J. Krupka, J. Breeze, N. Alford, A. E. Centeno, L. Jensen, T. Claussen. "Measurements of permittivity and dielectric loss tangent of high resistivity float zone silicon at microwave frequencies", *IEEE Transactions on Microwave Theory and Techniques*, **54**, 11, 3995-4001, 2006

[49] J.Gao, M. Daal, A. Vayonakis, S. Kumar, J. Zmuidzinas, B. Sadoulet, B. A. Mazin, P. K. Day, and H. G. Leduc. "Experimental evidence for a surface distribution of two-level systems in superconducting lithographed microwave resonators", *Applied Physics Letters*, **92**, 15, 152505, 2008.

[50] Coplanar Waveguide Circuits, Components and Systems. R. N. Simons. *Wiley-Interscience*, pg 11-33, 2001.

[51] Coplanar Waveguide Circuits, Components and Systems. R. N. Simons. *Wiley-Interscience*, pg 401, 2001.

[52] "http://www.ansoft.com/products/hf/hfss/"

[53] F. Aiga, H. Fuke, Y. Terashima, M. Yamazaki, H. Kayano, and T. Hashimoto. "HTS hairpin microstrip filter on r-cut sapphire substrate", *IEEE Transactions on Applied Superconductivity* **13**, 2, 287-290, 2003.

[54] Field Theory of Guided Waves. R. E. Collins *IEEE Press Series on Electromagnetic Waves*, Second Edition, Pg 189-192, 1991.

[55] Microwave Engineering, D. M. Pozar, *Addison-Wesley Publishing Company*, Pg 220-240, and 107-109, 1990.

[56] "http://www.clippercontrols.com/info/dielectric_constants.htmlS"

[57] V. N. Egorov, V. L. Masalov, and I. B. Ozhogov. "Anisotropy of dielectric losses in $Al_2O_3$ and $SiO_2$ single crystals", *Technical Physics Letters*, 30, 12, 2009.

[58] X. Aupi, J. Breeze, N. Ljepojevic, L. J. Dunne, N. Malde, A. Axelsson, and N. McN. Alforda. "Microwave dielectric loss in oxides: Theory and experiment", *Journal of Applied Physics*, 95, **5**, 2004.

[59] J. Sok, J. S. Lee, and E. H. Lee. "Tunability and loss tangent of ferroelectric films in superconducting resonator ", *Superconducting Science and Technology*, **11**, 9, 1998

[60] "http://www.ni.com/labview/"

[61] "http://www.rogerscorporation.com/mwu/pdf/6000data.pdf" RT Duroid 6010

[62] "http://www.wrcad.com/freestuff.html"

[63] "http://www.photomask.com/"

[64] "http://www.starcryo.com/"

[65] "http://www.lakeshore.com/temp/sen/crtd.html"

[66] A. N. Broers, A. C. F. Hoolea and J. M. Ryan. "Electron beam lithography - resolution limits", *Microelectronic engineering*, **32**, issues 1-4, pages 131-142, 1996.

[67] J. A. Nelder, and R. Mead. "A simplex method for function minimization", *Computer Journal*, **7**, pages 308313, 1965.

[68] A. I. Gubin, K. S. Ilin, S. A. Vitusevich, M. Siegel, and N. Klein. "Dependence of magnetic penetration depth on the thickness of superconducting Nb thin", *Physical Review B*, **72**, 064503, 2005

[69] C. J. Grebenkemper and J. P. Hagen. "The Dielectric Constant of Liquid Helium", *Physical Review*, **80**, 89-89, 1950

[70] T. Lindstrom, J. E. Healey, M. S. Colclough, C. H. Webster, C. M. Muirhead, and A. Ya. Tzalenchuk. "Properties of high-quality coplanar waveguide resonators for QIP

and detector applications ", *Journal of Physics: Conference Series,* 150, 052140, 2009.

[71] S. K. Lai. "Interface trap generation in silicon dioxide when electrons are captured by trapped holes", *Journal of Applied Physics* **54**, 5, 2540 - 2546, 1983.

[72] Meng Tao, Darshak Udeshi, Nasir Basit, Eduardo Maldonado, and Wiley P. Kirk, "Removal of dangling bonds and surface states on silicon .001. with a monolayer of selenium", *Applied Physics Letters*, **82**, 10, 1559-1561, 2003.

[73] N. Boulant, G. Ithier, P. Meeson, F. Nguyen, D. Vion, I. Siddiqi, R. Vijay, C. Rigetti, and F. Pierre. "Quantum nondemolition readout using a Josephson bifurcation amplifier", *Physical Review B*, **76**, 014525, 2007.

[74] "http://en.wikipedia.org/wiki/Silicondioxide"

[75] "http://en.wikipedia.org/wiki/Sapphire"

[76] J. E. Healey, T. Lindström, M. S. Colclough, C. M. Muirhead, and A. Ya. Tzalenchuk. "Magnetic field tuning of coplanar waveguide resonators", *Applied Physics Letters*, **93**, 4, 043513, 2008.

[77] "http://en.wikipedia.org/wiki/Coercivity"

[78] M. Tao, J. Shanmugam, M. Coviello and W. P. Kirk. "Suppression of silicon (001) surface reactivity using a valence-mending technique ", *Solid State Communications*, **132**, 2, 89-92, 2004.

[79] E. Cartier, J. H. Stathis, and D. A. Buchanan. "Passivation and depassivation of silicon dangling bonds at the Si/SiO2 interface by atomic hydrogen", *Applied Physics Letters*, **63**, 11, 1510-1512, 1993.

# APPENDIX

# A. SIMULATIONS

The method for simulating these structures are shown below, and the example used is based on a normal metal half wavelength CPR, residing on a silicon substrate.

The CPR geometric structure is designed in a program called KIC and exported as a GDS file. These files are also sent to the mask fabricators as they form the basis of the mask designs of the CPRs. These files are then imported into HFSS and the different geometries are given constraints such as material type, boundary conditions, wave excitations, and mesh operations. Within the HFSS program, the CPR structure that is imported can be simulated as a 2D structure or extruded into a 3D structure. However, for simplicity and time constraints the structure is simulated as a 2D film. A typical CPR resides on a dielectric substrate, and this can be simulated as a box and assigned a substrate material from a vast and comprehensive library contained within the program. Finally, the whole structure is contained within an external box, either contacting all sides of the CPR or only partially, depending upon the type of simulation that is being undertaken.

There are three solvers to choose from, driven modal, driven terminal and eigenmode. The driven modal and driven terminal solvers use wave ports to direct the $EM$ field. The driven modal solver calculates the modal-based S parameters of the structure and expresses the S matrix in terms of incident and reflected powers of the waveguide mode. The driven terminal calculates the terminal-based S parameters, and expresses the S matrix in terms of the terminal voltages and currents. The eigenmode solver finds eigenmodes of lossy and lossless system depending on any bounded region in the design. A typical structure that is solved using the driven modal solver is shown below:

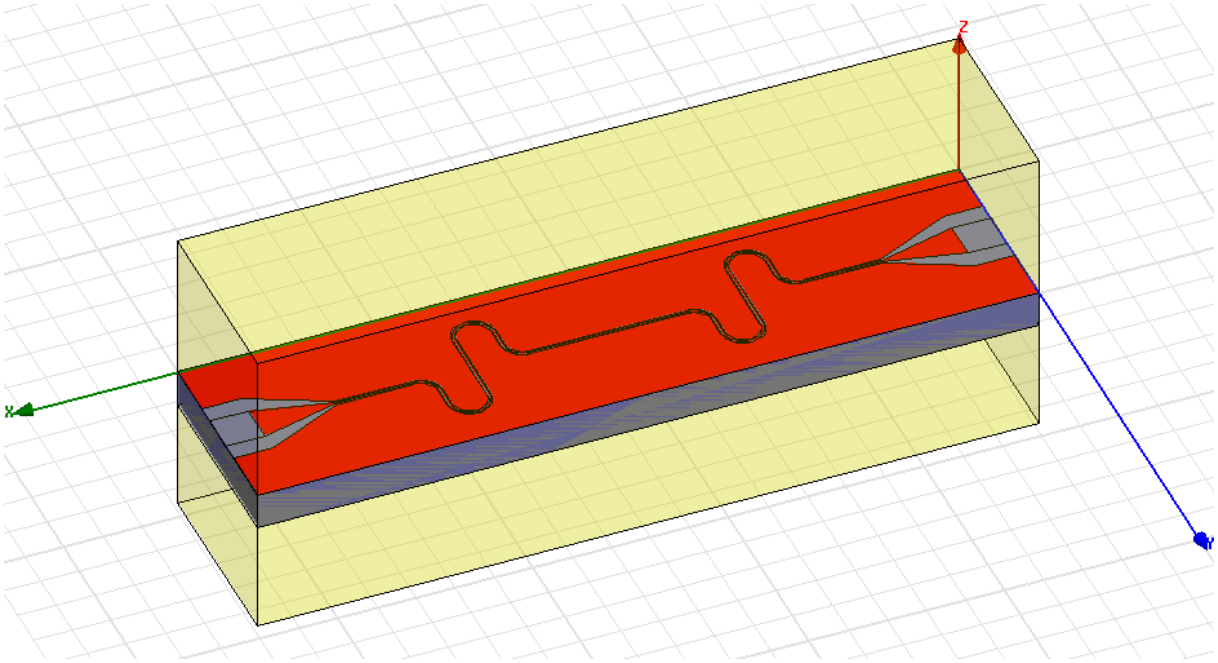


*Fig. A.1:* Half wavelength coplanar resonator with supporting box and substrate.

The example used here is a CPR with a length of 11 mm, with a width of 30 $\mu m$, gap separation of 15 $\mu m$ and a coupling gap of 15 $\mu m$. The CPR resides on a silicon substrate with $\epsilon_r = 11.9$ and loss tangent equal to zero. The top layer (red) is modelled as a perfectly electrically conducting (PEC) material to loosely represent a superconductor. Wave ports are assigned to opposite faces of a box enclosing the CPR. A requirement for placing a port on a face is to specify an electric field integration line. This electric field integration line is drawn from the middle of this face to the edge of the box to represent the direction where the peak E field resides on the CPR.

After specifying the structure and boundary regions within the HFSS window, the analysis process is then defined. To apply the analysis process, a relevant frequency is set that has an associated length scale within the structure (e.g. the CPR has a resonant frequency of 6 Ghz and wavelength of 5.5 mm so this will determine the appropriate length scale). The program then puts down a number of mesh elements, the number of which can be chosen by selecting a fraction of the wavelength that is to be meshed e.g. $0.1 \times \lambda$. The mesh that has initially been set up can be used for further simulations, however for certain structures with a high aspect ratio, applying the adaptive solution is more appropriate.

The adaptive solution puts mesh elements in relevant places to decrease the average error between mesh elements overlapping or leaving empty spaces. This also helps to resolve the Electric and magnetic field distributions. For this reason the mesh error in the matching of the elements is set low (typically 2 %) and the number of mesh iterations is kept high (say 10).

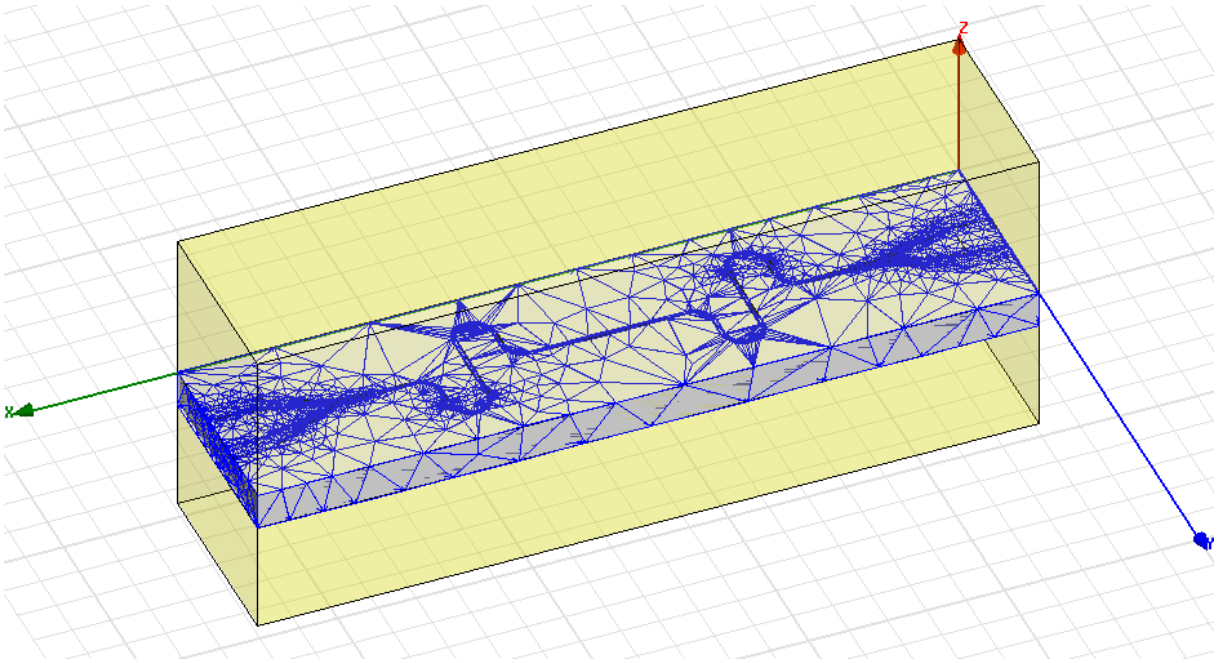


*Fig. A.2:* Adaptive mesh used to simulate the electromagnetic field pattern of a half wavelength resonator. For clarity, the mesh elements inside the larger box have been omitted.

Once the adaptive frequency has been set, the sweep function is then defined. There are three types of sweep functions, discrete, fast and interpolating. Selecting the discrete sweep function means that upon selecting the sweep frequency range and number of points, the program calculates all Maxwell's equations in each mesh element and for every frequency point specified. This is a very accurate way of extracting S and field parameters. This process can take a long time to solve, so to reduce the time of evaluation there are two other process that can be employed; the fast and interpolating frequency sweeps.

The fast frequency sweep finds the "poles and zeros" of the problem to calculate S parameters, it can also calculate fields at specific frequency points. The interpolating frequency sweep is usually used when a DC solution is required or a very broadband sweep.

HFSS chooses which frequency points are "ideal" for interpolating the S parameters. The downside is that it does not produce field patterns (just S/Y/Z parameters) however, a further discrete or fast frequency sweep can be used, while maintaining the same mesh from the previous sweep.

Once all of the above parameters have been defined and solved, the post processing of the details can be obtained. Typically the S parameters provide information regarding the successfulness of the CPR depending on its $Q$ and field distribution. The field distribution information can be used to find the correct location to place a flux or charge qubit to take advantage of the high energy density of the CPR to provide strong coupling for Qubit-CPR experiments.

The S parameters for the above model are shown below. The $Q$ in this case is fairly meaningless with reference to a superconducting material, however the simulation shows the capabilities of the HFSS program to cope with the CPR geometry.

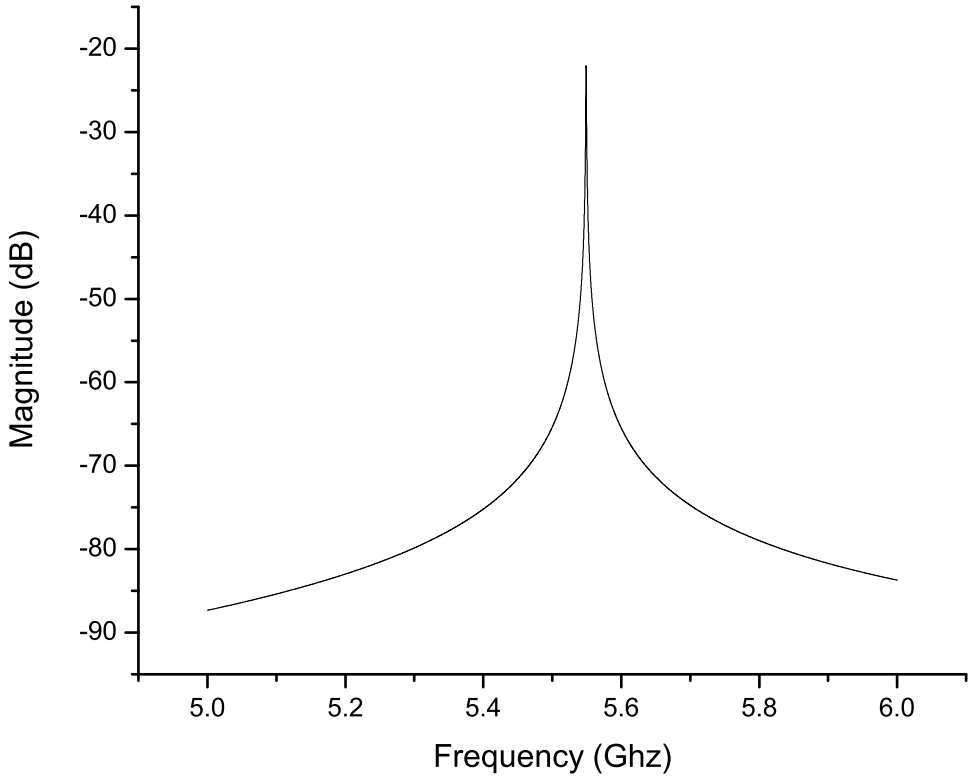


*Fig. A.3:* The transmission parameter (S21) as a function of the frequency applied.

The $E$ and $H$ field patterns for a CPR on resonance is shown below.

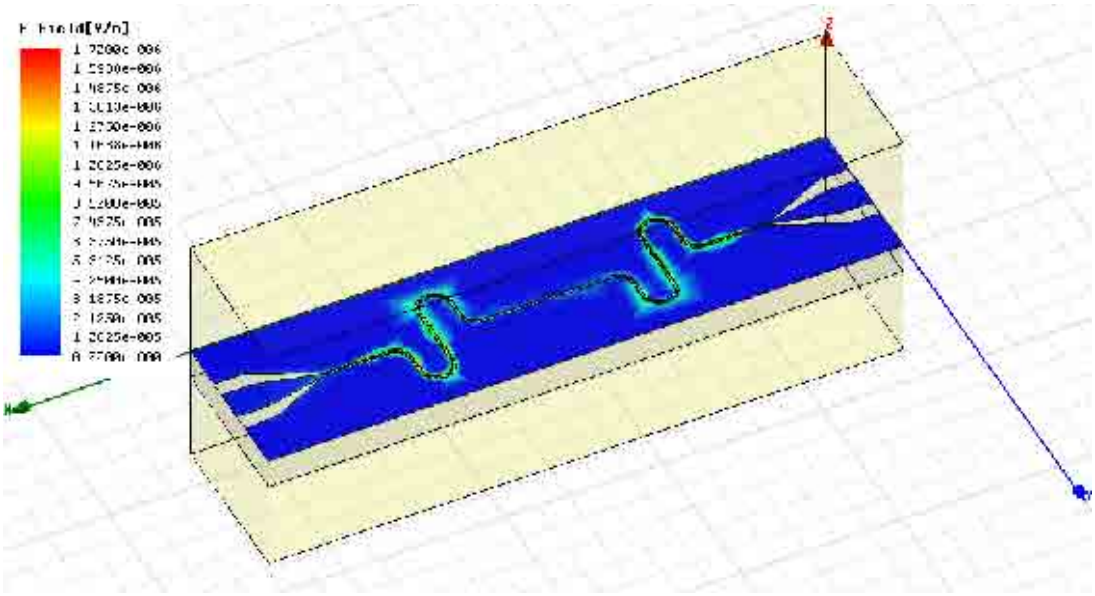

*Fig. A.4:* The $E$ field for a CPR on resonance.

The $E$ field peaks at the ends of the resonator, near the coupling capacitors and is zero at the centre. This is the field pattern for a typical fundamental mode of a CPR. Below is the response of the $H$ field:P

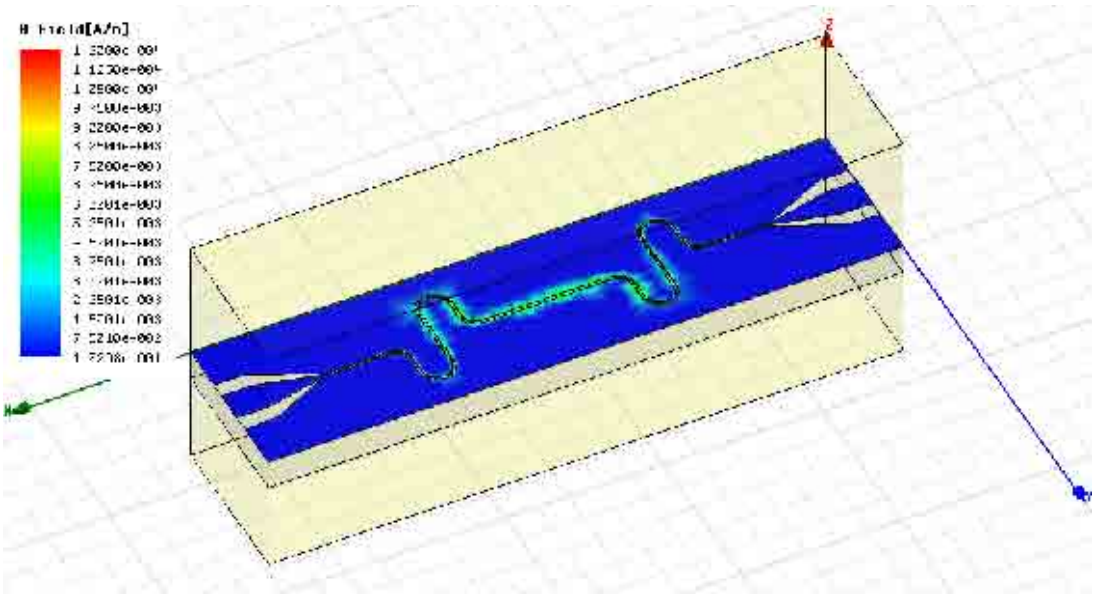

*Fig. A.5:* The $H$ field for a CPR on resonance.

The $H$ field peaks at the centre of the CPR and is a minimum at both ends near the coupling capacitors. The central position is an ideal location to place a flux QUBIT, for

strong coupling between the two devices.

It has been shown that HFSS is capable of simulating CPRs, therefore in the previous sections a thorough analysis of the CPR geometries are considered and simulated in detail.

# B. LABVIEW PROGRAM

Front end program.

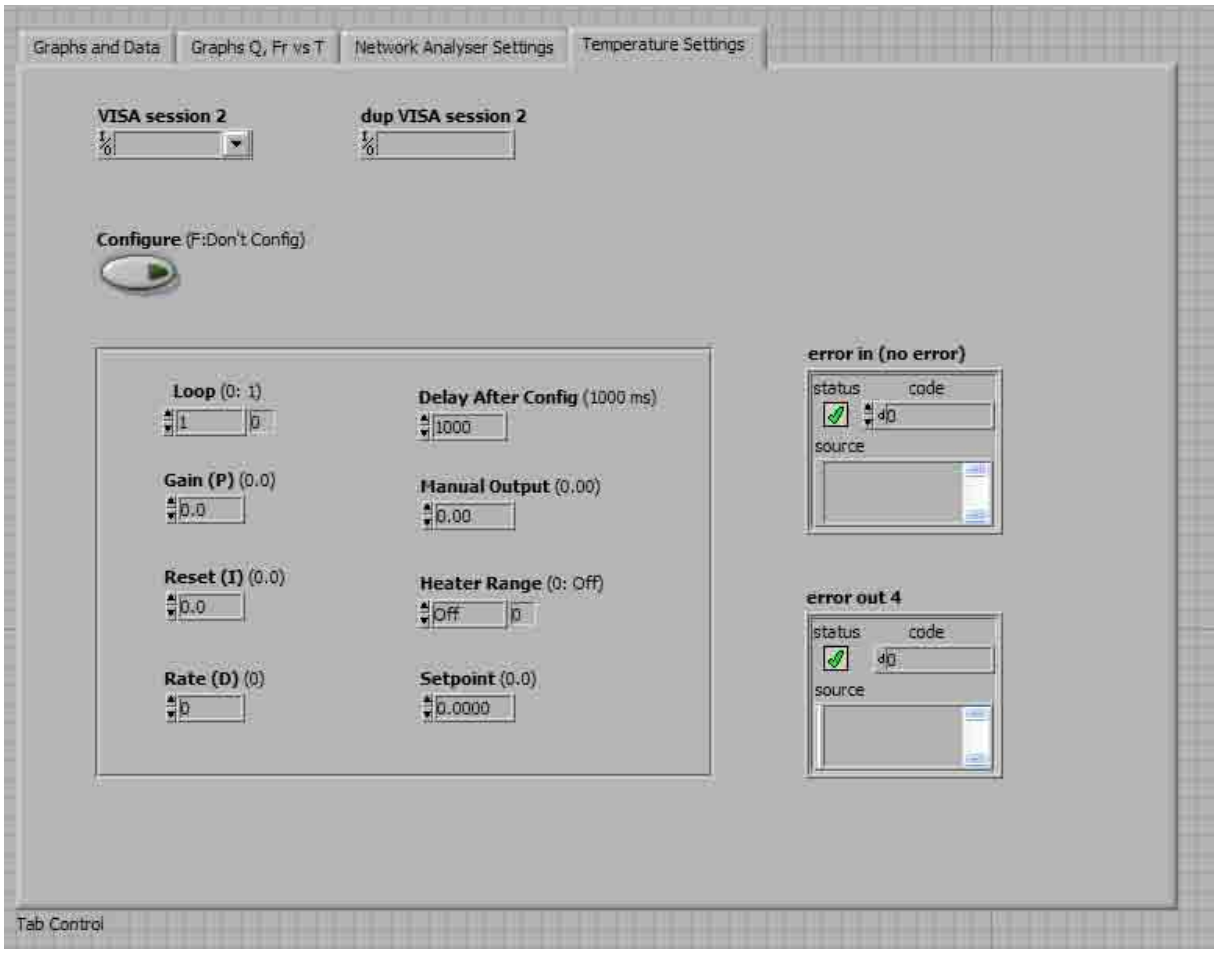


*Fig. B.1:* Temperature settings.

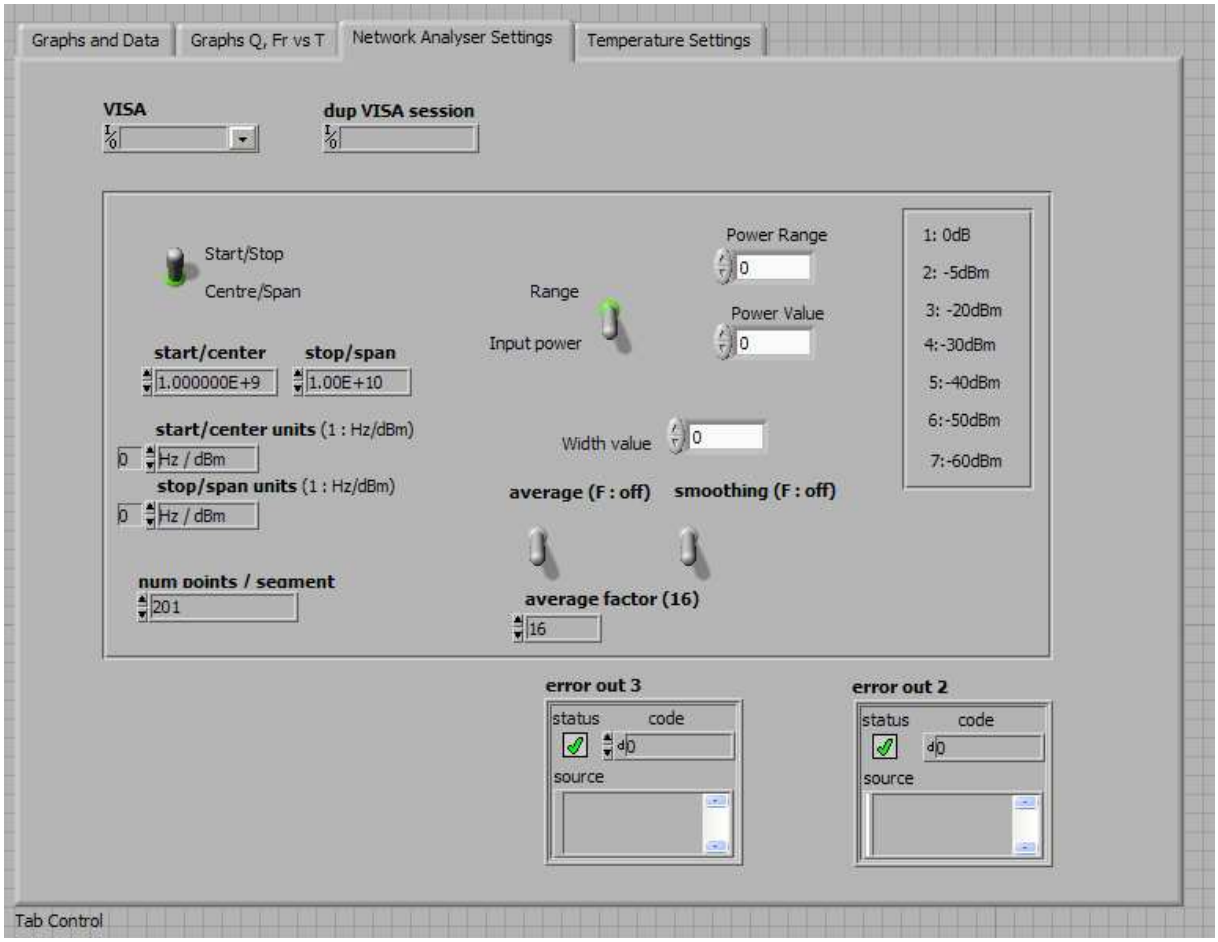


*Fig. B.2:* Network analyzer settings.

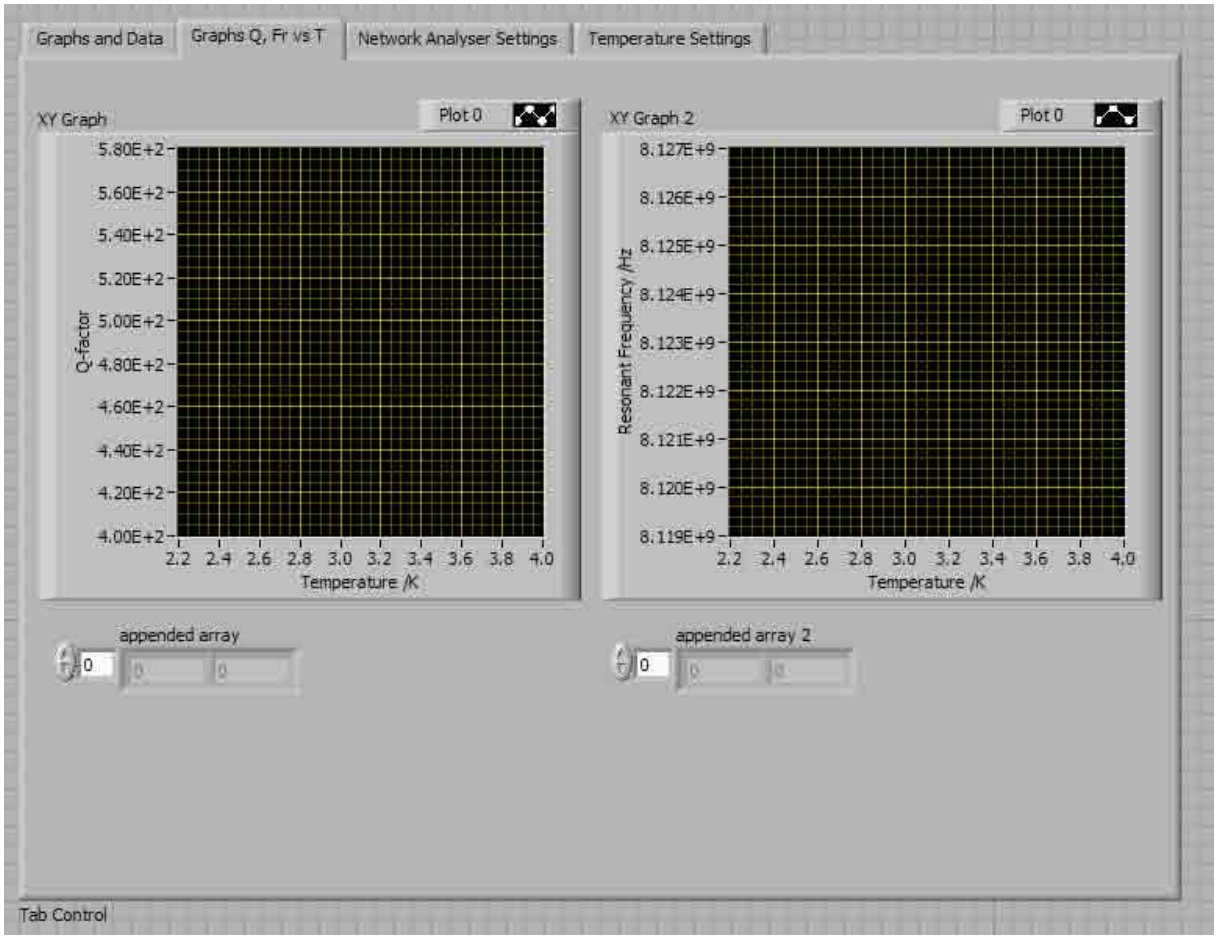


*Fig. B.3:* Plotting facilities.

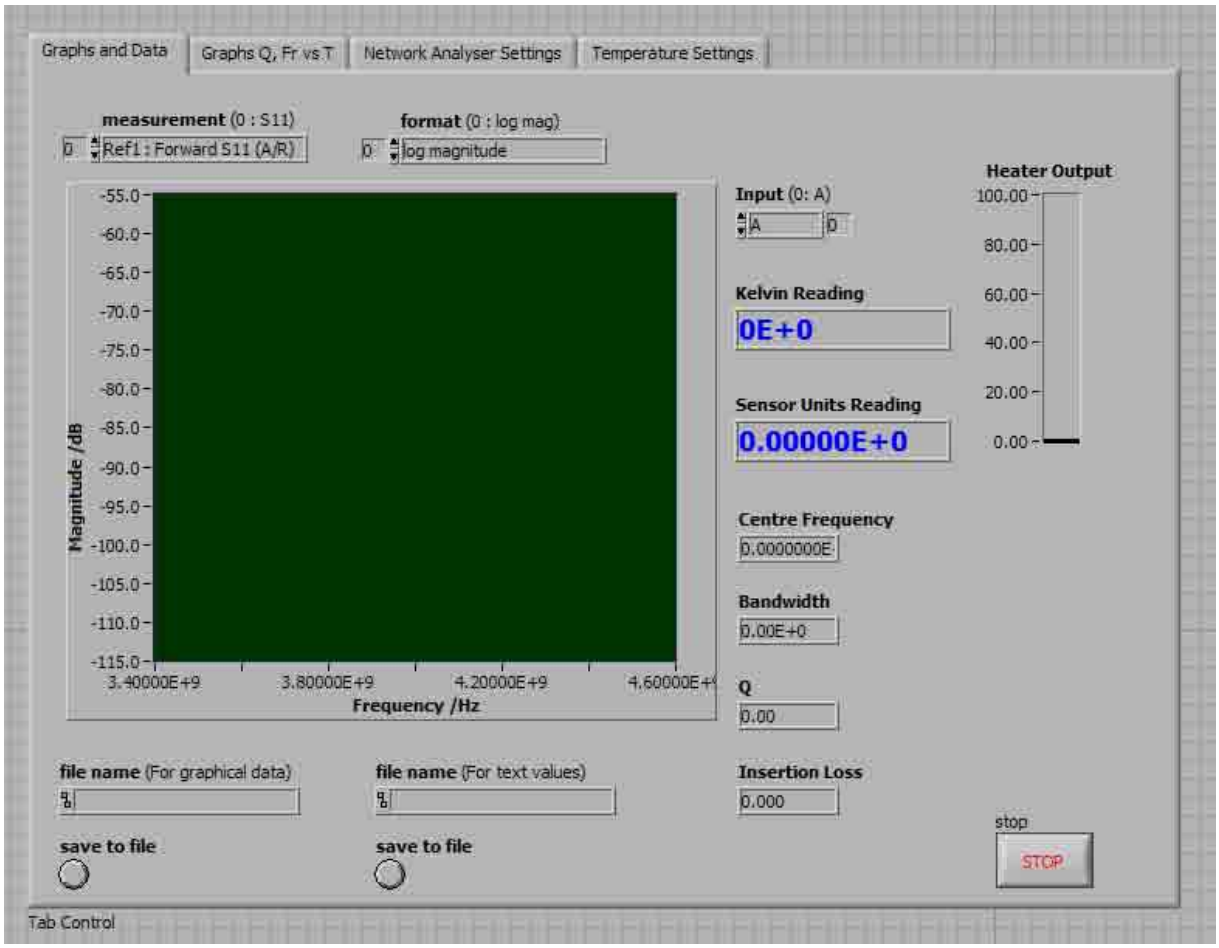


*Fig. B.4:* Plotting facilities.

Back end program.

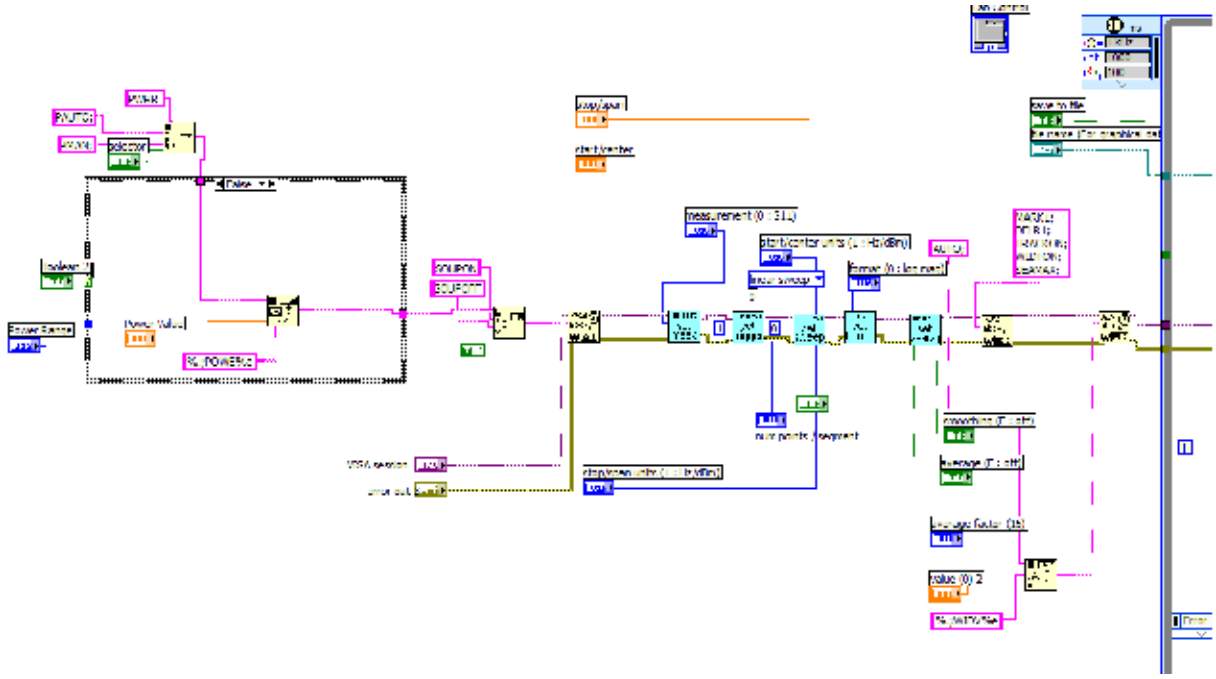

*Fig. B.5:* Initialising the network analyzer.

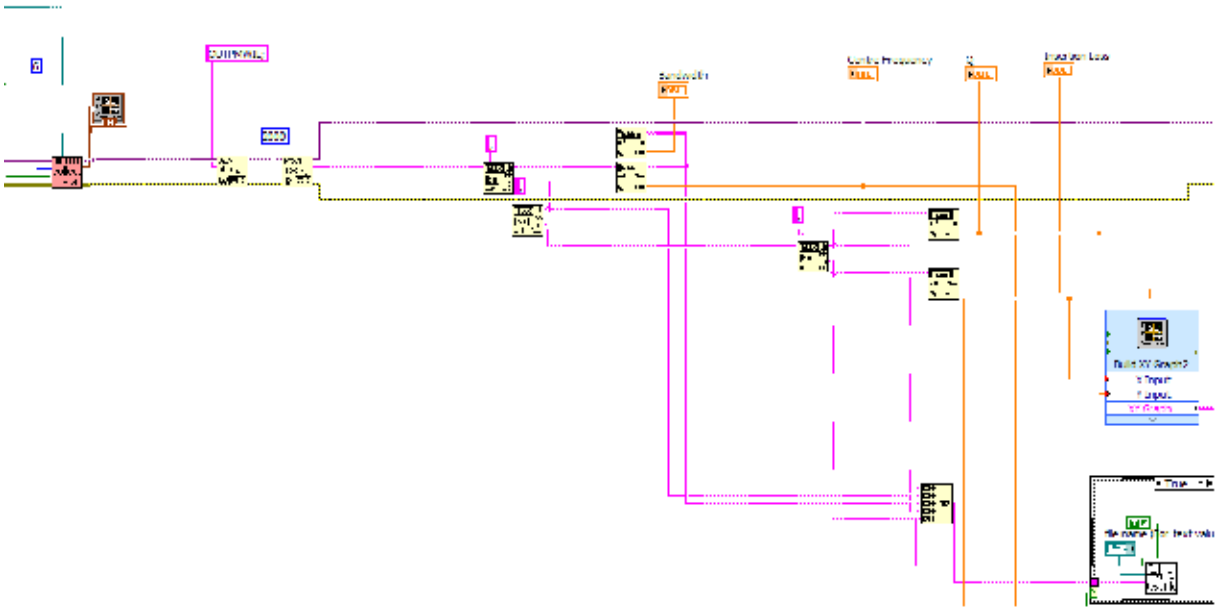

*Fig. B.6:* Selecting functions that are extracted from the network analyzer.

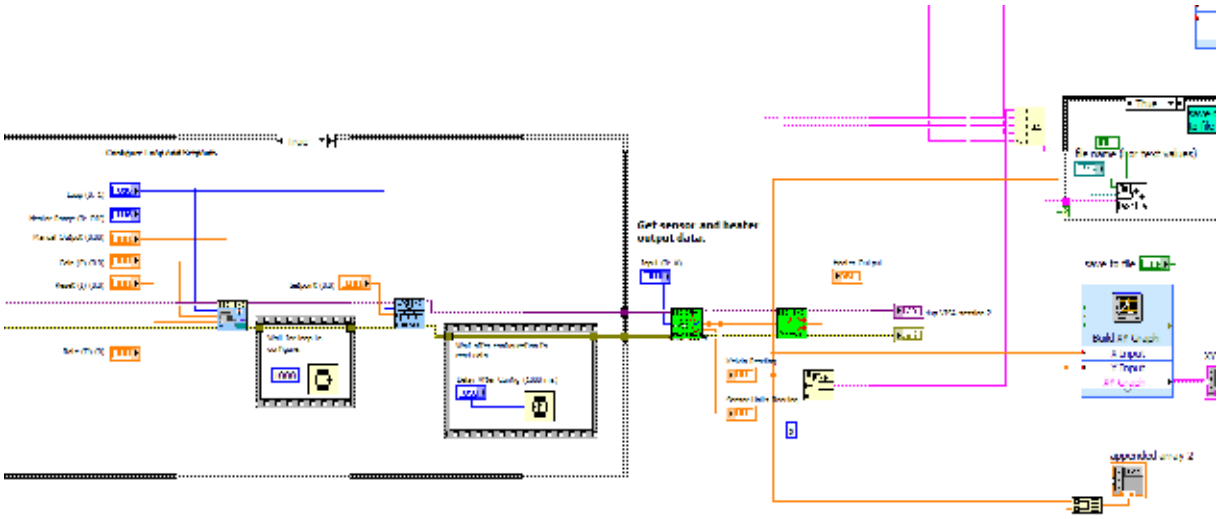


*Fig. B.7:* Selecting functions that are extracted from the temperature controller.

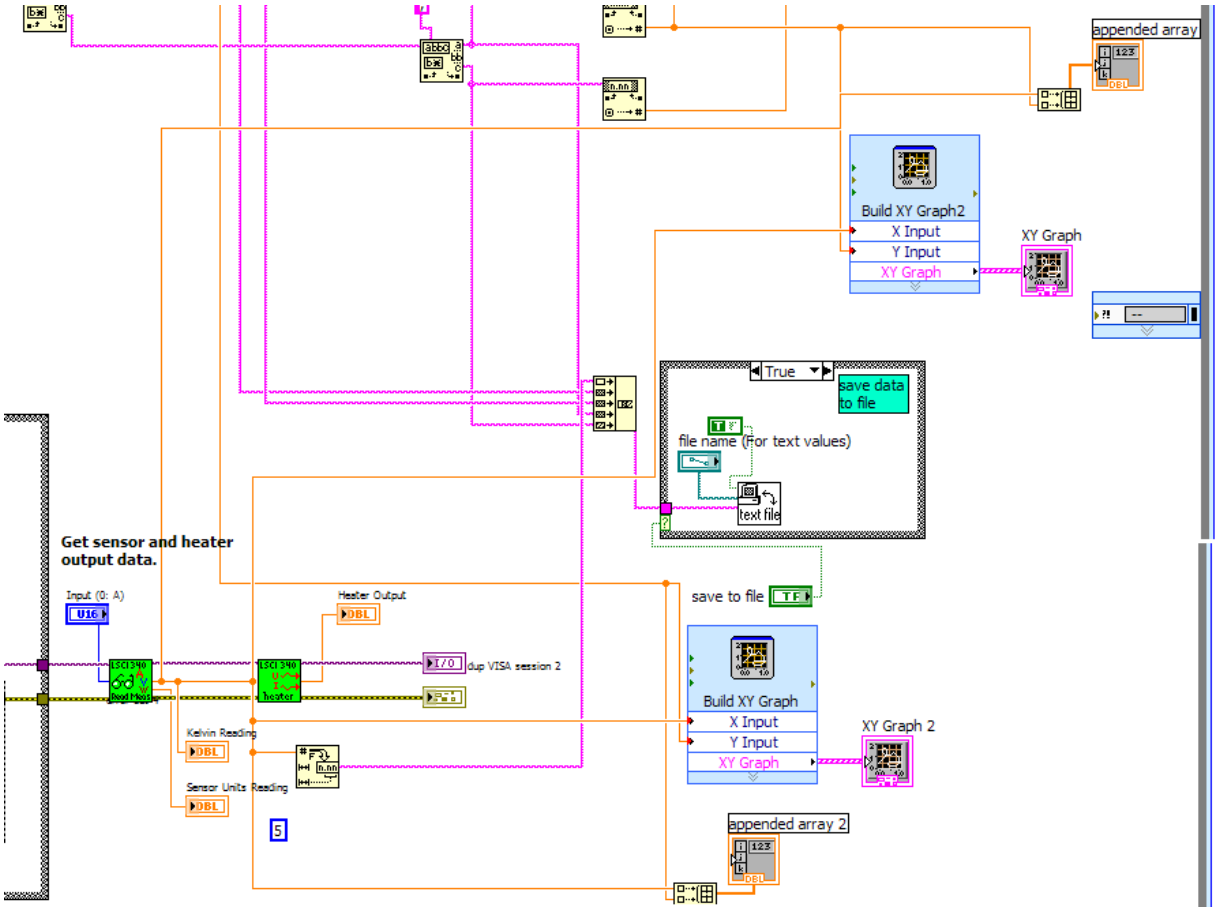


*Fig. B.8:* File capture, save and plotting functions.

# C. PHOTOLITHOGRAPHIC MASK

Photolithographic masks. An example of a half wavelength CPR

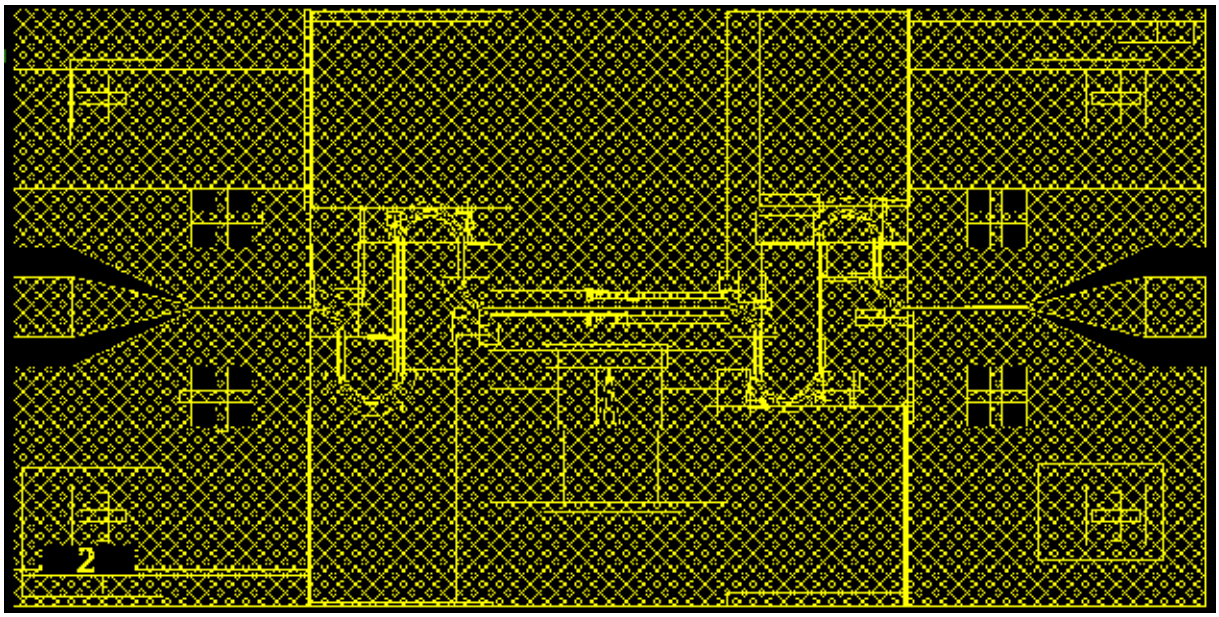


*Fig. C.1:* Half wavelength CPR.

An example of a KID.

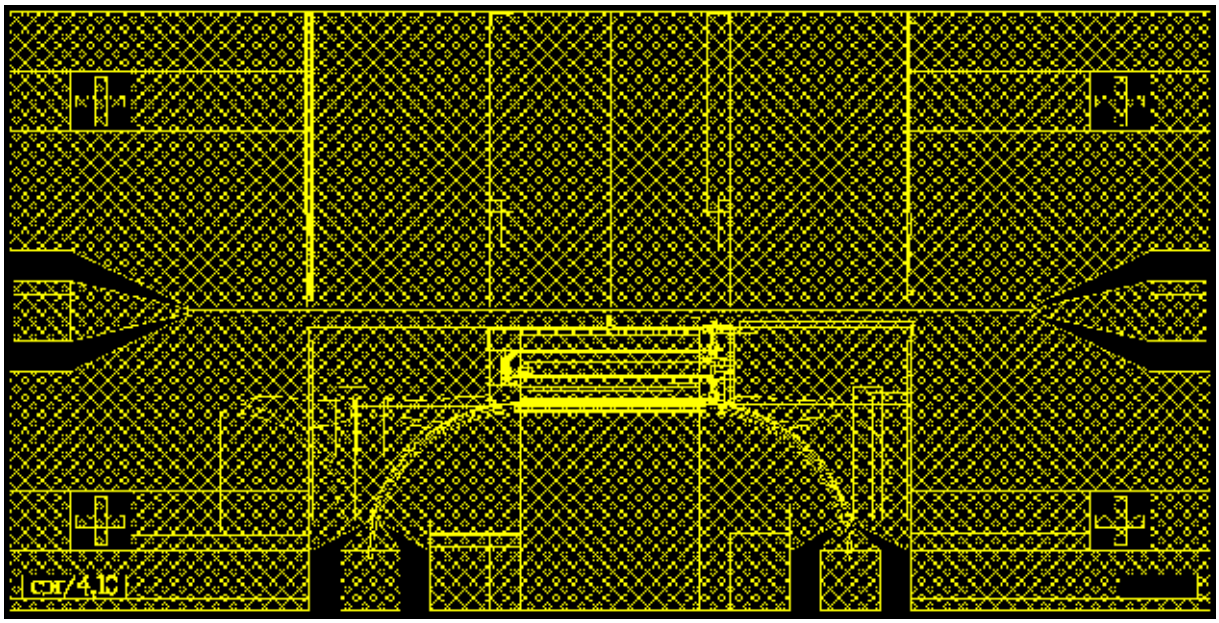


*Fig. C.2:* Quarter wavelength CPR with current control line.

An example of a CPR with a current control line.

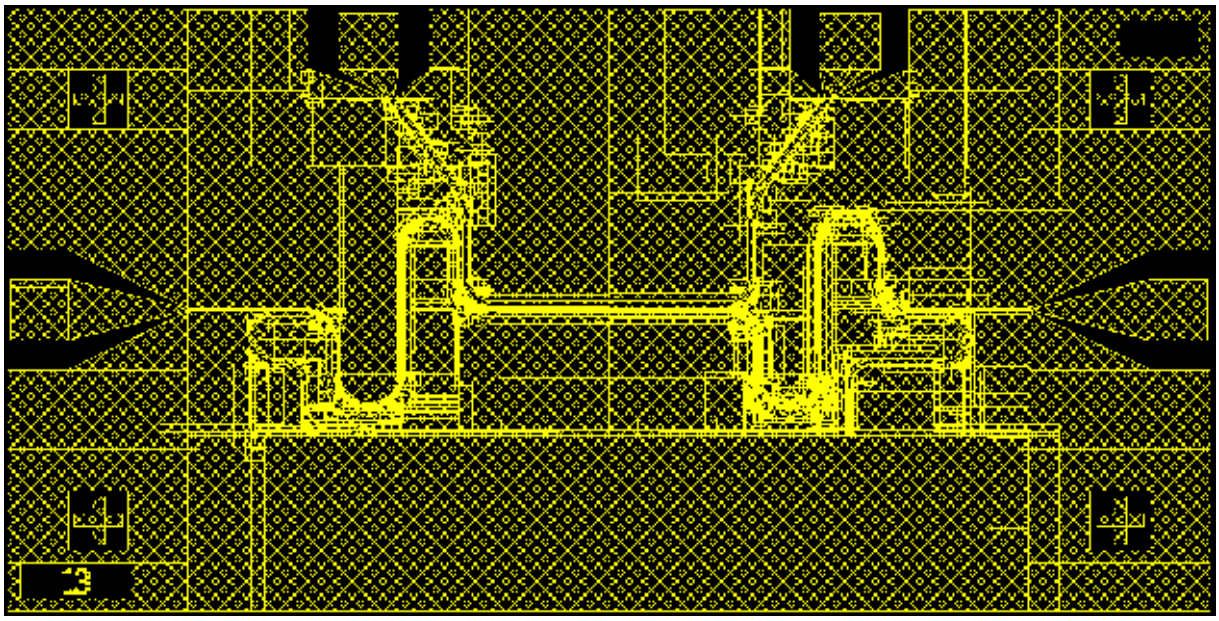


*Fig. C.3:* Half wavelength CPR with a current control line.

Entire mask.

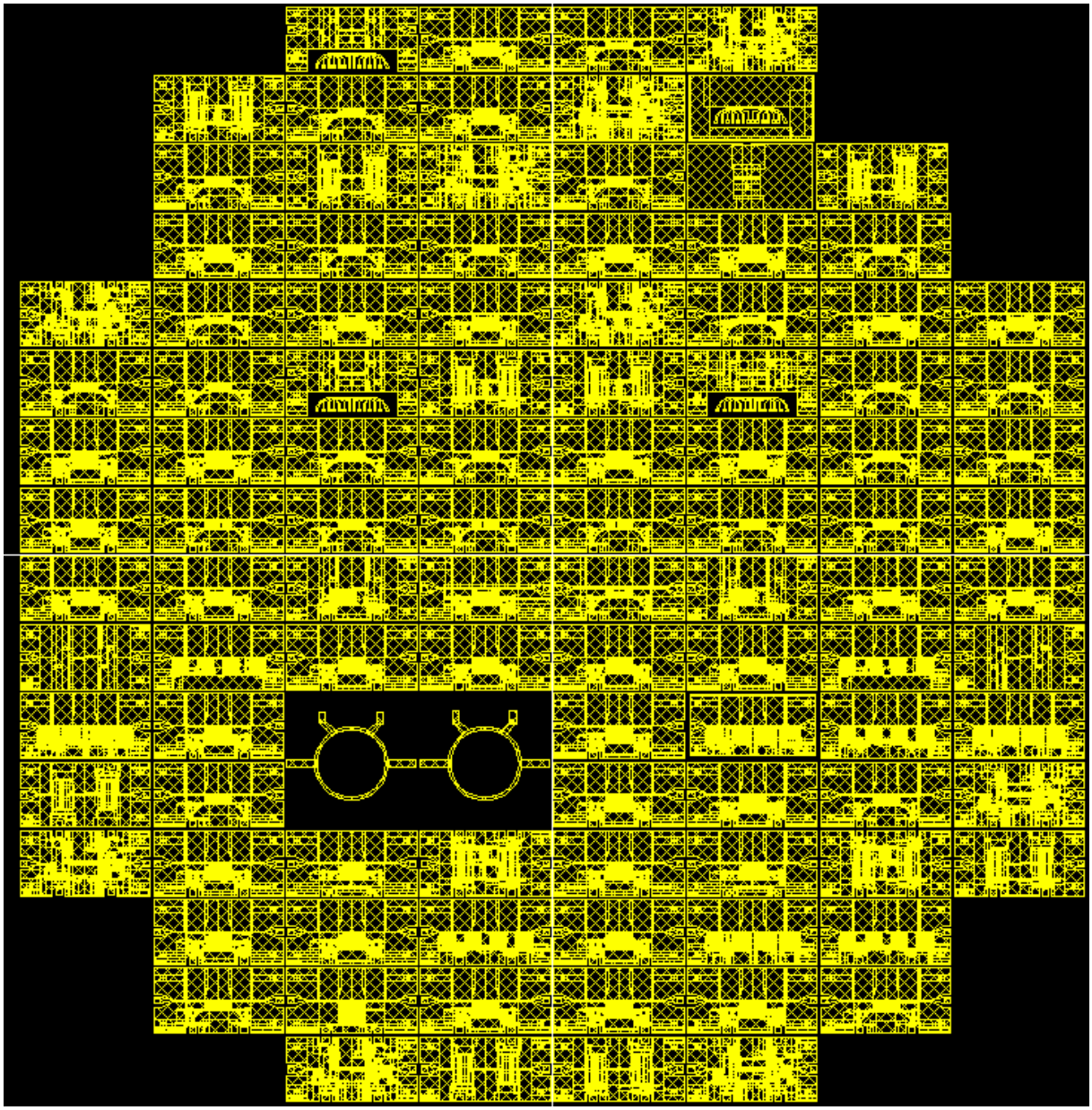

*Fig. C.4:* An image of the complete mask designed in KIC.

# D. RUO CALIBRATION DATA

| Temperature K | Resistance Ω |
|---|---|
| 3.220 | 2864.660 |
| 3.152 | 2879.200 |
| 3.120 | 2885.780 |
| 3.002 | 2910.620 |
| 2.950 | 2922.410 |
| 2.898 | 2934.220 |
| 2.849 | 2945.960 |
| 2.825 | 2951.970 |
| 2.799 | 2958.170 |
| 2.774 | 2964.410 |
| 2.749 | 2970.780 |
| 2.724 | 2977.020 |
| 2.699 | 2983.660 |
| 2.650 | 2997.290 |
| 2.625 | 3004.210 |
| 2.599 | 3011.350 |
| 2.574 | 3018.450 |
| 2.527 | 3032.620 |
| 2.503 | 3039.810 |
| 2.458 | 3053.940 |
| 2.437 | 3060.560 |

| | |
|---|---|
| 2.417 | 3067.200 |
| 2.398 | 3073.380 |
| 2.380 | 3079.660 |
| 2.362 | 3085.820 |
| 2.345 | 3091.800 |
| 2.328 | 3097.480 |
| 2.312 | 3103.020 |
| 2.297 | 3108.390 |
| 2.282 | 3113.420 |
| 2.270 | 3118.060 |
| 2.259 | 3122.460 |
| 2.247 | 3126.880 |
| 2.236 | 3131.160 |
| 2.225 | 3135.340 |
| 2.214 | 3139.380 |
| 2.204 | 3143.320 |
| 2.197 | 3146.440 |
| 2.191 | 3148.480 |
| 2.186 | 3150.560 |
| 2.180 | 3152.910 |
| 2.172 | 3155.720 |
| 2.163 | 3159.110 |
| 2.150 | 3163.810 |
| 2.136 | 3169.680 |
| 2.122 | 3175.960 |
| 2.106 | 3182.840 |
| 2.089 | 3190.140 |
| 2.071 | 3197.670 |

| | |
|---|---|
| 2.053 | 3205.110 |
| 2.035 | 3213.010 |
| 2.018 | 3221.030 |
| 2.000 | 3229.190 |
| 1.983 | 3237.550 |
| 1.966 | 3245.900 |
| 1.948 | 3254.140 |
| 1.931 | 3262.850 |
| 1.913 | 3271.640 |
| 1.894 | 3280.450 |
| 1.873 | 3289.520 |
| 1.857 | 3298.570 |
| 1.840 | 3307.710 |
| 1.823 | 3316.590 |
| 1.807 | 3325.840 |
| 1.790 | 3335.080 |
| 1.757 | 3353.710 |
| 1.741 | 3363.010 |
| 1.726 | 3372.420 |
| 1.711 | 3381.450 |
| 1.696 | 3390.830 |
| 1.681 | 3400.180 |
| 1.667 | 3409.520 |
| 1.652 | 3418.820 |
| 1.637 | 3428.050 |
| 1.623 | 3437.290 |
| 1.610 | 3446.190 |
| 1.597 | 3455.350 |

| | |
|---|---|
| 1.584 | 3464.380 |
| 1.572 | 3473.470 |
| 1.559 | 3482.510 |
| 1.534 | 3500.250 |
| 1.522 | 3509.180 |
| 1.510 | 3518.000 |
| 1.498 | 3526.760 |
| 1.488 | 3535.400 |
| 1.477 | 3543.960 |
| 1.467 | 3552.520 |
| 1.456 | 3560.710 |
| 1.446 | 3569.060 |
| 1.436 | 3577.310 |
| 1.427 | 3585.440 |
| 1.417 | 3593.480 |
| 1.408 | 3601.370 |
| 1.399 | 3609.230 |
| 1.390 | 3616.630 |
| 1.381 | 3624.200 |
| 1.373 | 3631.650 |
| 1.366 | 3638.970 |
| 1.358 | 3646.180 |
| 1.351 | 3653.240 |
| 1.344 | 3660.140 |
| 1.337 | 3666.750 |
| 1.330 | 3673.400 |
| 1.316 | 3686.310 |
| 1.310 | 3692.610 |

| | |
|---|---|
| 1.304 | 3698.700 |
| 1.297 | 3704.500 |
| 1.291 | 3710.290 |
| 1.286 | 3716.030 |
| 1.280 | 3721.570 |
| 1.275 | 3727.000 |
| 1.266 | 3737.360 |
| 1.261 | 3742.220 |
| 1.256 | 3747.120 |
| 1.252 | 3751.870 |
| 1.248 | 3756.460 |
| 1.244 | 3760.980 |
| 1.240 | 3765.310 |
| 1.236 | 3769.510 |
| 1.233 | 3773.480 |
| 1.229 | 3777.450 |
| 1.226 | 3781.290 |
| 1.222 | 3785.000 |
| 1.219 | 3788.630 |
| 1.216 | 3792.090 |
| 1.213 | 3795.440 |
| 1.210 | 3798.570 |
| 1.207 | 3801.710 |
| 1.205 | 3804.770 |
| 1.202 | 3807.640 |
| 1.200 | 3810.470 |
| 1.198 | 3813.150 |
| 1.195 | 3815.640 |

| | |
|---|---|
| 1.193 | 3818.070 |
| 1.191 | 3820.430 |
| 1.190 | 3822.660 |
| 1.188 | 3824.770 |
| 1.186 | 3826.810 |
| 1.184 | 3828.800 |
| 1.183 | 3830.620 |
| 1.181 | 3832.510 |
| 1.180 | 3834.280 |
| 1.178 | 3835.950 |
| 1.177 | 3837.490 |
| 1.176 | 3838.990 |
| 1.175 | 3840.410 |
| 1.174 | 3841.660 |
| 1.173 | 3842.850 |
| 1.172 | 3843.950 |
| 1.171 | 3844.970 |
| 1.170 | 3846.710 |
| 1.169 | 3847.440 |
| 1.168 | 3848.090 |
| 1.167 | 3850.210 |
| 1.166 | 3850.580 |
| 1.165 | 3852.500 |
| 1.164 | 3854.570 |
| 1.163 | 3854.760 |
| 1.162 | 3857.990 |
| 1.161 | 3858.210 |
| 1.160 | 3860.890 |

| | |
|---|---|
| 1.159 | 3861.120 |
| 1.158 | 3863.980 |
| 1.157 | 3864.170 |
| 1.156 | 3866.820 |
| 1.155 | 3867.010 |
| 1.154 | 3868.620 |
| 1.153 | 3870.690 |
| 1.152 | 3871.720 |
| 1.151 | 3873.660 |
| 1.150 | 3874.420 |
| 1.149 | 3876.350 |
| 1.148 | 3877.510 |
| 1.147 | 3879.830 |
| 1.146 | 3880.330 |
| 1.145 | 3882.660 |
| 1.144 | 3883.160 |
| 1.143 | 3885.600 |
| 1.142 | 3886.170 |
| 1.141 | 3888.470 |
| 1.140 | 3889.160 |
| 1.139 | 3891.120 |
| 1.138 | 3893.090 |
| 1.137 | 3893.170 |
| 1.136 | 3896.030 |
| 1.135 | 3896.100 |
| 1.134 | 3898.930 |
| 1.133 | 3899.010 |
| 1.132 | 3901.350 |

| | |
|---|---|
| 1.131 | 3903.390 |
| 1.130 | 3903.480 |
| 1.129 | 3905.880 |
| 1.128 | 3907.670 |
| 1.127 | 3907.760 |
| 1.126 | 3910.320 |
| 1.125 | 3911.940 |
| 1.124 | 3912.050 |
| 1.1123 | 3929.800 |
| 1.1123 | 3929.860 |
| 1.1121 | 3930.140 |
| 1.1120 | 3930.230 |
| 1.1119 | 3930.330 |
| 1.1118 | 3930.410 |
| 1.1117 | 3930.610 |
| 1.1116 | 3930.670 |
| 1.1115 | 3930.920 |
| 1.1114 | 3930.940 |
| 1.1113 | 3931.120 |
| 1.1112 | 3931.370 |
| 1.1111 | 3931.380 |
| 1.1110 | 3931.510 |
| 1.1109 | 3931.780 |
| 1.1108 | 3931.820 |
| 1.1107 | 3931.930 |

*Tab. D.1:* Calibrated RuO sensor, temperature versus resistance.

# E. PERMITTIVITY OF LIQUID HELIUM

| Temperature K | $\epsilon_{helium}$ |
|---|---|
| 4.2 | 1.0493 |
| 4.0 | 1.05052 |
| 3.8 | 1.0517 |
| 3.6 | 1.0527 |
| 3.4 | 1.0537 |
| 3.2 | 1.0546 |
| 3.0 | 1.05552 |
| 2.8 | 1.0562 |
| 2.6 | 1.0569 |
| 2.4 | 1.0573 |
| 2.2 | 1.05748 |
| 2.0 | 1.05713 |
| 1.8 | 1.057 |
| 1.6 | 1.05687 |

*Tab. E.1:* Permittivity of liquid helium as a function of temperature.

# F. MATLAB CODE FOR EXTRACTING RESONATOR PARAMETERS

## *F.1 Fitting Procedure*

Simplifying all the multiple constants from the function shown in equation 7.15:

$$f(T) = A\left[1 - B\lambda(T) - \frac{C\lambda(T)}{sinh(\frac{D}{\lambda(T)})}\right] \tag{F.1}$$

Where A, B, C and D are a combinations of constants that are real and positive. Find where $df(T)/dT- > 0$ to find where any turning points exist in temperature. Now differentiating with respect to T is difficult, but $\lambda(T)$ varies between $\lambda_0$ and $\infty$. So differentiate the function with respect to $\lambda$ and see if a turning point lies within the range $\lambda_0 \rightarrow \infty$. Therefore redefine the function:

$$f(\lambda) = A\left[1 - B\lambda - \frac{C\lambda}{sinh(\frac{D}{\lambda})}\right] \tag{F.2}$$

Differentiate this and set it to zero to find any turning points. Discard the A as this is just a scaling constant.

$$\frac{df}{d\lambda} = 0 = -B - \frac{C}{sinh(\frac{D}{\lambda})} - C\lambda\left(\frac{d}{d\lambda}\right) \cdot \left(\frac{1}{sinh(\frac{D}{\lambda})}\right) \tag{F.3}$$

The term containing C is split in two parts using the product rule. Then using $u = C \cdot \lambda v = 1/sinh(D/\lambda)$ and using the identity $d/dx(1/sinh(x)) = -1/(sinh(x) \cdot tanh(x))$ with the chain rule:

$$\frac{df}{d\lambda} = 0 = -B - \frac{C}{sinh(\frac{D}{\lambda})} - C\frac{dx}{d\lambda} \cdot \frac{d}{dx}\frac{1}{sinh(x)} \tag{F.4}$$

Where $x = D/\lambda$. Perform the differentiation and then resubstitute back in and one gets:

$$0 = -B - \frac{C}{sinh(\frac{D}{\lambda})} - C\lambda\left(\frac{-2D}{\lambda^2}\right)\left(\frac{-1}{sinh(\frac{D}{\lambda})tanh(\frac{D}{\lambda})}\right) \tag{F.5}$$

Tidying this equation:

$$0 = Bsinh\left(\frac{D}{\lambda}\right)tanh\left(\frac{D}{\lambda}\right) + Ctanh\left(\frac{D}{\lambda}\right) + 2C\left(\frac{D}{\lambda}\right) \tag{F.6}$$

## *F.2 Matlab Code*

function out = JoFunc(T,lambda0,epseff)

Tc = 9.20;

A = $4.93674 * 10^{-06}$;

B = $5.06407 * 10^{-06}$;

C = $1.00008 * 10^{-05}$;

D = $1.01281 * 10^{-05}$;

t = $2.00 * 10^{-07}$;

l = $1.10 * 10^{-02}$;

c = $2.99863 * 10^{+08}$;

K = $2.15669 * 10^{+00}$;

mu0 = $1.25663706 * 10^{-06}$;

eps0 = $8.854187817 * 10^{-12}$;

part1 = (1/(2.*l.*sqrt(mu0.*eps0.*epseff)));

part2 = 1.7*(C/(2*A*D*K));

part3 = $(0.4./(\text{sqrt}(((\text{B/A})^2 - 1) * (1 - (B/D)^2)))) * (C/(2 * A * D * K))$;

$out = part1.*(1-part2.*lambdaL(T, Tc, lambda0)./sinh(t./(2.*lambdaL(T, Tc, lambda0)))$

$- part3. * lambdaL(T, Tc, lambda0))$;

$function\ out = lambdaL(T, Tc, lambda0)$

$out = lambda0./((1 - (T/Tc).^4).^{0.5});$

$function\ out = residuals(in, data)$

$fit = JoFunc(data(:,1), in(1), in(2));$
$out = sqrt(sum((fit - data(:,2)).^2));$

$function\ out = PlotData(trange)$
$Tc = 9.20$
$SiData = load('Silicondata.csv');$
$lambda0 = 234 * 10^(-10);$
$eeff = 10;$
$if exist('trange','var')$
$which = find(and(SiData(:,1) > trange(1), SiData(:,1) < trange(2)))$
$SiData = SiData(which,:);$
$end$
$getopt = optimset('fminsearch');$
$getopt = optimset(getopt,'Display','iter','MaxIter',10000,'MaxFunEvals',10000,$
$'TolX',1E-6);$
$fit = fminsearch(@(in)residuals(in, SiData), [lambda0; eeff], getopt);$
$holdoff;$
$plot(SiData(:,1), SiData(:,2),'-r');$
$holdon;$
$plot(SiData(:,1), JoFunc(SiData(:,1), fit(1), fit(2)));$
$out = fit;$

$disp([\prime Lambda0 =\prime\ num2str(fit(1))\prime andeeff =\prime\ num2str(fit(2))]);$

This is courtesy of Richard Lycett.

# G. PAPERS

## *G.1 Contribution.*

My contribution to this project was to design, simulate, fabricate, measure and analyze high $Q$ superconducting Niobium on Sapphire and oxidized Silicon Substrate CPRs.

### *G.1.1 Circuit QED with a flux qubit strongly coupled to a coplanar transmission line resonator.*

I provided pictures, contributed to the calculation of the coupling strength by providing values for the inductance/capacitance of the CPR, measurements of CPR $Q$ factor, and acted as an editor for the publishing of the paper.

### *G.1.2 Numerical Simulations of a Flux Qubit Coupled to a High Quality Resonator.*

I designed, fabricated and measured CPRs with various coupling parameters and device materials.

### *G.1.3 Properties of high-quality coplanar waveguide resonators for QIP and detector applications.*

I designed, fabricated and measured CPRs with various coupling parameters and device materials. Measurements of the resonant frequency and $Q$ as a function of temperature for various CPRs are undertaken in my cryostats.

### *G.1.4 Properties of Superconducting Planar Resonators at Millikelvin Temperatures.*

I designed, fabricated and measured CPRs with various coupling parameters and device materials.

### G.1.5 *Magnetic Field Tuning of Coplanar Waveguide Resonators.*

I designed, fabricated, measured and analyzed CPRs with various coupling parameters and device materials. I measured the resonant frequency and $Q$ as a function of temperature and magnetic field. I acted as the author and editor of the paper, and provided the majority of the graphs.